12 The Acoustic Field in a Waveguide near an Oscillating Elastic Shell.

12.1 Introduction.

An analysis of the temporal evolution of an acoustic field near a scattering object is important for the investigation of a scattering process. Such analysis reveals the *propagation* of acoustic waves and, thus, allows the determination of more than just wave amplitude as is done in Section 9.5.

This chapter presents the results of analysis of an acoustic field in a waveguide near a gas-filled elastic shell (Zinoviev, 2000). These results are compared with the pictures of the reflection coefficient and the velocity amplitudes, presented in section 11. The waveguide configuration is the same as the configuration shown in Fig. 11, and the parameters of the waveguide are the same as those in section 11.3.

Figures from 14 to 43 show pictures of the acoustic field in the waveguide. The source of the incident field is located to the left from the shell at infinite distance. The scattered field is calculated by formula (68), and the total field is the sum of the scattered and the incident fields. Every figure contains eight different pictures showing the acoustic field structure at a given moment in time. The distance between consecutive pictures equals $1/16^{th}$ of the period of the acoustic wave, so that the whole figure covers half of the acoustic period. Red colour represents zones of compression, while blue colour represents zones of rarefaction. White colour represents zones where the fluid is in the state of equilibrium. Due to linearity of the process pictures for the second half of the period would be similar to those shown with the replacement of blue with red and vice versa.

Parameters of scattering are calculated in the wavenumber (frequency) k range between $k = 0.5$ and $k = 32$. This range may be separated in two subranges. The first subrange is a low frequency region from $k = 0.5$ to $k = 10$, where the acoustic wavelength λ is much greater than the diameter of the shell $2R_1$. The second subrange is a middle frequency region from $k = 10$ to $k = 32$, where λ and $2R_1$ are of the same order. These two frequency ranges are discussed in separate sections, where differences in physical characteristics of the scattering process are revealed. A high frequency range, where $\lambda \ll 2R_1$, is not discussed here but may be a subject for further investigation.

12.2 Acoustic Field Structure in the Low Frequency Range.

The low frequency region may be separated further into one-mode and multi-mode ranges. The critical frequency k_n of the waveguide mode of order n for the given boundary conditions (pressure release upper surface and rigid bottom) is defined by the following formula

$$k_n = n + 0.5 \qquad\qquad (82)$$

Between $k = 0.5$ and $k = 1.5$ only lowest mode of order zero can propagate in the waveguide, while in the range $k > 1.5$ at least two modes can propagate, transmitting the acoustic energy into infinite distance.

12.2.1 Acoustic Field in One-Mode Regime.

Figs. 14 - 19 show the acoustic field in the waveguide at the frequency $k = 0.501$, which is just above the critical frequency $k_0 = 0.5$ of the lowest waveguide mode of order zero. In this case, the acoustic wavelength λ is 4 times larger than the waveguide depth D, and, thus, it is much larger than the size of the shell.

12.2.1.1 Structure of the Incident Acoustic Field.

Formula (13) for the longitudinal wavenumber g_n takes the following form for the given boundary conditions:

$$g_n = \left(k^2 - (n+0.5)^2\right)^{1/2}. \qquad\qquad (83)$$

Simple calculations show that for $n = 0$ and $k = 0.501$ $g_0 \approx 32 * 10^{-2}$, and the longitudinal wavelength $2\pi/g_0 \approx 196$, which is 62.5 times larger than the normalised waveguide depth $D = \pi$. With such a small longitudinal wavenumber, the mode of order 0 propagates mostly in vertical direction, bouncing up and down between the waveguide boundaries.

12.2.1.2 Shell of Zero Thickness.

In this section, the case of zero shell thickness is considered. The curve of the reflection coefficient for this case (Figure 12) reveals that at $k \approx 0.5$ the reflection coefficient nearly equals one, so that nearly all acoustic energy is reflected. The mechanism of almost total reflection is clear from Figs. 14 and 15. In all pictures in Fig. 14 the shell is surrounded by white area, indicating that in the close vicinity of the shell the amplitude of the total field is very small. Indeed, at such low frequency the shell with zero thickness behaves like a soft body, that requires the total pressure to be zero on the shell boundary. Therefore, the acoustic sources on the shell boundary produce an acoustic field, which is equal to the incident field in magnitude but opposite to it in phase at every point of the boundary. Fig. 15 shows that the radiated sound wave is symmetrical in the longitudinal direction (Figs. 15a,b). After being radiated from the shell, the acoustic field is reflected from the boundaries and propagates in both backward and forward directions. In the forward direction, it cancels the incident wave, while in the backward direction the radiated wave is added to the incident acoustic field, giving rise to a standing wave.

Figs. 15a,b show that there is a strong dipole component in the scattered field near the shell. However, from Fig. 12a it is seen that at

$k \approx 0.5$ there is a monopole component in the shell vibrations as well. Apparently, The dipole component is caused by vertical movement of fluid particles in the incident wave, while the monopole component is caused by monopole oscillations of the shell in the incident pressure field. From Figs. 15a,b it is clear that multimodal shell vibrations lead to propagation of a wave of pressure near the surface of the shell. Indeed, the white region in these pictures is shifted significantly during each time interval between them (1/16th of the acoustic period), which means propagation of a wave along the shell boundary.

12.2.1.3 Thin Shell of Non-Zero Thickness.

Figs. 16 and 17 present the results for a shell with small, but non-zero, wall thickness, $d = 0.01 * R_1$. The picture of the total acoustic field, shown in Fig. 16, makes it clear that the shell in this case does not change noticeably the structure of the acoustic field in the waveguide. The reflected field, shown in Fig. 14, has the same structure as in the case of zero shell thickness. Due to the finite shell thickness, however, the amplitude of the shell oscillations is much smaller, so that the incident field can not be cancelled by the reflected field in the area behind the shell. This explains the very small reflection in this situation (Fig. 12d).

Results for a thicker shell with $d = 0.05 * R_1$ is shown in Figs. 18 and 19. The shell in these pictures is located near the upper acoustically soft boundary. It may be observed that the total field structure is changed very little by the shell. The picture of the scattered field (Fig. 19a) shows that the near field has a dipole component, seen also in the velocity distribution on the surface of the shell (Fig. 13e). Absence of the monopole component in this situation can be explained by the incident field structure. Due to the boundary conditions, the incident field has a minimum at the upper surface. Thus, the acoustic pressure amplitude near the surface is too small for the excitation of monopole "breathing" oscillations of the shell.
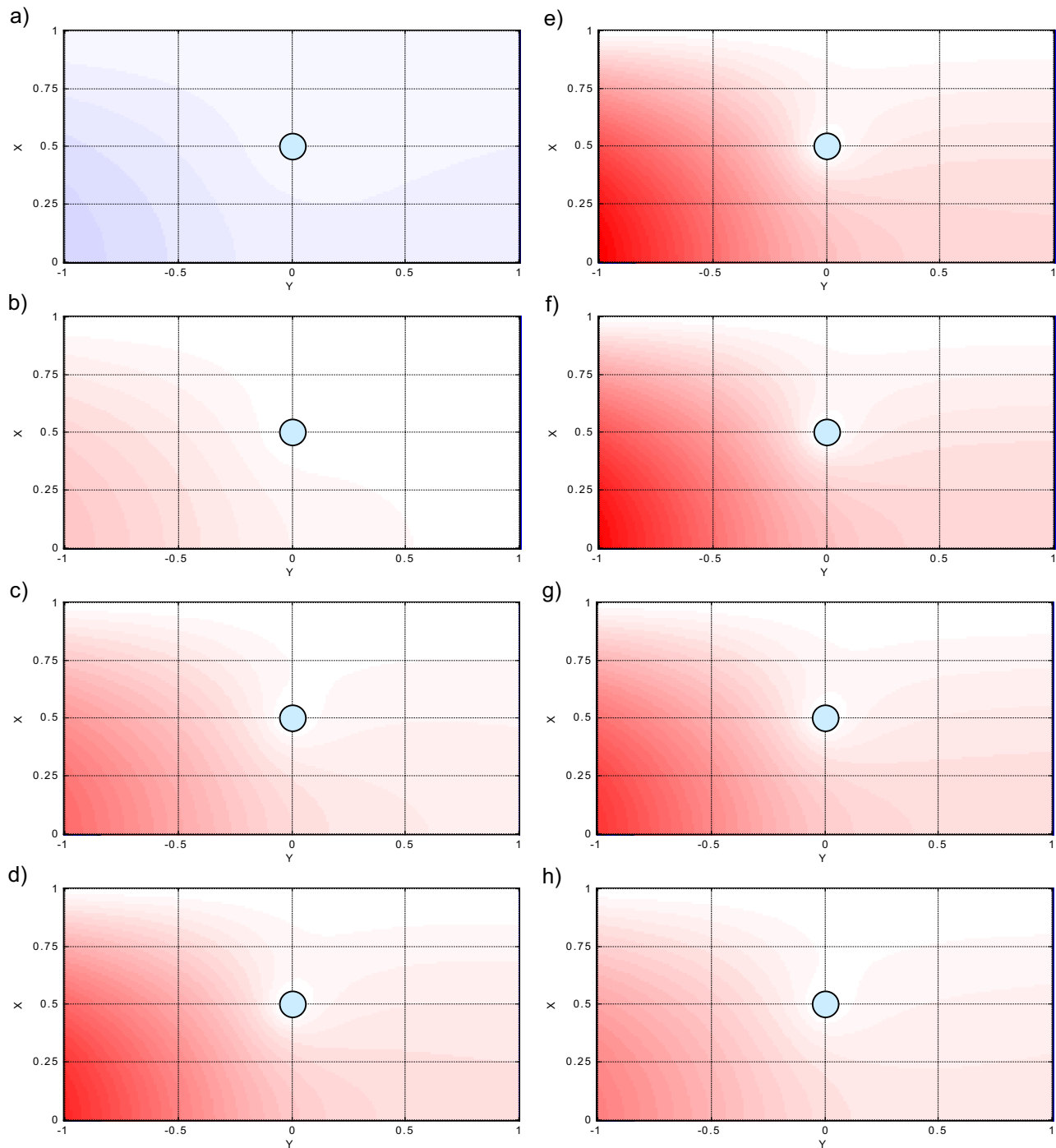
Figure 14. Total acoustic field. The shell is in the centre of the waveguide.
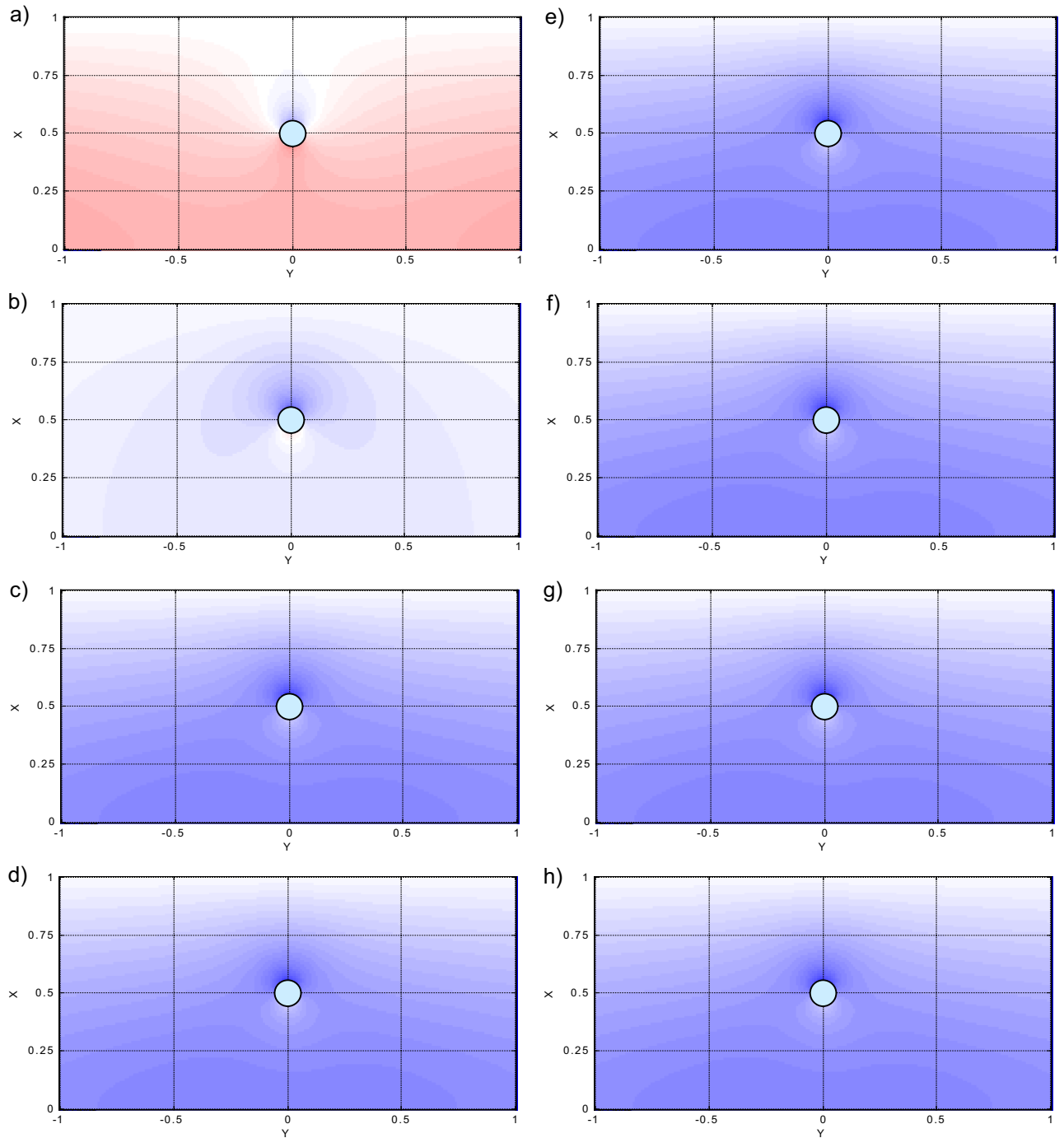*The shell thickness $d = 0$, wavenumber $k = 0.501$.*

Figure 15. Scattered acoustic field. The shell is in the centre of the waveguide . The shell thickness $d = 0$, wavenumber $k = 0.501$
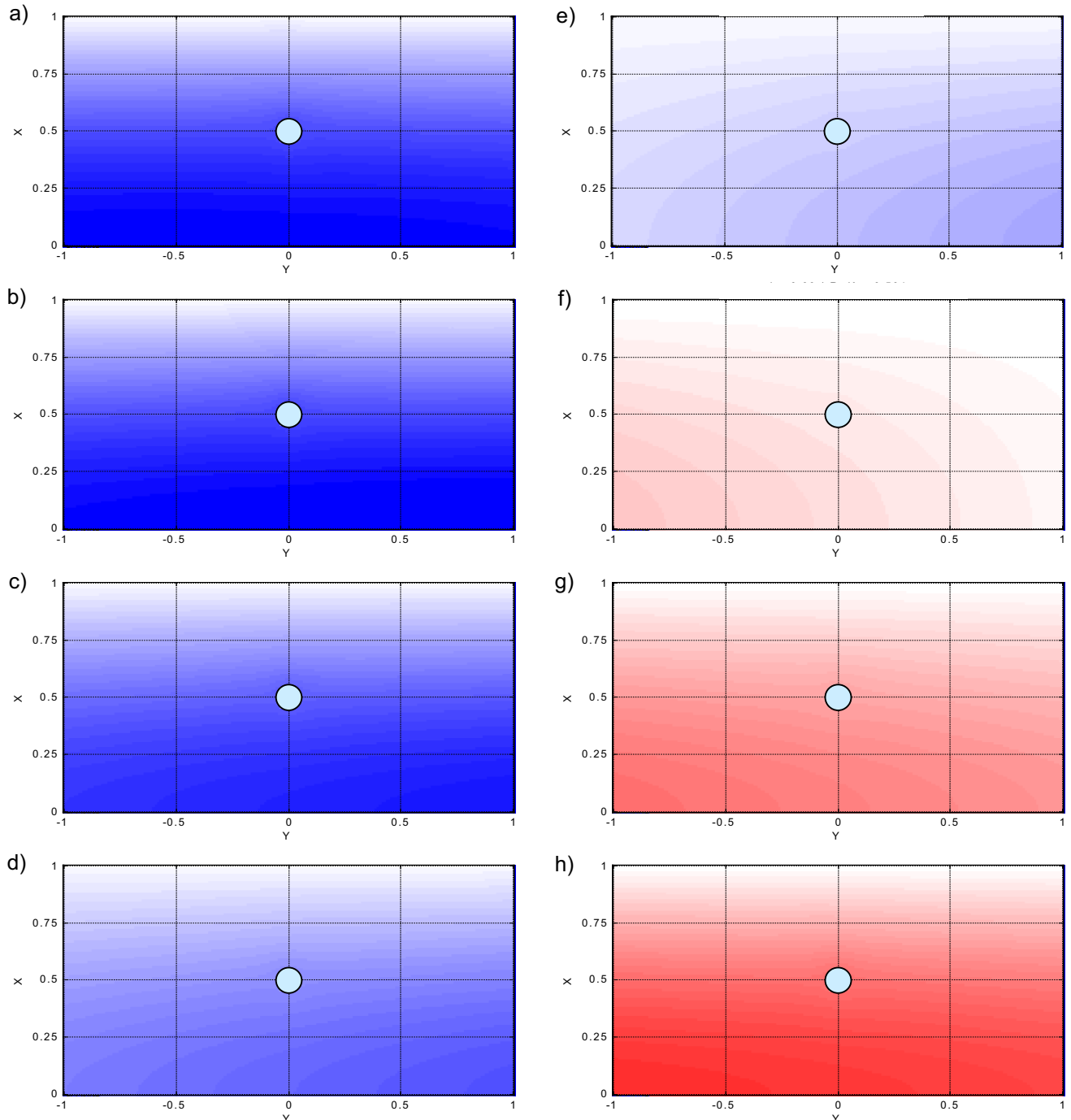
Figure 16. Total acoustic field. The shell is in the centre of the waveguide.
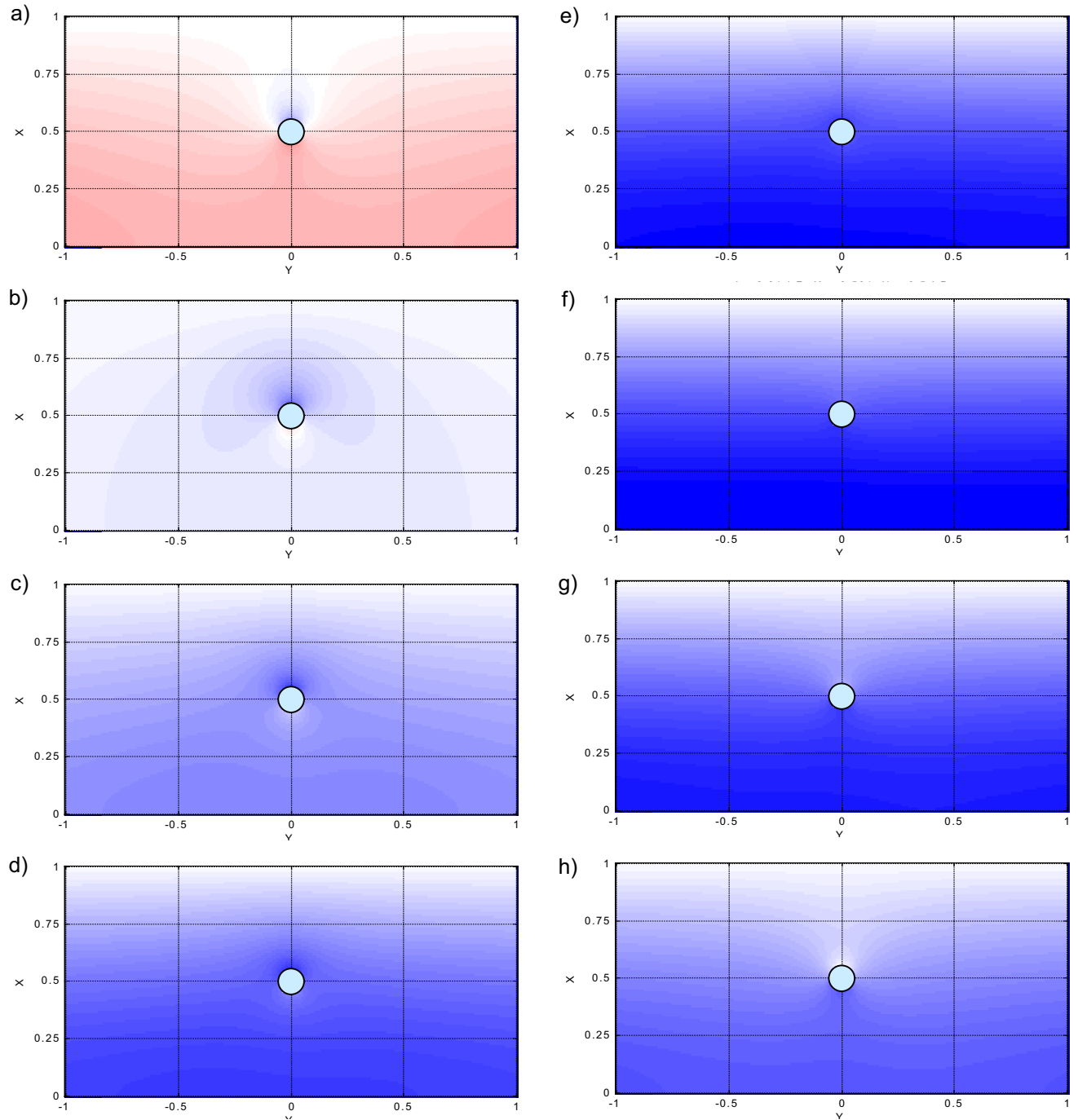*The shell thickness $d = 0.01*R_1$, wavenumber $k = 0.501$.*

Figure 17. Scattered acoustic field. The shell is in the centre of the waveugide.
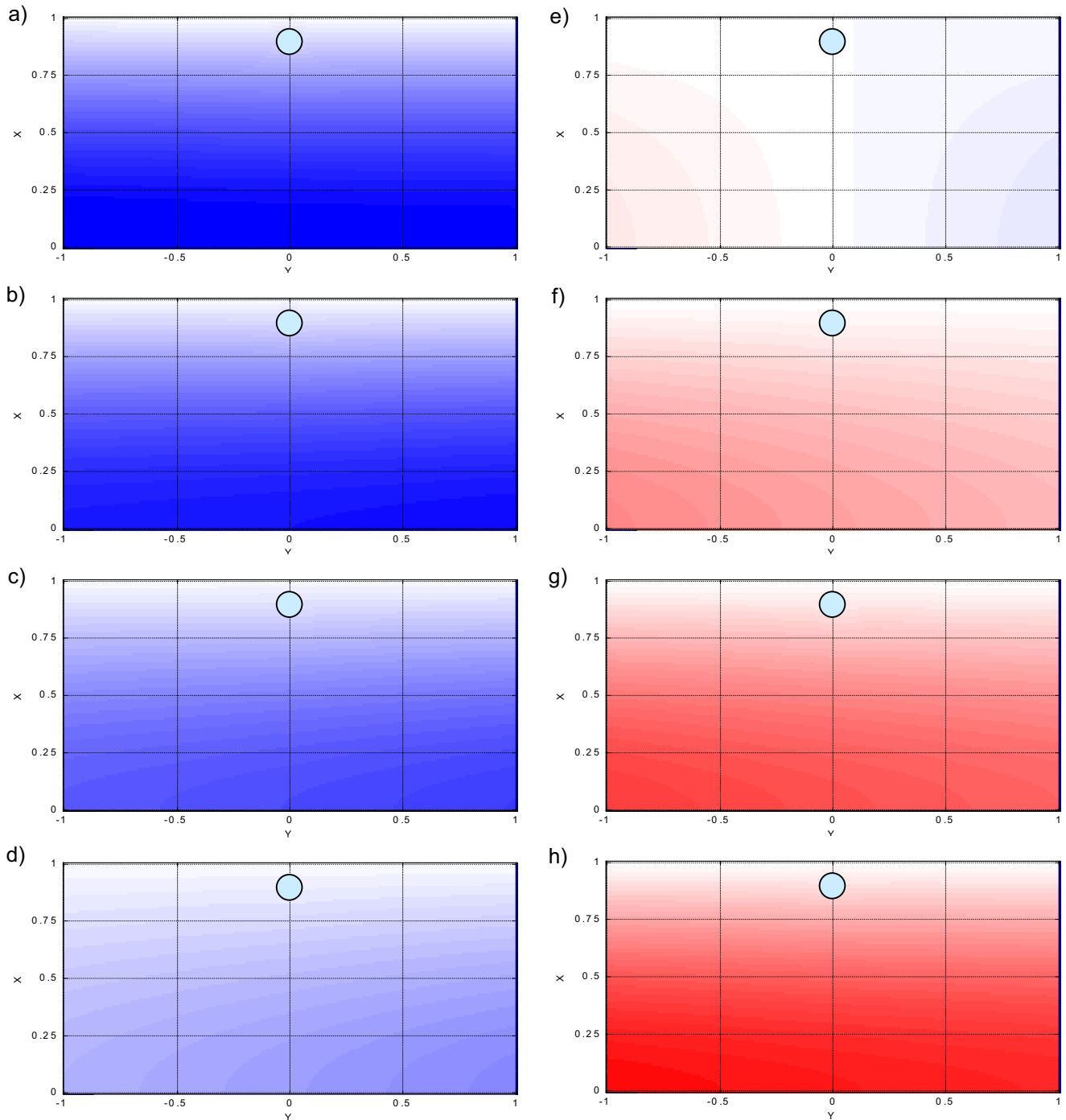*The shell thickness d = 0.01*R$_1$, wavenumber k = 0.501.*

Figure 18. Total acoustic field. The shell is located near the upper boundary.
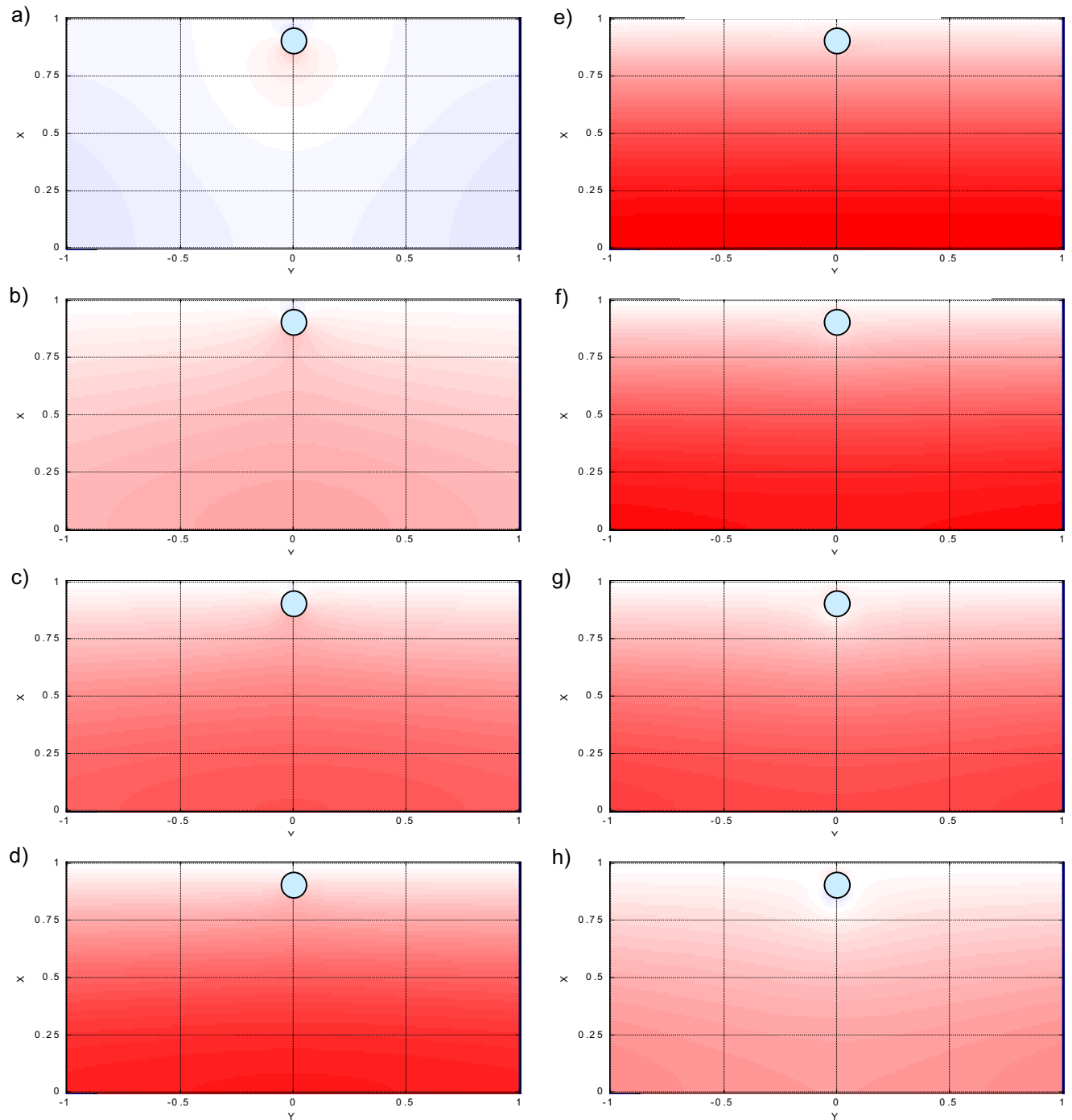*The shell thickness $d = 0.05*R_1$, wavenumber $k = 0.501$.*

Figure 19. Scattered acoustic field. The shell is located near the upper boundary. The shell thickness d = 0.05*R₁, wavenumber k = 0.501.

12.2.2 Acoustic Field in Multi-Mode Regime.

The reflection coefficient curve for a thin shell with thickness $d = 0.01*R_1$ (Fig. 12d) has a distinct feature: a wide maximum in the low frequency range near $k = 5$. This section presents an analysis of the time evolution of the acoustic field, where two frequencies in the area of this maximum are considered. The first frequency is $k = 2.601$, and the second frequency is $k = 5.401$.

12.2.2.1 Acoustic field at the Monopole Resonance of the Shell.

The first of these frequencies, $k = 2.601$, is close to the critical frequency of the waveguide mode of order 2. It can be seen from Fig. 12d, that this frequency corresponds to neither a minimum nor a maximum of the reflected signal. It is shown in the section 11.3 that this frequency coincides with the lowest order monopole resonance of the shell.

Fig. 20 presents the spatial structure of the total acoustic field at the frequency $k = 2.601$. Clear vertical wavefronts of incident waves are seen moving from left to right. However, these wavefronts are distorted by the field scattered from the shell, especially in the vicinity of the shell (Fig. 20f) and in the top half of the waveguide (Fig. 20h).

Fig. 21 confirms the existence of a strong monopole component in the scattered field at this frequency (Fig. 21d). As in the very low frequency case, as described in the section 12.2.1, the higher modes in the shell oscillations cause the propagation of pressure waves along the shell surface (Fig. 21c,d). Yet, the surface waves in this situation propagate from left to right, rather than from the top to the lower part of the shell. This fact is explained by the direction of the wave vector of the incident wave, which is nearly horizontal in this case.

Figs. 21 reveals white belts, indicating fluid in the state of equilibrium, which stay almost at the same place in the waveguide in the area between the shell and the waveguide boundaries. This suggests the existence of standing waves caused by the reflection of sound from the waveguide boundaries.

Figs. 20 and 21 provide a verification that the frequency $k = 2.601$ is close to the monopole resonance of the shell. Comparison of the pictures from both figures, corresponding to the same moments in time, shows that the phase shift between the scattered and the incident waves is approximately equal $\pi/2$. Indeed, while the incident field is at its minimum near the shell (Fig. 20c), the scattered field changes its phase from compression to rarefaction (Fig. 21c). This means that the scattered field near the shell is behind the incident field by a quarter of a period, or $\pi/2$. This correlates with the results obtained by Donskoi *et al.* (1990) for resonance oscillations of an air-filled cavity near a piston. Comparison of Fig. 20g and Fig. 21g leads to the same conclusion.

12.2.2.2 Acoustic Field at the Maximum of the Reflection Coefficient.

The second of the considered frequencies, $k = 5.401$, is close to the maximum of the reflection coefficient in Fig. 12d and lies above the monopole resonance discussed in the previous section. Figs. 22 and 23 represent the pressure field for this frequency.

Fig. 22 for the total field shows, as does Fig. 20 for $k = 2.601$, vertical wavefronts of the incident wave, distorted by higher modes radiated by the shell. The wavelength is smaller due to the higher frequency, which makes structure of the scattered wave in Fig. 23 more complex. The picture of the scattered wave shows that there is still a significant monopole component. Surface pressure waves, caused by interference of different modes in the shell oscillations, propagate from the front to the rear part of the shell. The standing waves between the shell and the waveguide boundaries are shown more clearly than at $k = 2.601$.

Comparison of the phases of the incident and the scattered fields confirms that the frequency $k = 5.401$ is higher than the shell resonance. Fig. 22e shows that the incident field has a minimum near the shell, while the scattered field at the same moment in time has a maximum near the shell (Fig. 23e). This shows that the phase difference between the scattered and the incident fields is close to π, which corresponds to a frequency above resonance according to Donskoi *et al.* (1990).
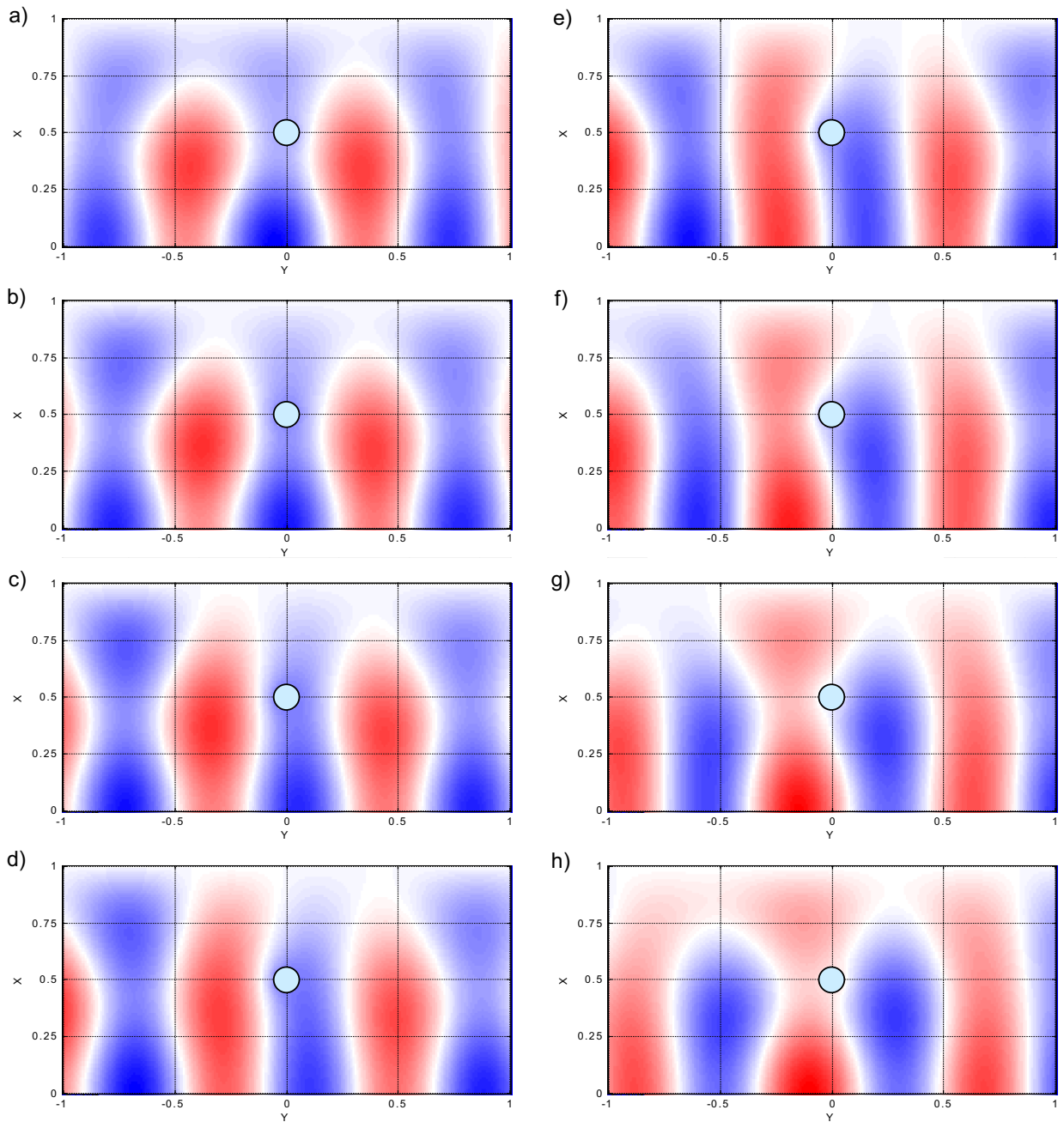
Figure 20. Total acoustic field. The shell is located in the middle of the waveuguide.
The shell thickness $d = 0.01*R_1$, wavenumber $k = 2.601$.

Figure 21. Scattered acoustic field. The shell is located in the middle of the waveuguide. The shell thickness $d = 0.01*R_1$, wavenumber $k = 2.601$.

Figure 22. Total acoustic field. The shell is located in the middle of the waveuguide..
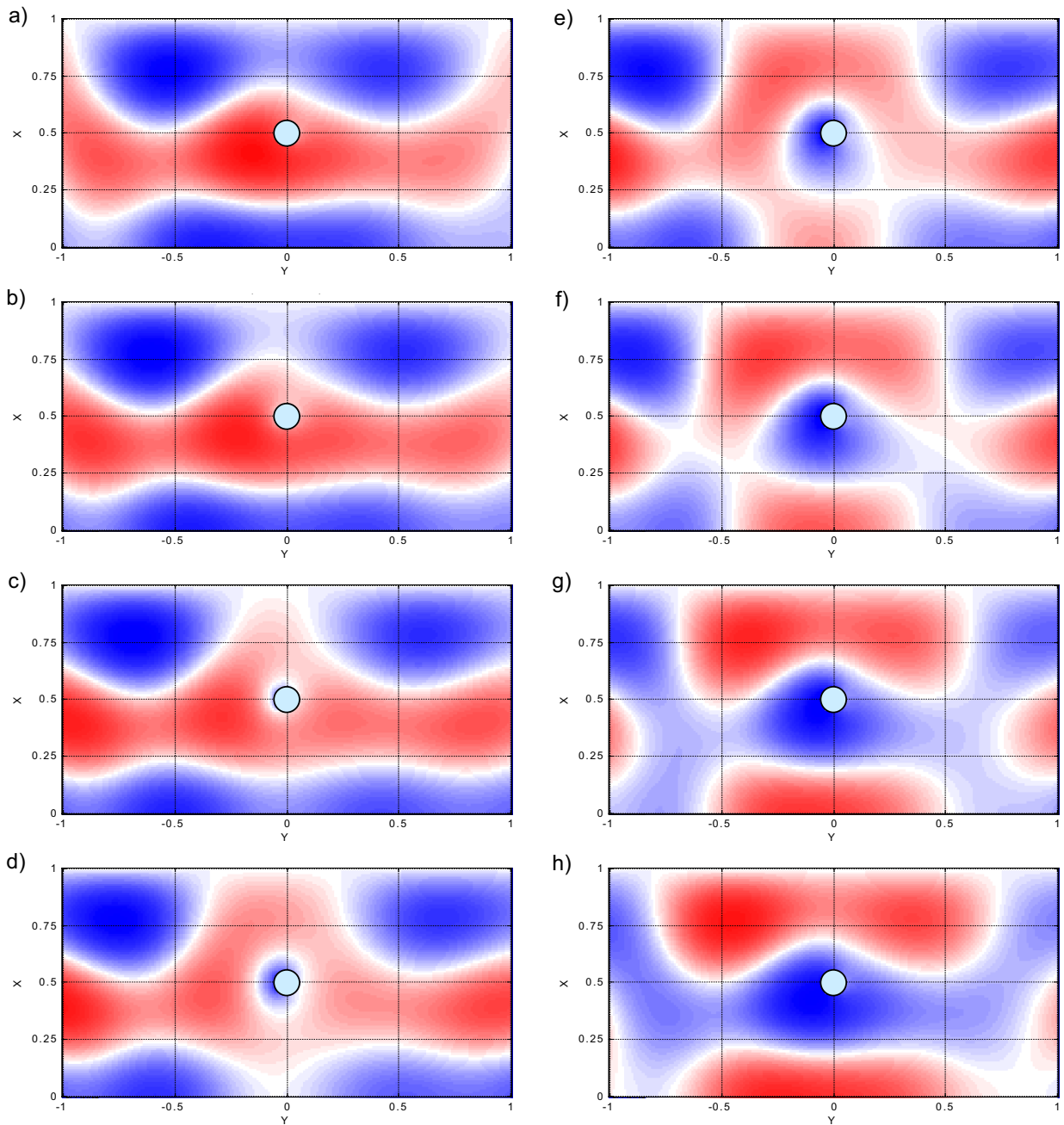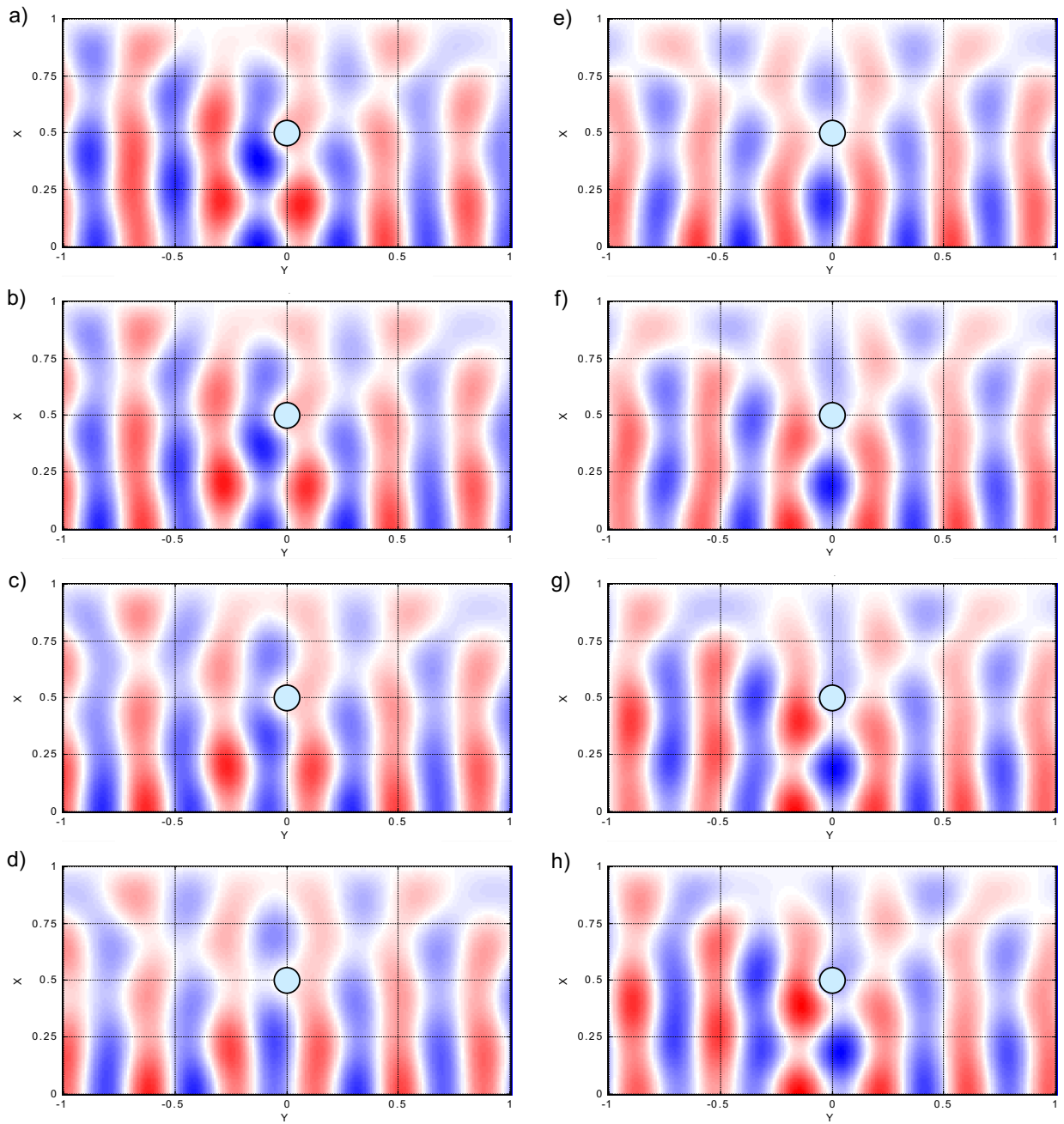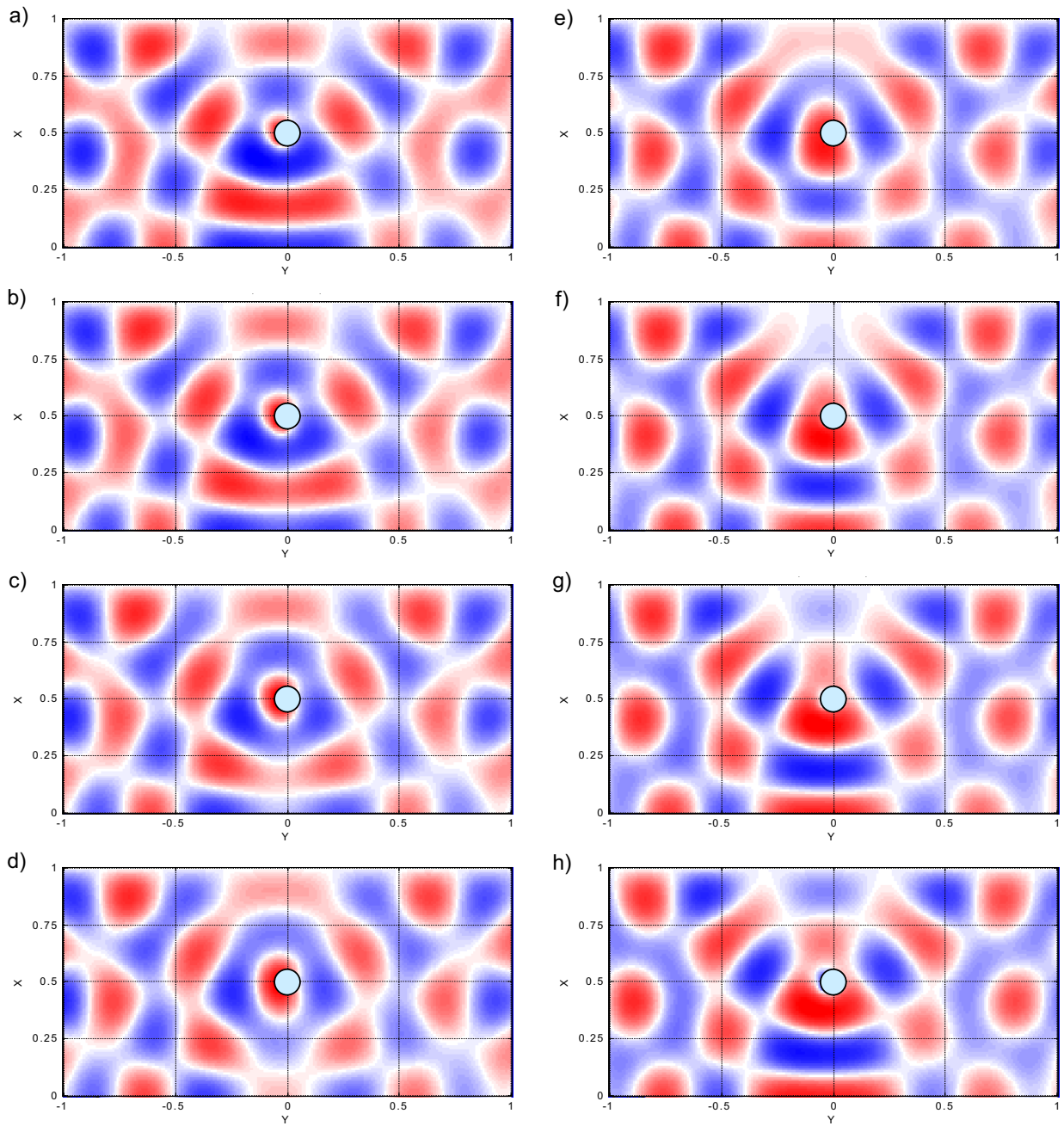*The shell thickness $d = 0.01*R_1$, wavenumber $k = 5.401$.*

Figure 23. Scattered acoustic field. The shell is located in the middle of the waveguide. The shell thickness $d = 0.01*R_1$, wavenumber $k = 5.401$.

12.3 Acoustic Field in the Middle Frequency Range.

This section presents results of calculations of the acoustic field and their analysis in the range where the acoustic wavelength and the diameter of the shell are of the same order. It should be noted that modelling of the scattering in this frequency range is usually very difficult. The analysis carried out in this section is made possible by use of the Multi-Modal Integral Method, which has few restrictions on the wavelength, size of the object, and the waveguide depth.

12.3.1 Comparison of Resonant and Non-Resonant Fields

The picture of the reflection coefficient for the shell with zero thickness (Fig. 12b) showed two sharp minima denoted by letters A and B. It was shown in section 11.3, that these minima are associated with strong monopole and dipole resonances respectively. This section presents an investigation of an acoustic field in the narrow frequency range about the monopole resonance at A. A comparative analysis of the field at the dipole resonance at B and at the same frequency for a thin shell, where the resonance at B is not observed, is carried out as well.

12.3.1.1 Acoustic Field at Non-Resonance Frequency.

The acoustic field in a non-resonant case will be considered first. This case allows consideration of the general features of the acoustic field in the middle frequency range. Figs. 24 - 27 show the structure of the acoustic field at the frequency k = 14.701, which is close to the frequency of the monopole resonance at A, k_A = 15.801, but outside the narrow resonance region.

12.3.1.1.1 Acoustic Field in the Far Field Zone.

Fig. 24 shows the total acoustic field in the waveguide in this case. It is clearly seen that vertical wavefronts of the incident wave prevail in the field structure. However, the higher waveguide modes, radiated by the shell, exist as well. This confirms that a scattering object significantly changes the modal composition of the acoustic field in a waveguide.

A distinct feature in this figure is a shadow in the area behind the shell. This shadow is not observed in the low frequency range, because in that range the shell is much smaller than the acoustic wavelength, and the acoustic wave is diffracted around the shell. In the case under consideration, the ratio of wavelength to the diameter of the shell is close to unity. This value of the ratio is small enough for the shadow to exist, but large enough to make the shadow very indistinct.

The vertical wavefronts are distorted significantly near the top waveguide boundary, which can be explained by the spatial structure of the incident and scattered fields. Indeed, the incident field consists of one lowest order mode only, which has a maximum at the bottom

and a zero at the upper surface. Therefore, the amplitude of the incident field is quite small in the top part of the waveguide. On the other hand, the higher modes in the scattered field have many maxima, which are equal to each other by value. Hence, near the upper boundary of the waveguide, the amplitude of the scattered field becomes comparable to the incident field.

The area near the upper surface to the left from the scattering shell is of special interest. In this region, the incident and the scattered fields propagate in opposite directions. At some points in the waveguide, the amplitude of the scattered field becomes larger than the amplitude of the incident field. This leads to the phase speed, of the total acoustic wave, being directed from right to left, that is opposite to the incident wave. It is suggested that an energy vortex, analogous to the vortices shown in Fig. 10, exists in this area of the waveguide.

Fig. 25 shows the scattered acoustic field structure for the non-resonant frequency $k = 14.701$. It is clear that the acoustic field, radiated by the shell propagates in circular waves. The wavefronts are distinct near the shell, but become less definite as the distance from the shell increases. The cause of this is interference of fields travelling by different acoustic paths from the shell.

Above and below the shell the interference of the wave radiated from the shell and the wave reflected from the boundaries leads to the appearance of a standing wave. The standing wave in this case is more distinct than that in the low frequency range considered above. The waves above and below the shell are shifted in phase by half a period because the boundaries above and below are respectively free and rigid.

12.3.1.1.2 Acoustic Field in the Near Field Zone.

The structure of the acoustic field near the shell is shown in Figs. 26 and 27. The area of the waveguide shown in these pictures corresponds to the area of the rectangle shown in Figs. 24 and 25.

Fig. 26 for the total acoustic field clearly depicts the acoustic waves propagating along the surface of the scattering object. Indeed, the wavefronts of the total acoustic field are perpendicular to the shell surface, which means that the waves propagate along the shell boundary. This picture reveals that the surface waves near a scattering object are excited not only at resonance frequencies. In fact, they turn out to be a universal feature of scattering processes.

Another feature shown in Fig. 26 is a zone of small pressure amplitude near the shell boundary revealed by the white belt. The shell has zero wall thickness, and all elasticity of the shell is associated only with the air in the shell interior. Therefore, in the non-resonance case the shell behaves like a soft body, which requires the pressure on its surface to be close to zero.

Fig. 27 shows the scattered field in the near field zone. The field scattered by the shell is generated by waves of acoustic sources

propagating along the shell boundary. Moving along the shell, the waves generate the circular wavefronts of the scattered field seen also in Fig. 25.

The direction of propagation of these waves coincides with the direction of propagation of incident wave, leading to the conclusion that these sources are fluctuations of pressure excited on the shell surface by the incident wave. In the case under consideration, the phase of the scattered wave is opposite to the phase of the incident wave. This is caused by the boundary conditions on the shell of zero thickness.

It is important to note that at the non-resonance frequency the amplitude of the surface waves remains constant as the waves propagate along the shell boundary. It is shown below, that this is not the case at a resonance frequency.

Figure 24. Total acoustic field in the far field zone. The shell is located in the middle of the waveguide. The shell thickness $d = 0$, wavenumber $k = 14.701$. Rectangle reveals area shown in Fig. 26

Figure 25. Scattered acoustic field in the far field zone. The shell is located in the middle of the waveguide. The shell thickness $d = 0$, wavenumber $k = 14.701$. Rectangle reveals area shown in Fig. 27.
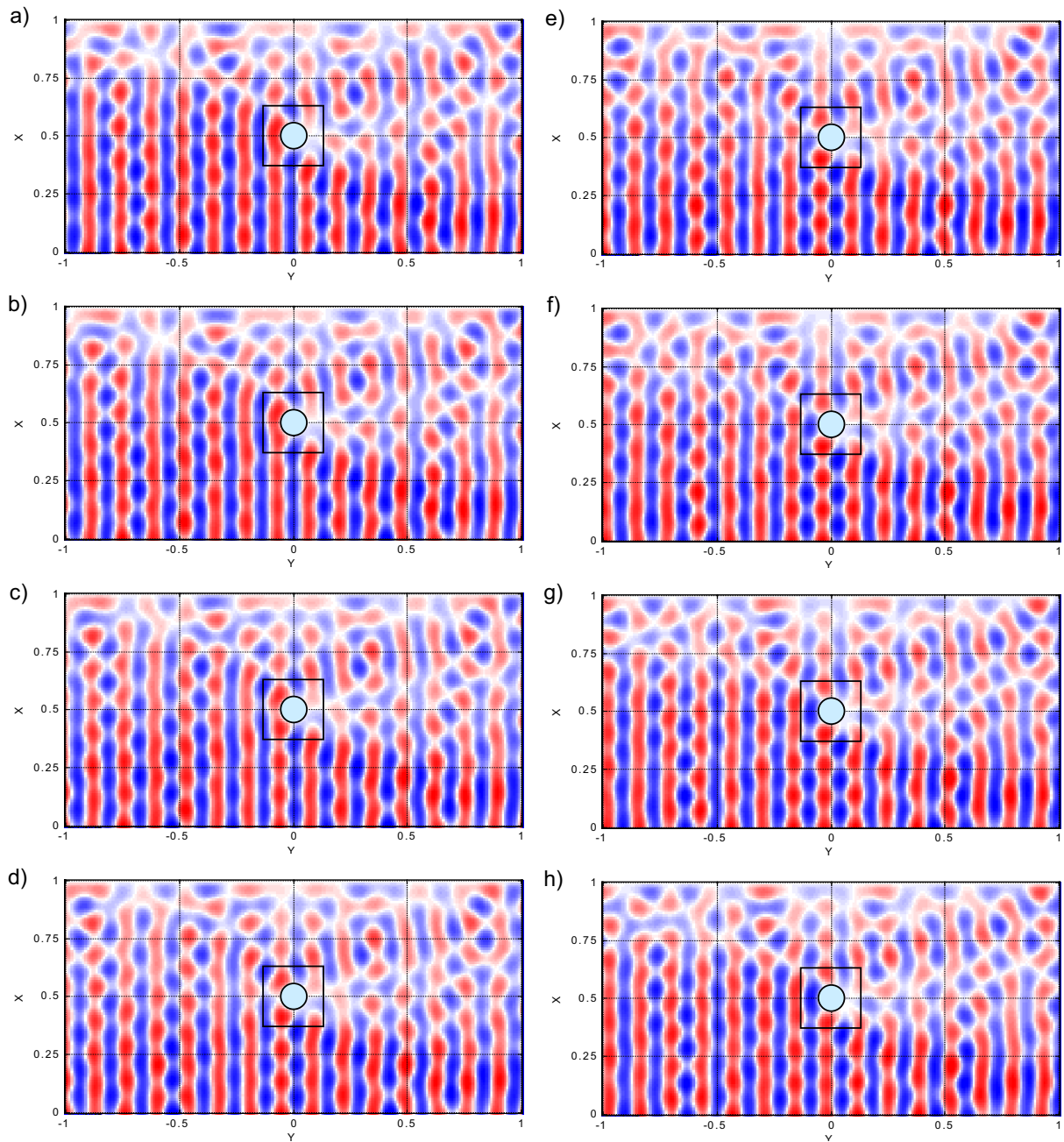
Figure 26. Total acoustic field in the near field zone. The shell is located in the middle of the waveguide. The shell thickness $d = 0$, wavenumber $k = 14.701$.
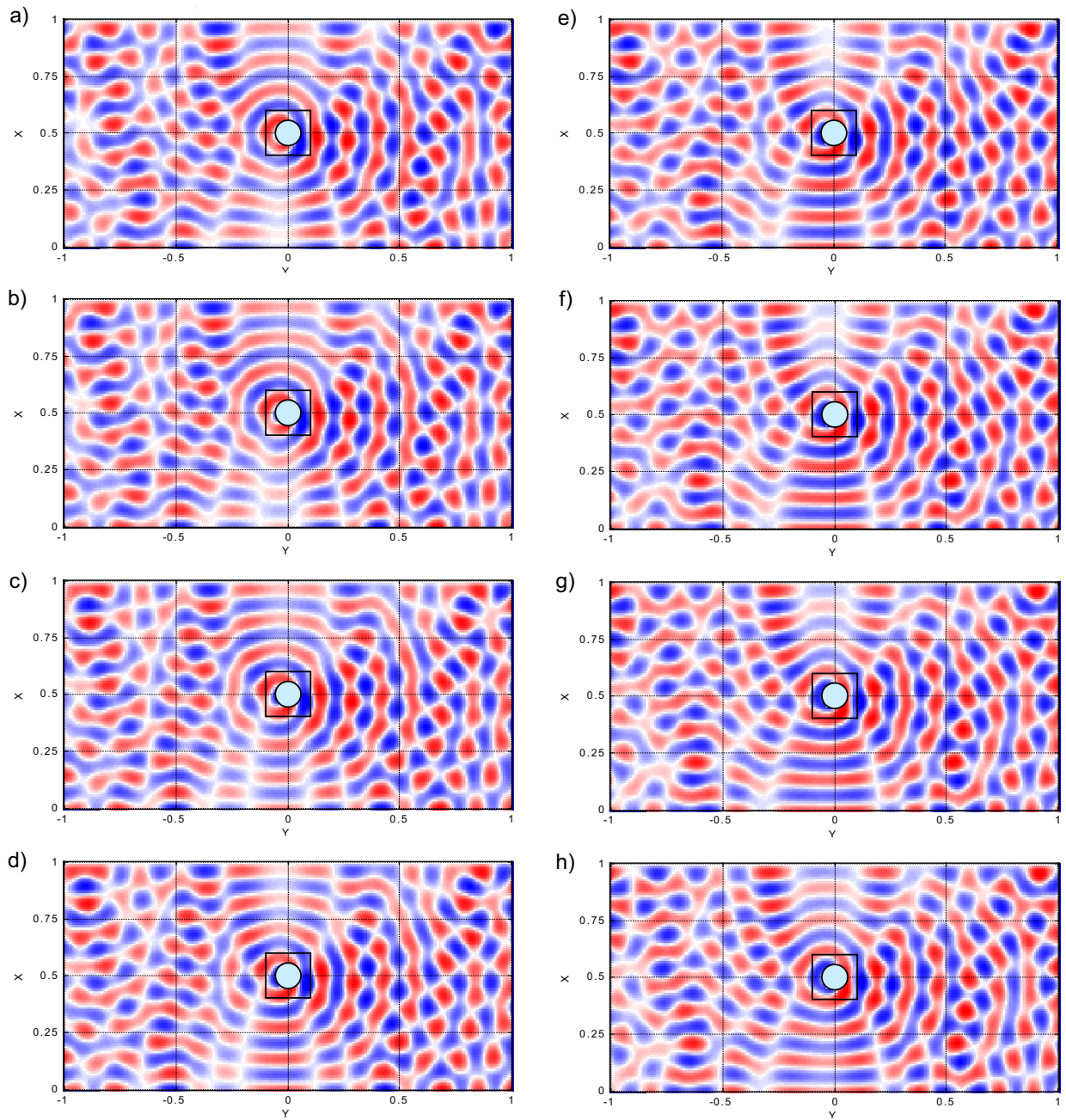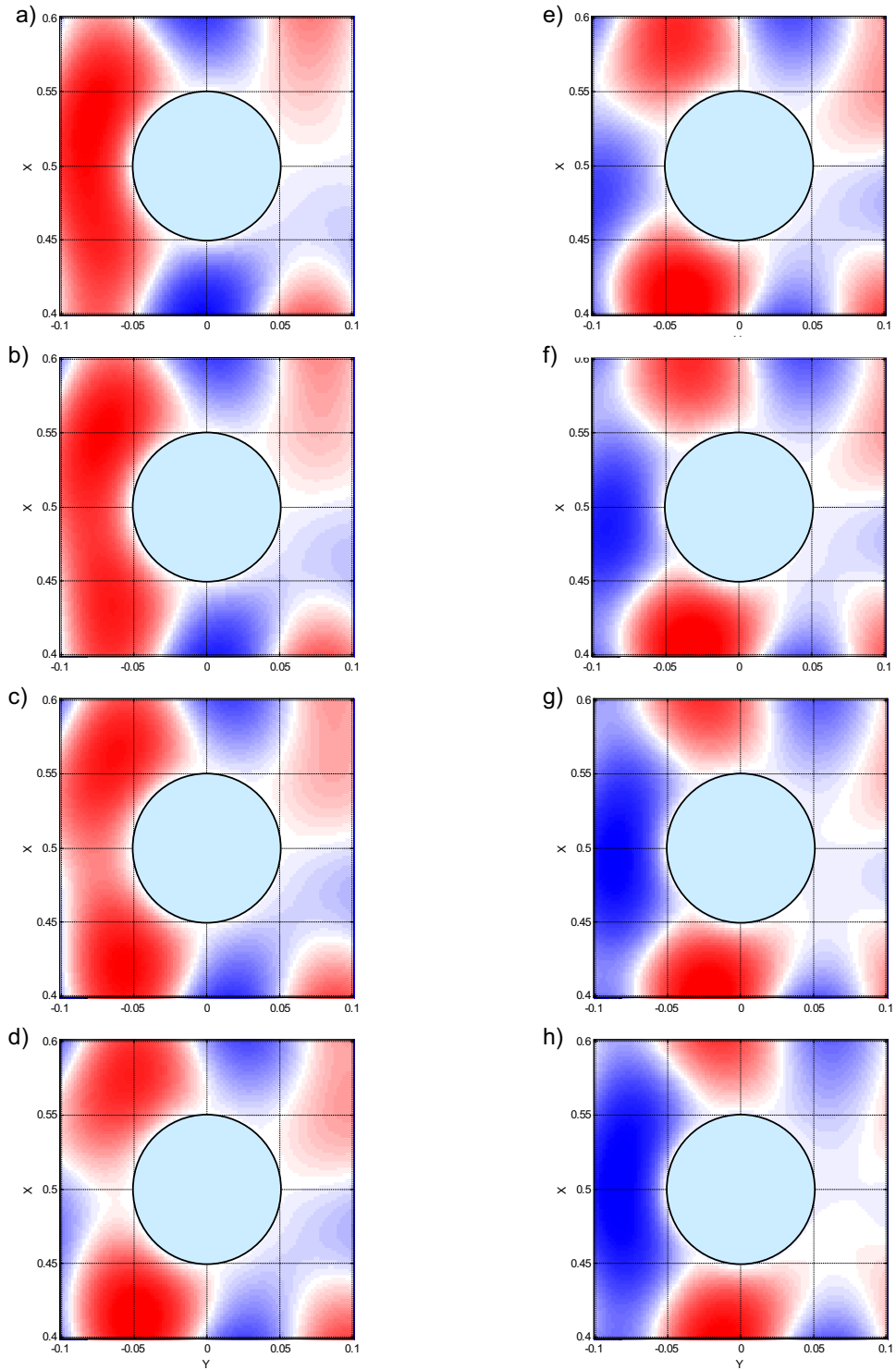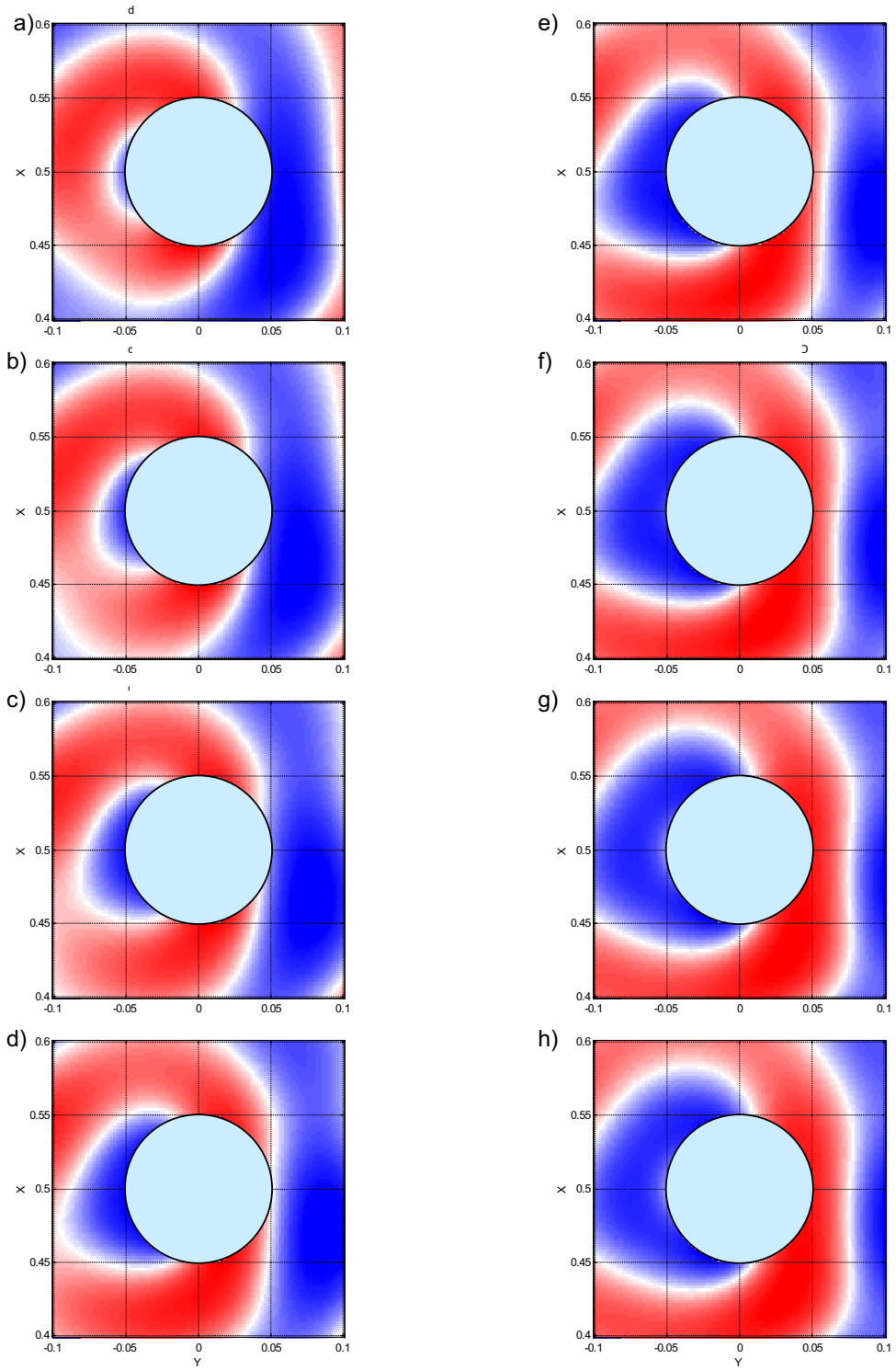
Figure 27. Scattered acoustic field in the near field zone. The shell is located in the middle of the waveguide. The shell thickness d =0, wavenumber k = 14.701.

12.3.1.2 Acoustic Field at the Monopole Resonance.

The second case to be considered is a case of the frequency $k = 15.801$, corresponding to the minimum A in Fig. 12. As was shown in section 11.3, this minimum is associated with a monopole resonance of the shell.

12.3.1.2.1 Acoustic Field in the Far Field Zone.

Fig. 28 shows the total acoustic field in the far field zone. As does Fig. 24 for the non-resonance case, this figure reveals the vertical wavefronts of the incident wave, indistinct shadow behind the shell, and pressure maxima moving in the backward direction in the top part of the waveguide.

However, this figure differs from the figure for the non-resonance case by the amplitude of the higher waveguide modes reflected from the shell. Comparison of Fig. 24 for the non-resonance case and Fig. 28 for the resonance case shows that the pressure maxima, associated with the higher modes, are smaller in the former case, than in the latter. This is in agreement with the sharp decrease of the reflection coefficient at resonance A shown in Fig. 12b.

The ability of the shell to transmit the acoustic energy efficiently at a resonance is clearly seen in Fig. 29. Indeed, the amplitude of the scattered wave radiated forward from the shell is much higher than the amplitude of the wave radiated backwards. This is entirely different from the non-resonance case (Fig. 25), where the shell radiates the energy equally to all directions.

12.3.1.2.2 Acoustic Field in the Near Field Zone.

The total and the scattered acoustic fields in the close vicinity of the shell for the resonance case are shown in Figs. 30 and 31 respectively. Opposite to the non-resonance case (Fig. 26), there is no white belt near the shell in Fig. 30 for the total field. Instead, the phase of the field is the same along the entire shell surface. For example, in Fig. 30a the total field is in the phase of rarefaction near the shell boundary in spite of the wave of compression coming from the left. In Fig. 30b the total pressure is close to zero, and in Fig. 30c compression appears simultaneously in all points of the shell surface. It confirms again that the shell experiences a monopole resonance at this frequency, which was seen also in Fig. 12a. It must be noted, that this resonance is not the lower order resonance discussed earlier in this work, because the acoustic wavelength in the gas inside the shell at this frequency is several times smaller than the shell diameter.

Fig. 31 for the scattered field near the shell reveals an interesting fact. The waves of pressure fluctuations along the shell boundary, observed in the non-resonance case (Fig. 27), are seen here as well. However, in the resonance case these waves increase their amplitude while moving along the shell. This suggests that at the

resonance these waves interact with each other through the shell interior. They lose their energy to the resonant oscillations inside the shell while they are moving along the front left-hand part of the shell, and receive the energy back while they are at the rear right-hand part of the shell. Therefore, the scattered waves radiated backwards are smaller in amplitude than the waves radiated forward (Fig. 29).

This energy transfer can be explained by the phase shift between the incident wave and the shell resonance oscillations. The oscillations of the shell are shifted in phase relative to the incident wave, so that the shell radiates more effectively in the forward direction.

Figure 28. Total acoustic field in the far field zone. The shell is located in the middle of the waveguide. The shell thickness d = 0, wavenumber k = 15.801. Rectangle reveals area shown in Fig. 30.

Figure 29. Scattered acoustic field in the far field zone. The shell is located in the middle of the waveguide. The shell thickness d =0, wavenumber k = 15.801. Rectangle reveals area shown in Fig. 31.
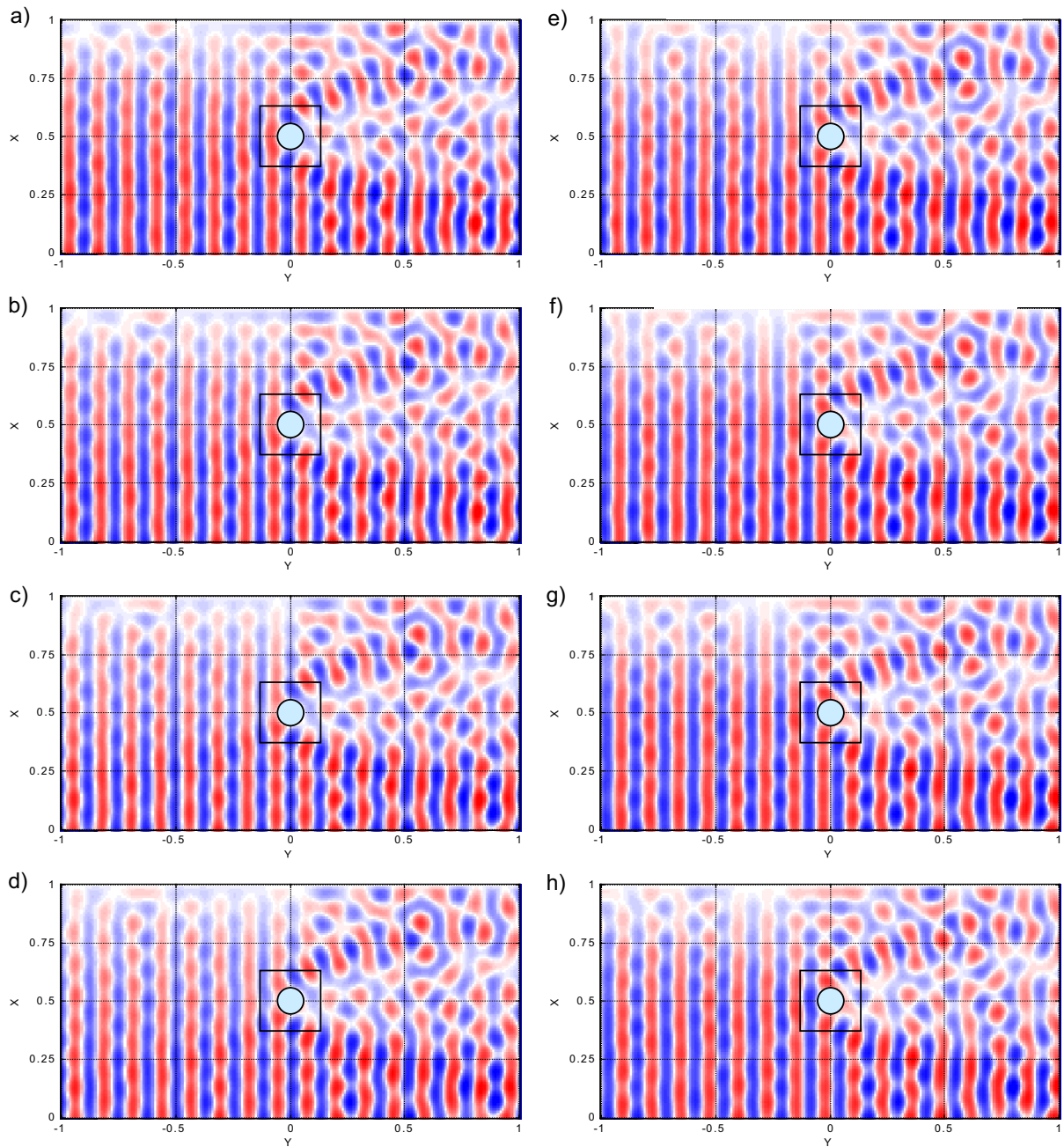
Figure 30. Total acoustic field in the near field zone. The shell is located in the middle of the waveguide. The shell thickness d =0, wavenumber k = 15.801.
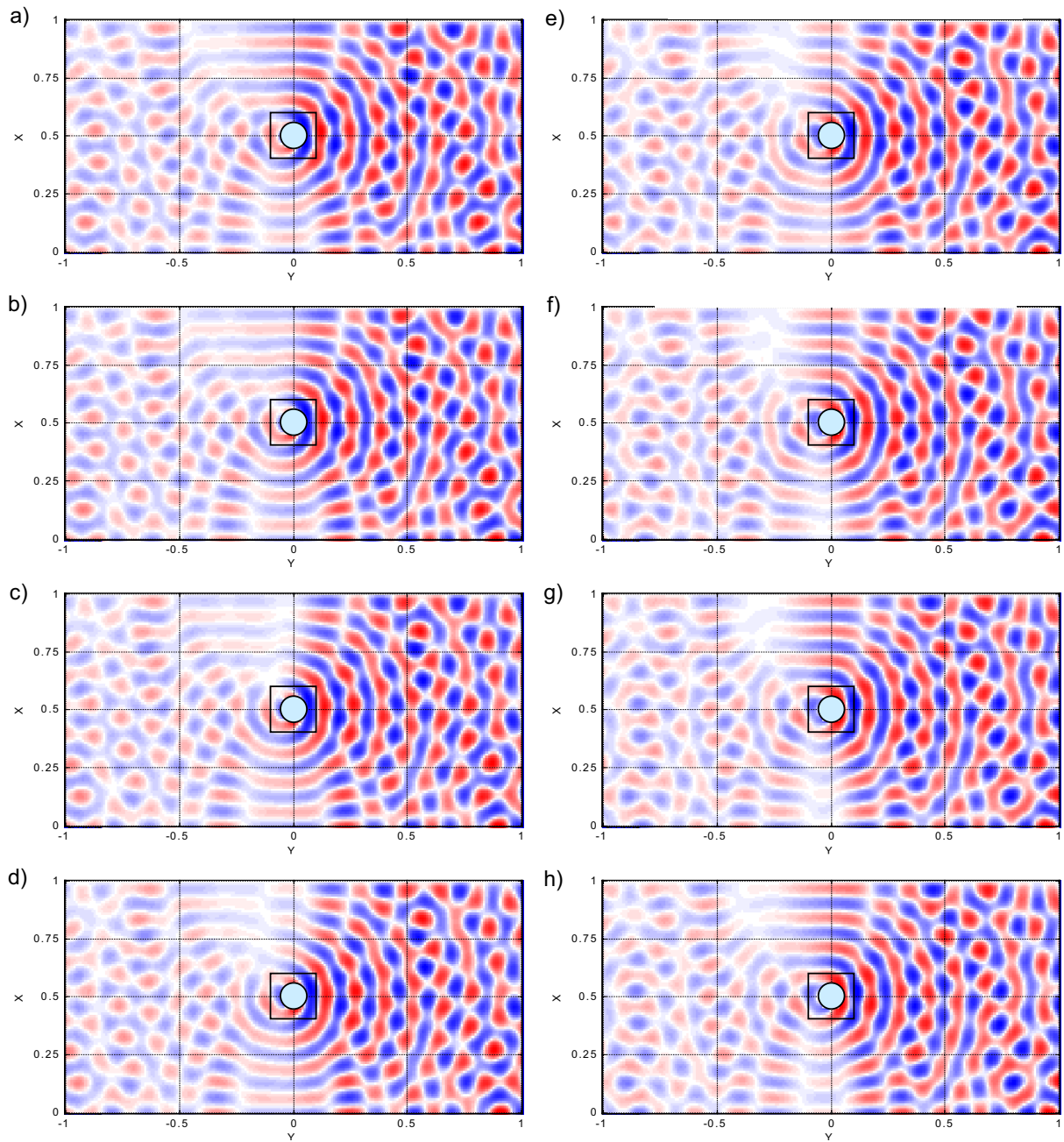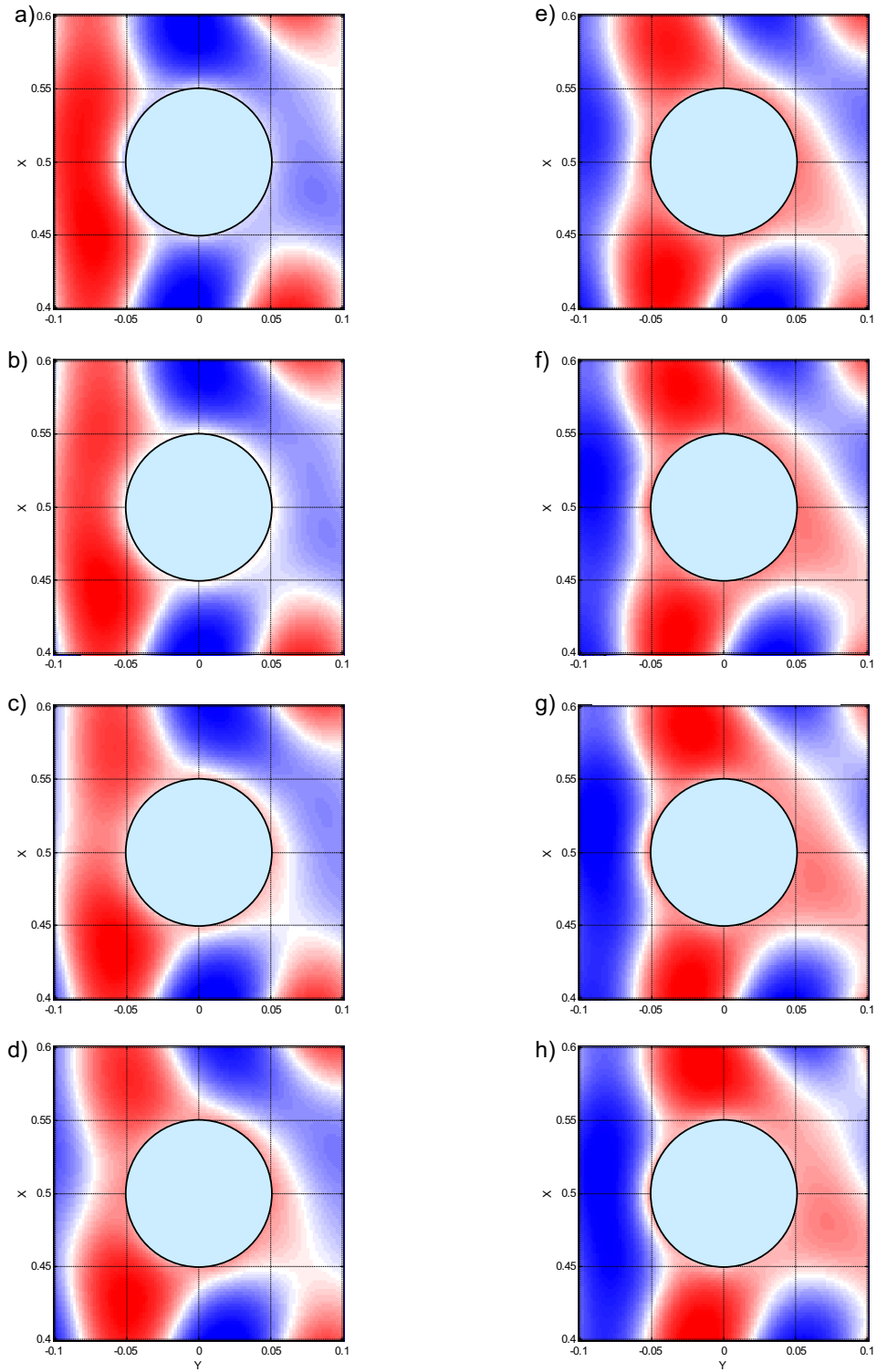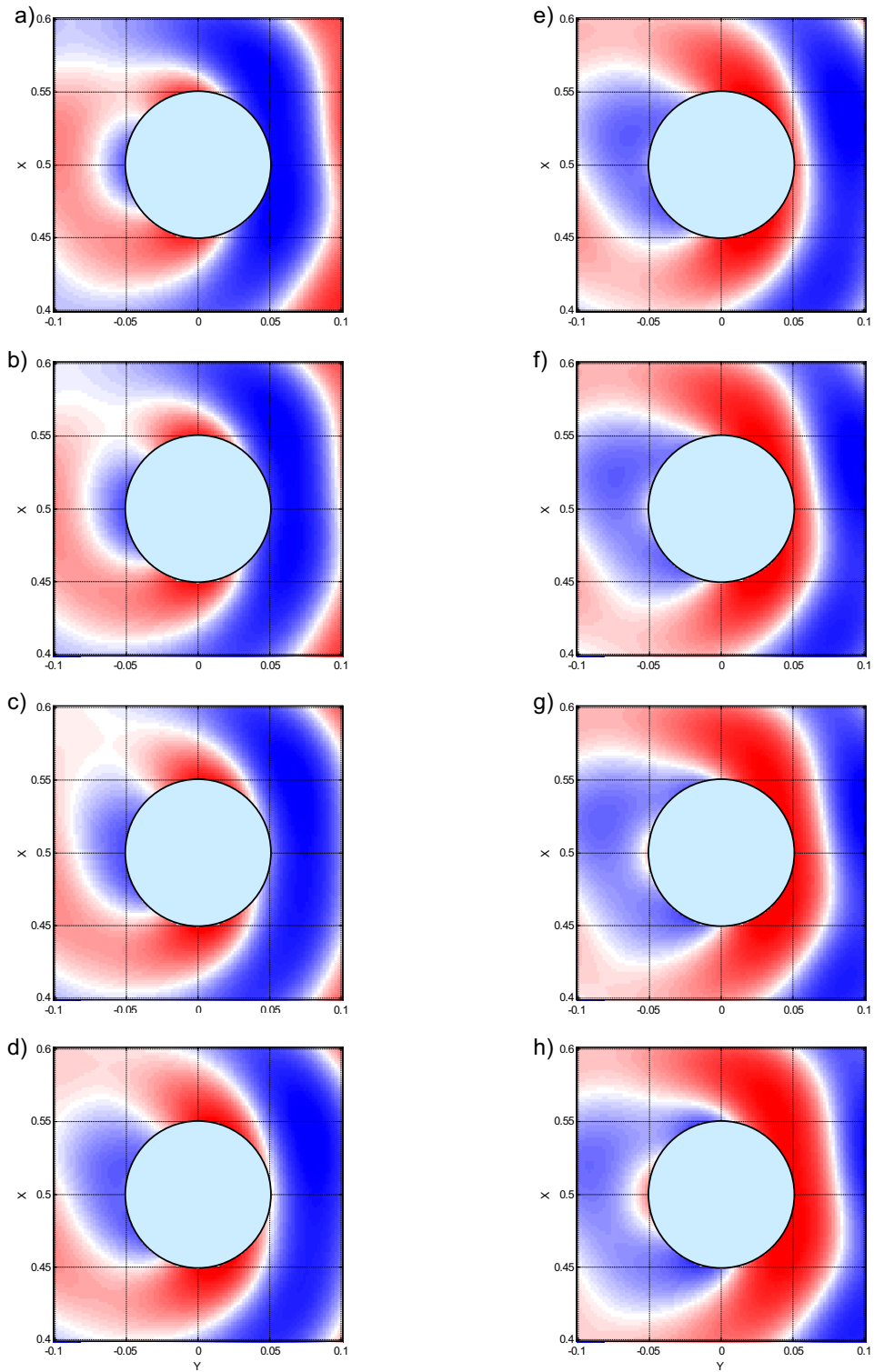
Figure 31. Scattered acoustic field in the near field zone. The shell is located in the middle of the waveguide. The shell thickness d =0, wavenumber k = 15.801.

12.3.1.3 Acoustic Field at the Dipole Resonance.

Figures 32 - 35 show the acoustic field structure for the frequency $k = 25.201$, corresponding to the resonance B in Fig. 12b, which was discussed previously in section 11.3. It was shown that the resonance is split into two close resonances with the corresponding nodal patterns rotated 90 degrees with respect to each other. These resonances correspond to dipoles, one of which has its axis parallel, and the other its axis normal to the axis of the waveguide. Discussion will be confined to the former resonance.

Figures 32 - 35 reveal the same features of the acoustic field as those discussed above for the monopole resonance and the non-resonance case. These features are:
a) vertical wavefronts of the incident field interfering with the higher modes of the scattered field;
b) a shadow behind the shell, which is more distinct in this case due to the smaller wavelength;
c) wavefronts moving backwards near the top boundary of the shell;
d) surface waves around the shell;
e) standing waves between the shell and the waveguide boundaries.

The dipole resonance case also has features similar to the monopole resonance case considered above. In both cases, the shell radiates the acoustic wave mostly in the forward direction (Figs. 29 and 33). However, an area of high amplitude is narrower in the dipole resonance case, because of the smaller wavelength. Another common feature is an increase in the amplitude of the scattered acoustic field near the shell surface while the wave of acoustic sources propagates along the surface (see section 12.3.1.1.2).

The structure of the total acoustic field in the near field zone reveals a major difference between the cases of the monopole (Fig. 30) and the dipole (Fig. 34) resonances. While the field at the monopole resonance is always in the same phase near the shell surface, at the dipole resonance the phase is opposite at the front and the rear half of the shell. Indeed, in Figs. 34a - 34f the phase of compression (red colour) is located before the shell, while the phase of rarefaction (blue colour) is behind the shell. In Figs. 34g,h the phase is changing, but in opposite directions before and behind the shell. The phase agrees with the distribution of the shell velocity amplitude (Fig. 12a).

Another important feature of the dipole resonance is the type of surface waves near the shell. Fig. 34 reveals that, opposite to the non-resonance case, the surface waves are standing, rather than propagating waves. Indeed, in all pictures shown in Fig. 34, the area near the top and the bottom of the shell is always white, which corresponds to a node in the pressure wave. Therefore, a standing wave, rather than a propagating wave, exists near the shell surface. This correlates with the representation of scattering resonances as surface waves, circling the cylinder many times, as discussed in the literature review.

Figure 32. Total acoustic field in the far field zone. The shell is located in the middle of the waveguide. The shell thickness d =0, wavenumber k = 25.201. Rectangle reveals area shown in Fig. 34.

Figure 33. Scattered acoustic field in the far field zone. The shell is located in the middle of the waveguide. The shell thickness $d = 0$, wavenumber $k = 25.201$. Rectangle reveals area shown in Fig. 35.
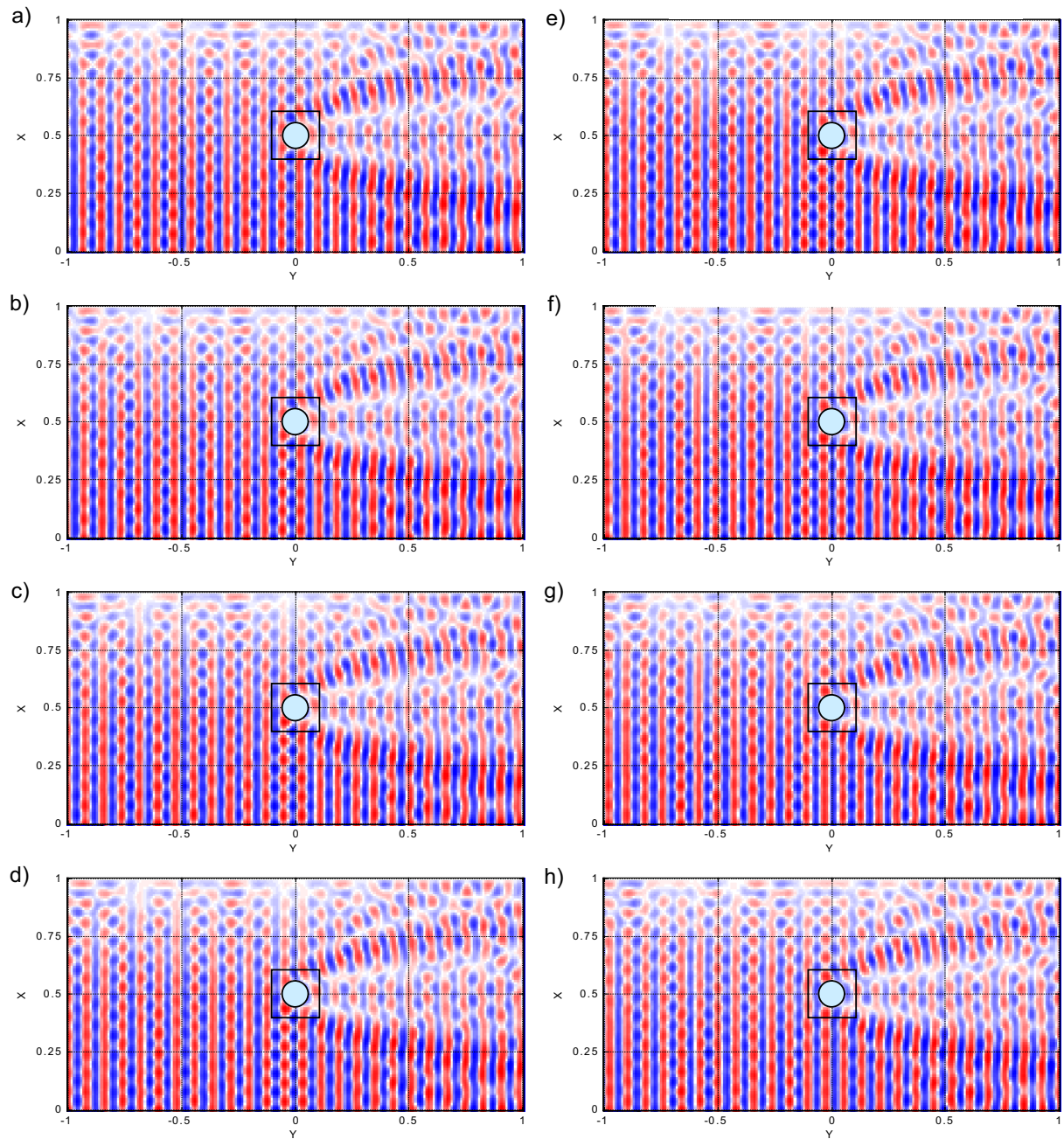
Figure 34. Total acoustic field in the near field zone. The shell is located in the middle of the waveguide. The shell thickness d =0, wavenumber k = 25.201.
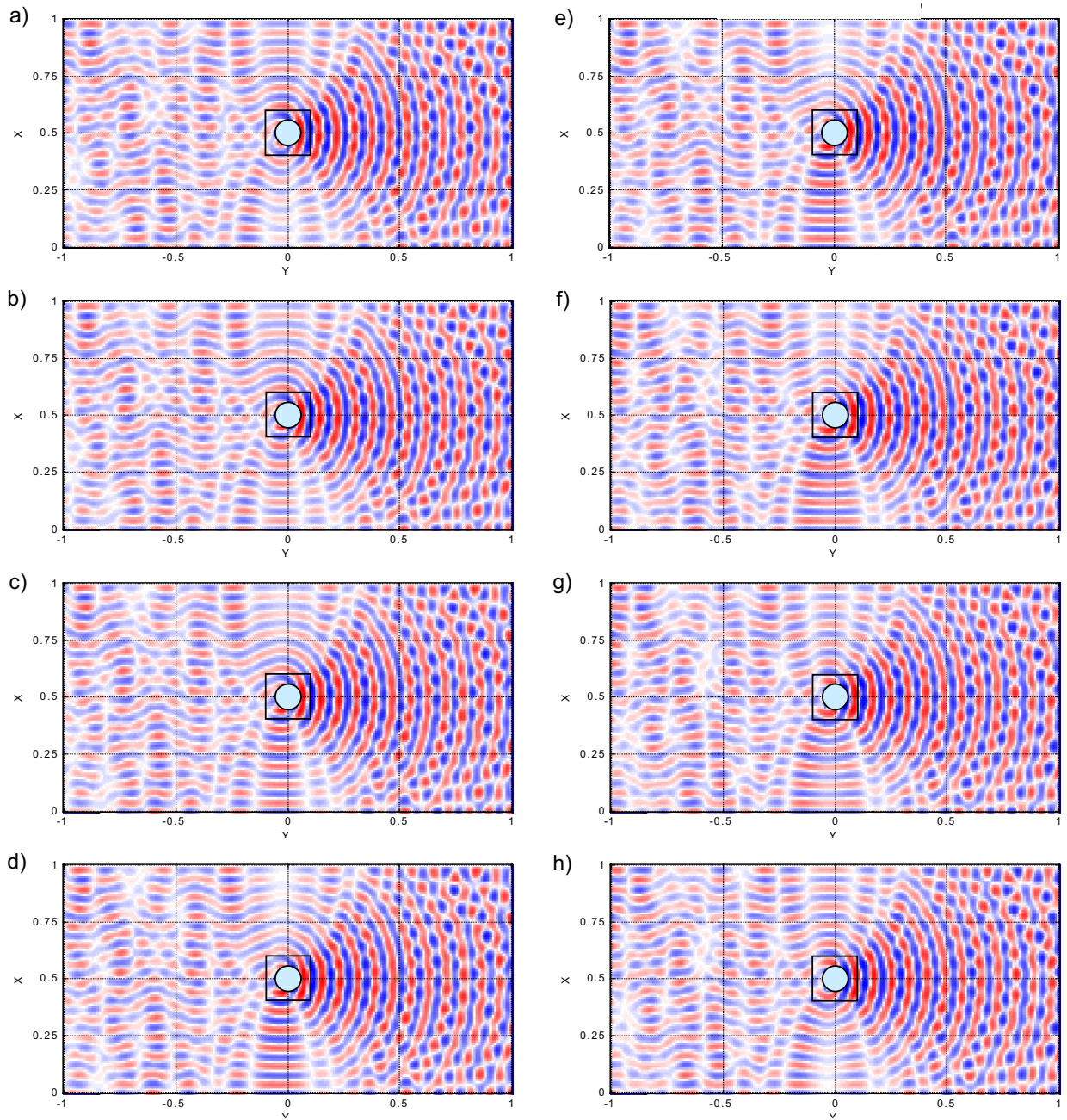
Figure 35. Scattered acoustic field in the near field zone. The shell is located in the middle of the waveguide. The shell thickness $d = 0$, wavenumber $k = 25.201$.

12.3.1.4 Acoustic Field near the Shell with Non-Zero Thickness.

Figures 36 - 39 present the acoustic field structure for the same frequency $k = 25.201$, but for a shell with non-zero thickness $d = 0.01 * R_1$. It was stated in section 11.3, that the resonance at B is not observed for such a shell, so the case considered here corresponds to a non-resonance situation.

The structure of the acoustic field in this case is analogous to the non-resonance case discussed above ($k = 14.701$, $d = 0$). Compared to the resonance case considered in the previous section, the pictures reveal the following differences:
a) The scattered field has approximately the same amplitude in all directions.
b) Pressure waves propagate around the shell surface.
c) The waves of acoustic sources do not change their amplitude while propagating around the surface.
d) The pressure amplitude on the shell surface is very small due to softness of the shell at this frequency. (The shell thickness is only 0.01 of its outer radius R_1).

Figure 36. Total acoustic field in the far field zone. The shell is located in the middle of the waveguide. The shell thickness $d = 0.01 * R_1$, wavenumber $k = 25.201$. Rectangle reveals area shown in Fig.38.

Figure 37. Scattered acoustic field in the far field zone. The shell is located in the middle of the waveguide. The shell thickness d = 0.01 * R₁, wavenumber k = 25.201. Rectangle reveals area shown in Fig.39.
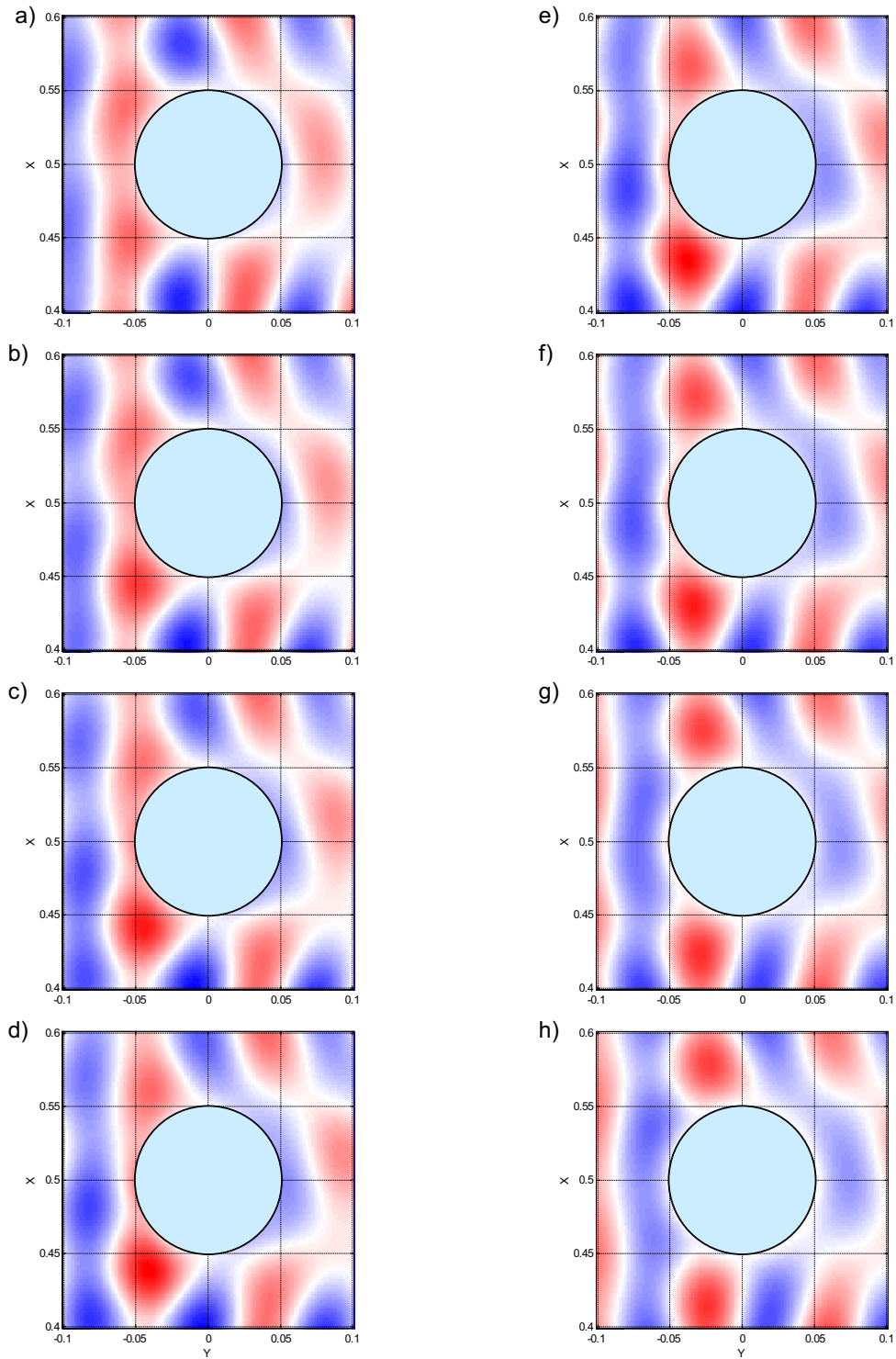
Figure 38. Total acoustic field in the near field zone. The shell is located in the middle of the waveguide. The shell thickness $d = 0.01 * R_1$, wavenumber $k = 25.201$.
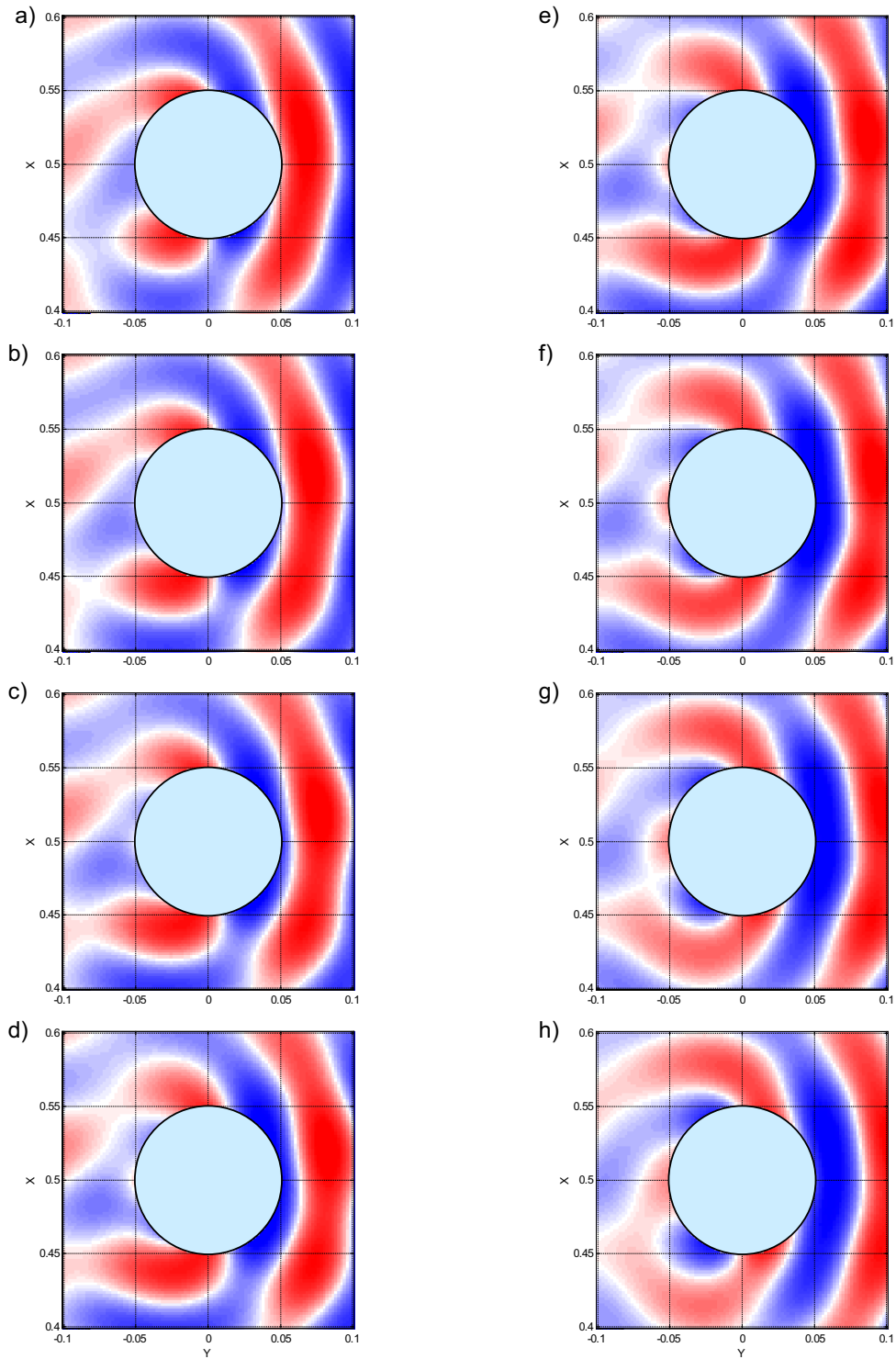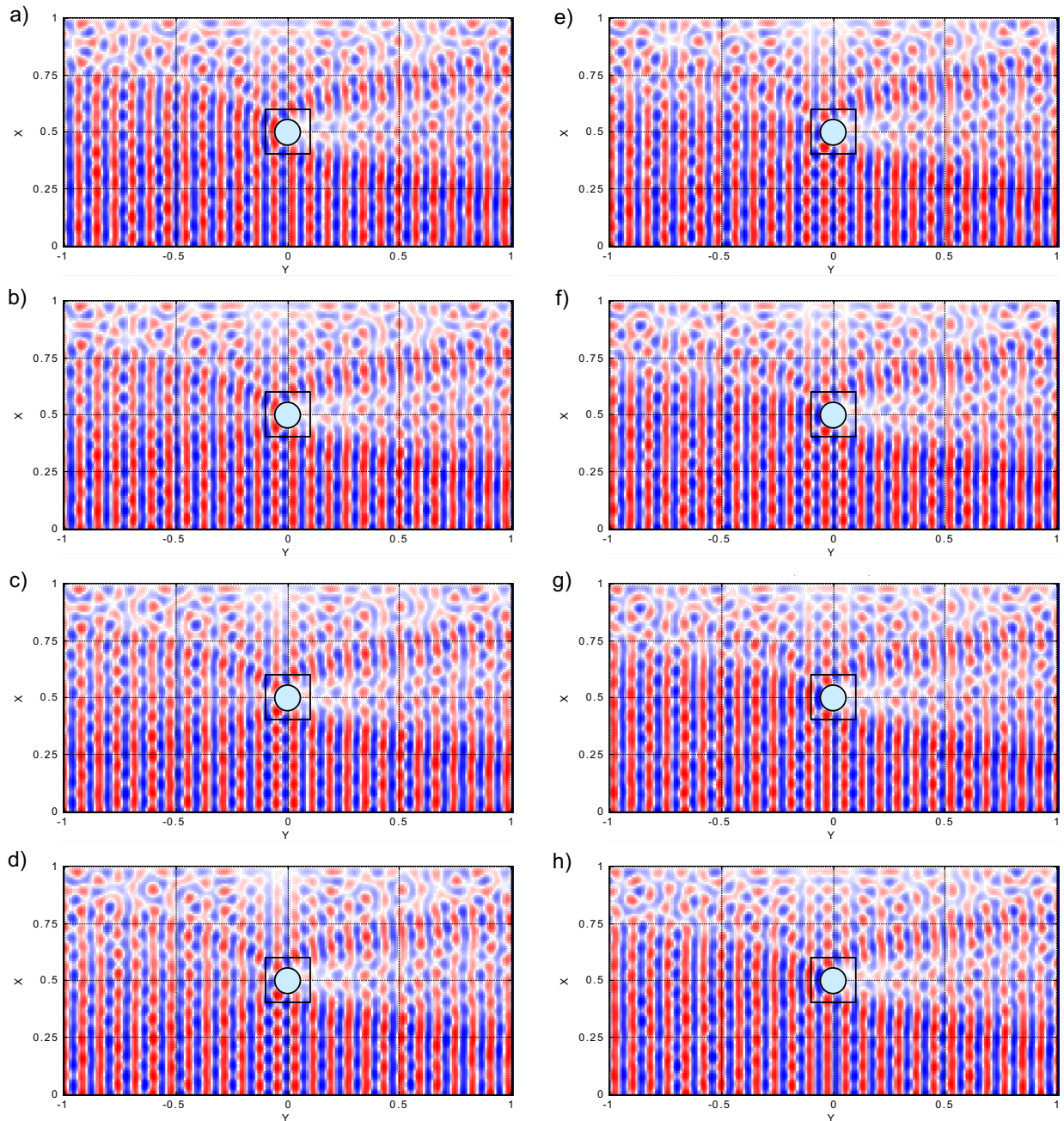
Figure 39. Scattered acoustic field in the near field zone. The shell is located in the middle of the waveguide. The shell thickness $d = 0.01 * R_1$, wavenumber $k = 25.201$.

12.3.1.5 Differences between Resonant and Non-Resonant Fields.

Comparison of two resonance cases and two non-resonance cases, carried out above, allows the formulation of differences in the acoustic field structure for resonance and non-resonance cases in the middle frequency range.

Table 3.

Differences between resonant and non-resonant fields in the middle frequency range for the two-dimensional elastic cylindrical shell.

Non-resonant scattering	**Resonant scattering**
Scattered acoustic field is radiated almost equally in all directions	Scattered acoustic field has distinct maxima in some directions and minima in other directions
Propagating waves are observed near the shell surface in the total field structure	Standing waves are observed near the shell surface in the total field structure
Waves of acoustic sources, propagating along the shell surface, do not change their amplitude	Waves of acoustic sources, propagating along the shell surface, change their amplitude

The differences shown in Table 3 reveal the importance of internal resonances of the scattering object for the formation of the acoustic field. The resonances discussed in this section are associated with the internal oscillations of the scattering shell. However, in a waveguide, there can exist resonances of other types, caused by the reflection of waves from the waveguide boundaries. The acoustic field structure at one of such resonances is discussed in the next section.

12.3.2 Acoustic Field in the Case of the Shell Located near the Waveguide Bottom.

Scattering resonances associated with the strong oscillations of the shell can also be observed in an unbounded fluid. For example, some of these resonances were shown in the articles discussed in the literature review. However, when scattering occurs in a waveguide, other resonance phenomena can be observed as well.

The frequency $k = 25.201$ corresponds to a wide maximum in the reflection coefficient for the shell located near the bottom (Fig. 13d). Figs. 40 - 43 show the acoustic field structure for this case. The figures allow understanding the physical meaning of this resonance.

Fig. 40 shows distortions in the acoustic field caused by the scattered field. The structure of the scattered field in the far field zone is revealed in Fig. 41. It is seen that the distribution of the scattered field has maxima in some directions, and minima in other directions, which is similar to the resonance case discussed above.

Fig. 42 depicts the total acoustic field in the near field zone. Again, the surface waves are seen propagating along the boundary of the shell. However, in contrast to the field structure for a thin shell (Fig. 38), the acoustic field amplitude is not zero at the shell boundary. The shell thickness is larger in this case, and the shell behaves more like a rigid object, rather than a soft object.

The most interesting feature of Fig. 42 is the reflections of the pressure waves between the waveguide bottom and the shell. Indeed, the time evolution of the pressure field clearly shows a maximum of pressure in the front lower part of the shell. This maximum is reflected from the waveguide bottom first (Fig. 42c,d), then it is reflected from the shell (Fig. 42e,f), and eventually comes back to the waveguide bottom (Fig. 42g,h). In the structure of the scattered field (Fig. 43) this phenomenon corresponds to a standing wave. These multiple reflections of the acoustic wave from the shell and the waveguide bottom are a specific type of resonance, which can be observed only in a waveguide. This resonance appears as the maximum on the reflection coefficient curve (Fig. 13d), and as a maximum of the shell vibrational velocity in the lower part of the shell (Fig. 13c).

The mechanism of the increased reflection at this frequency can also be explained by means of energy vortices. It is suggested, that the mode interference near the lower part of the shell leads to formation of an energy vortex, similar to the vortex shown in Fig. 10h. This vortex blocks the lower part of the waveguide for the incoming acoustic energy, thus increasing the scattering cross-section of the shell.

Figs. 40 - 43 reveal another important role of the higher-order waveguide modes. These modes represent a mechanism for the interaction between the scattering object and the waveguide

boundaries. The calculation of the scattering characteristic in the case of the shell near the boundary is made possible only by use of the Multi-Modal Integral Method, which takes into account the higher waveguide modes up to infinite order.

Figure 40. Total acoustic field in the far field zone. The shell is located near the bottom of the waveguide. The shell thickness d = 0.05 * R₁, wavenumber k = 25.201. Rectangle reveals area shown in Fig 42.
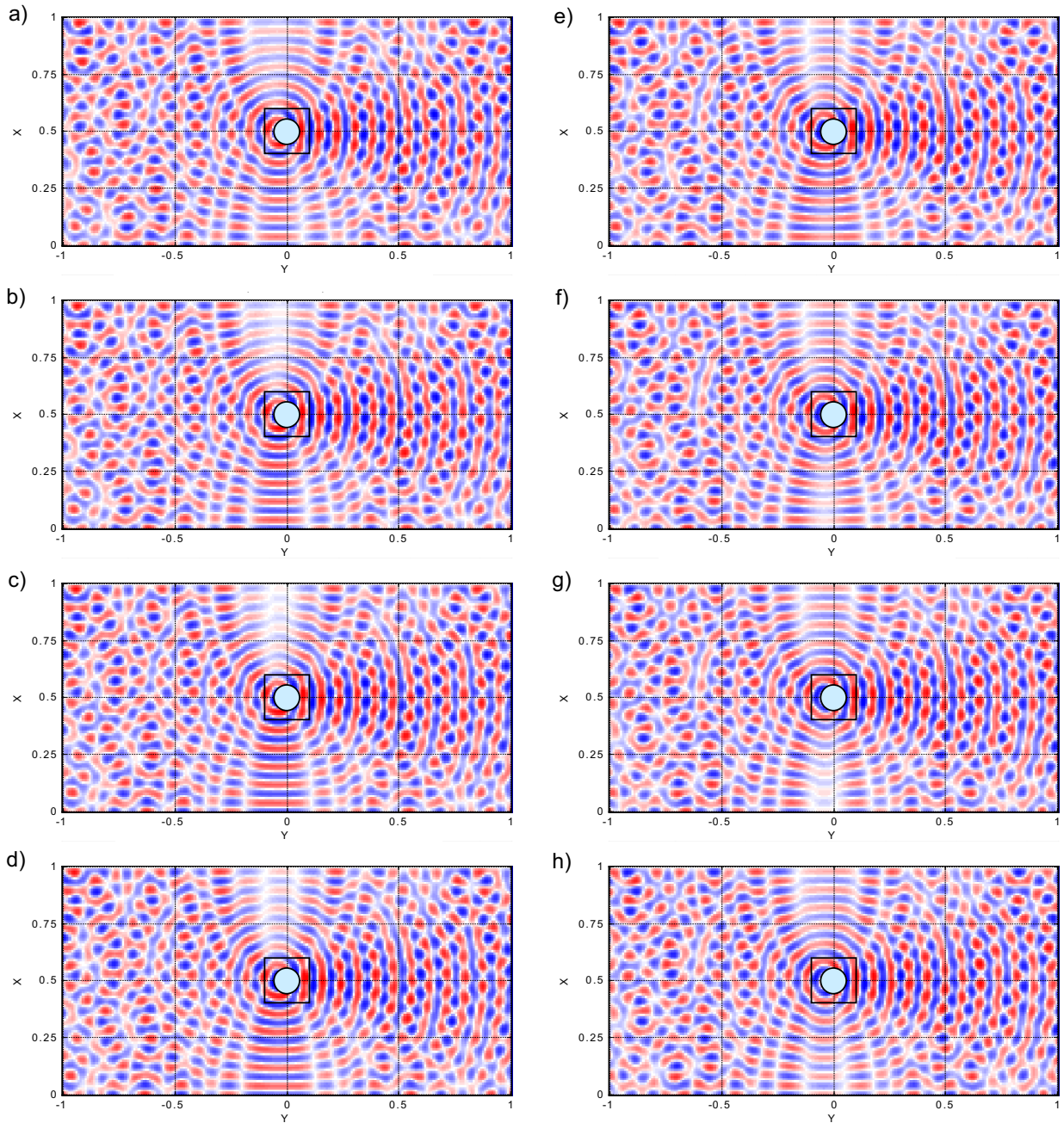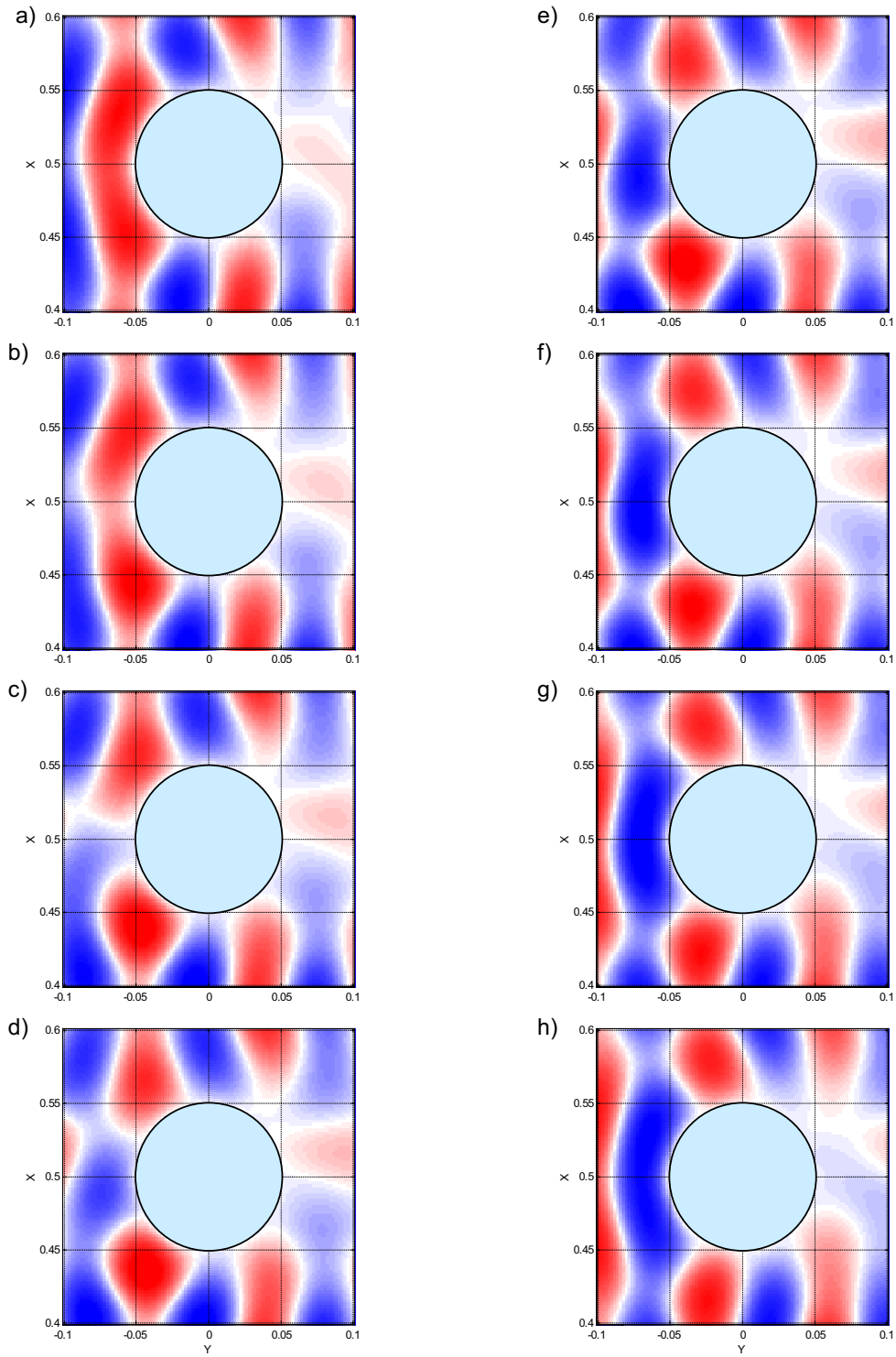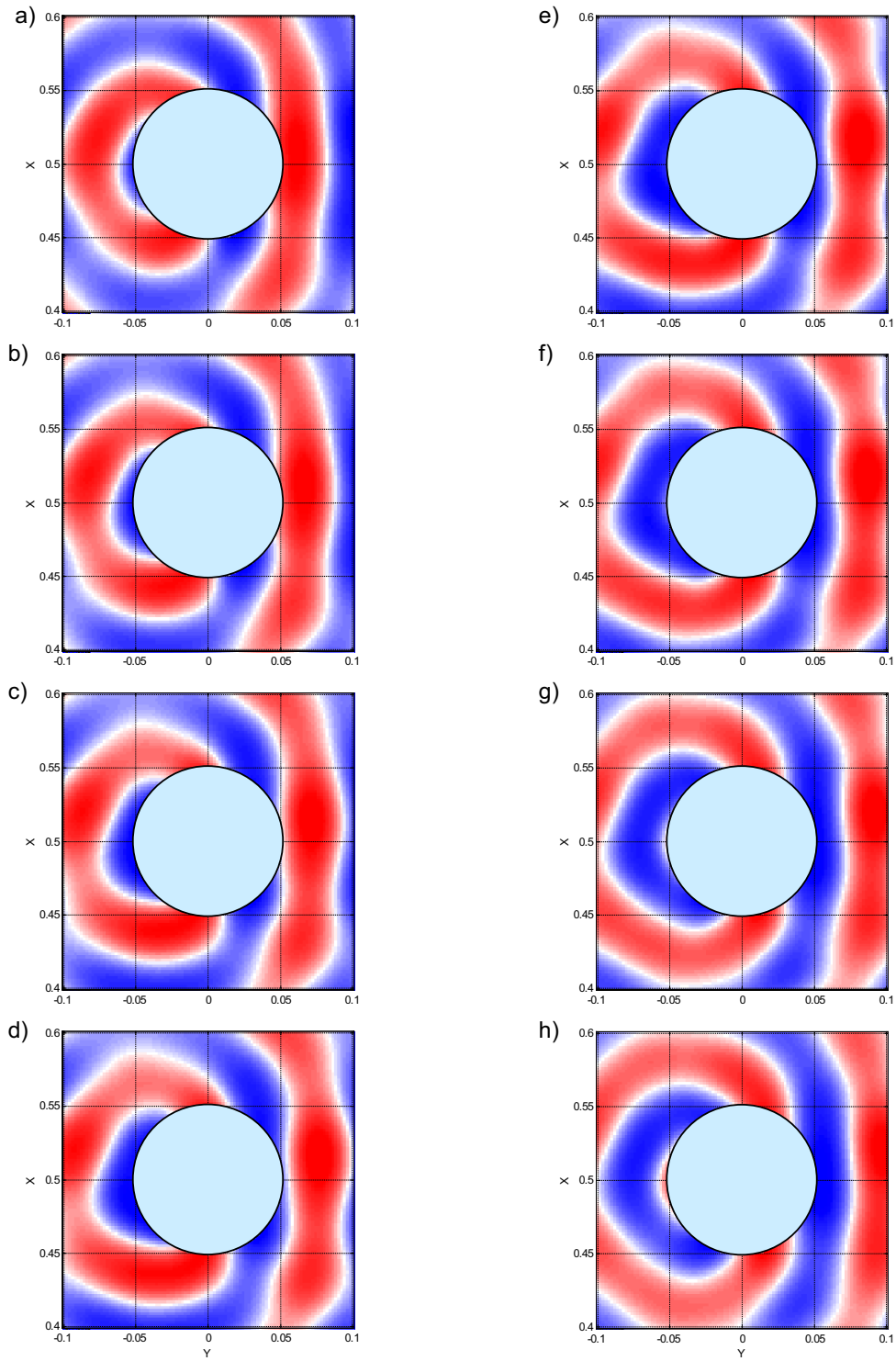
Figure 41. Scattered acoustic field in the far field zone. The shell is located near the bottom of the waveguide. The shell thickness $d = 0.05 * R_1$, wavenumber $k = 25.201$. Rectangle reveals area shown in Fig. 43
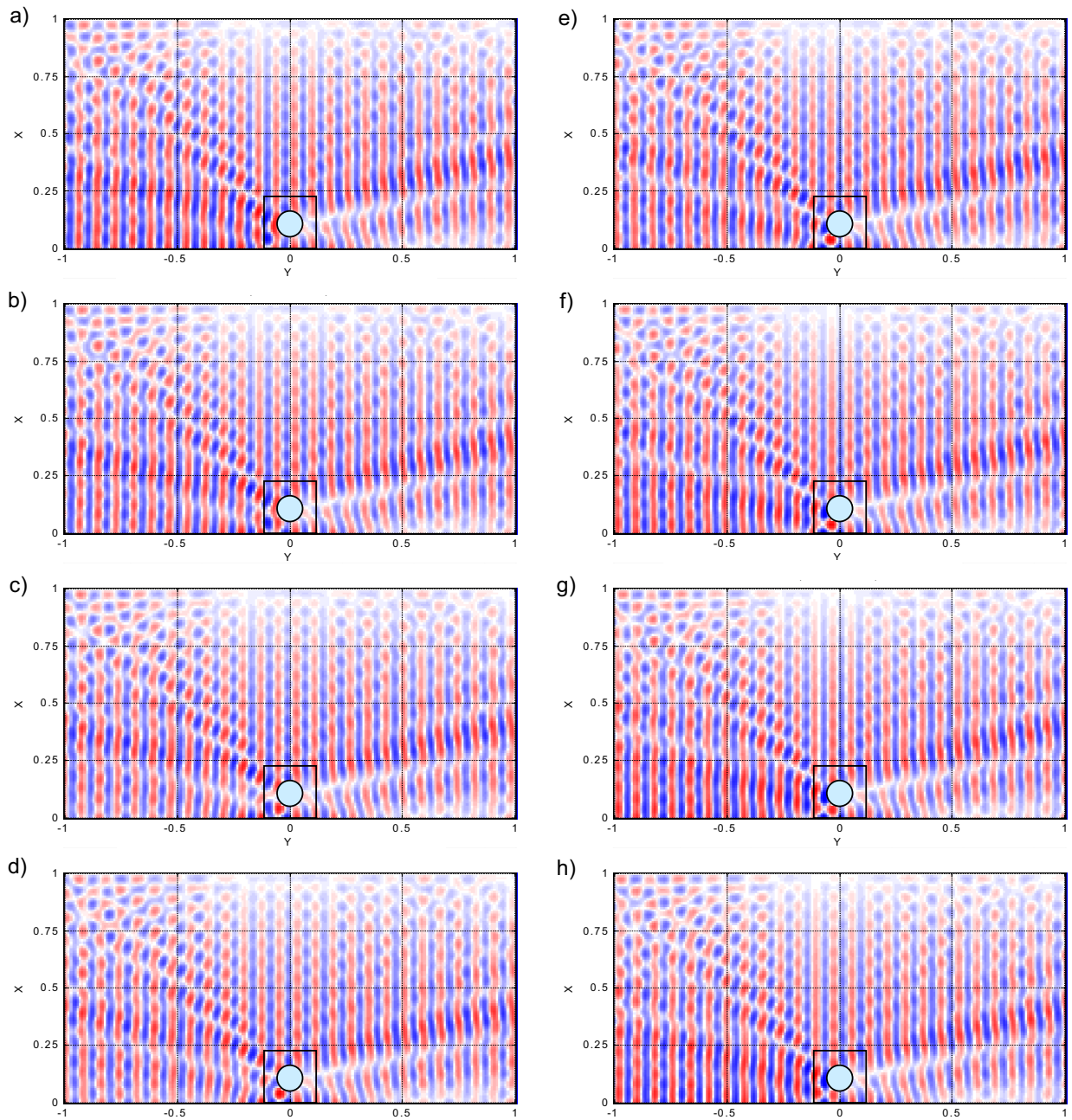
Figure 42. Total acoustic field in the near field zone. The shell is located near the bottom of the waveguide. The shell thickness $d = 0.01 * R_1$, wavenumber $k = 25.201$.
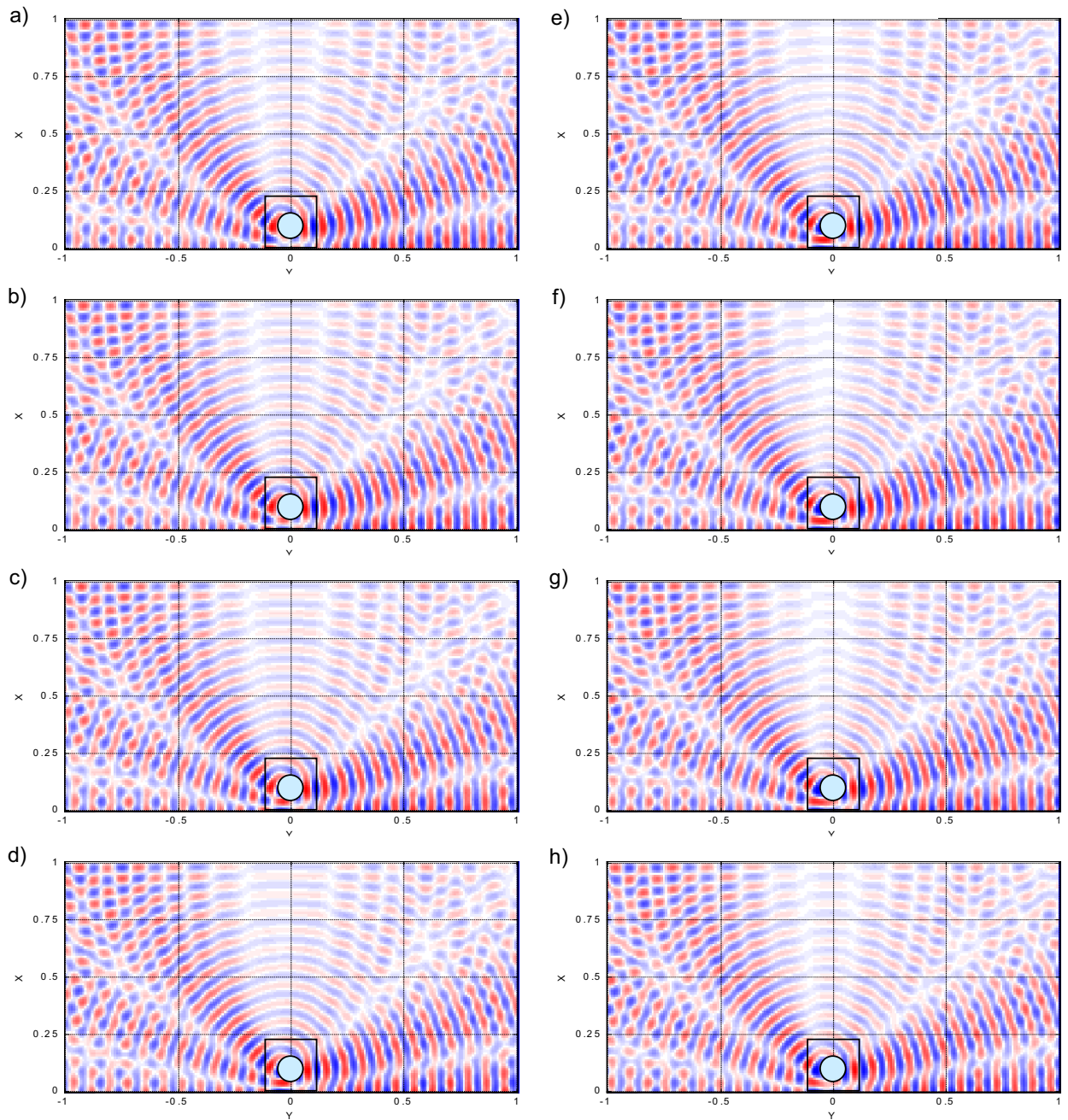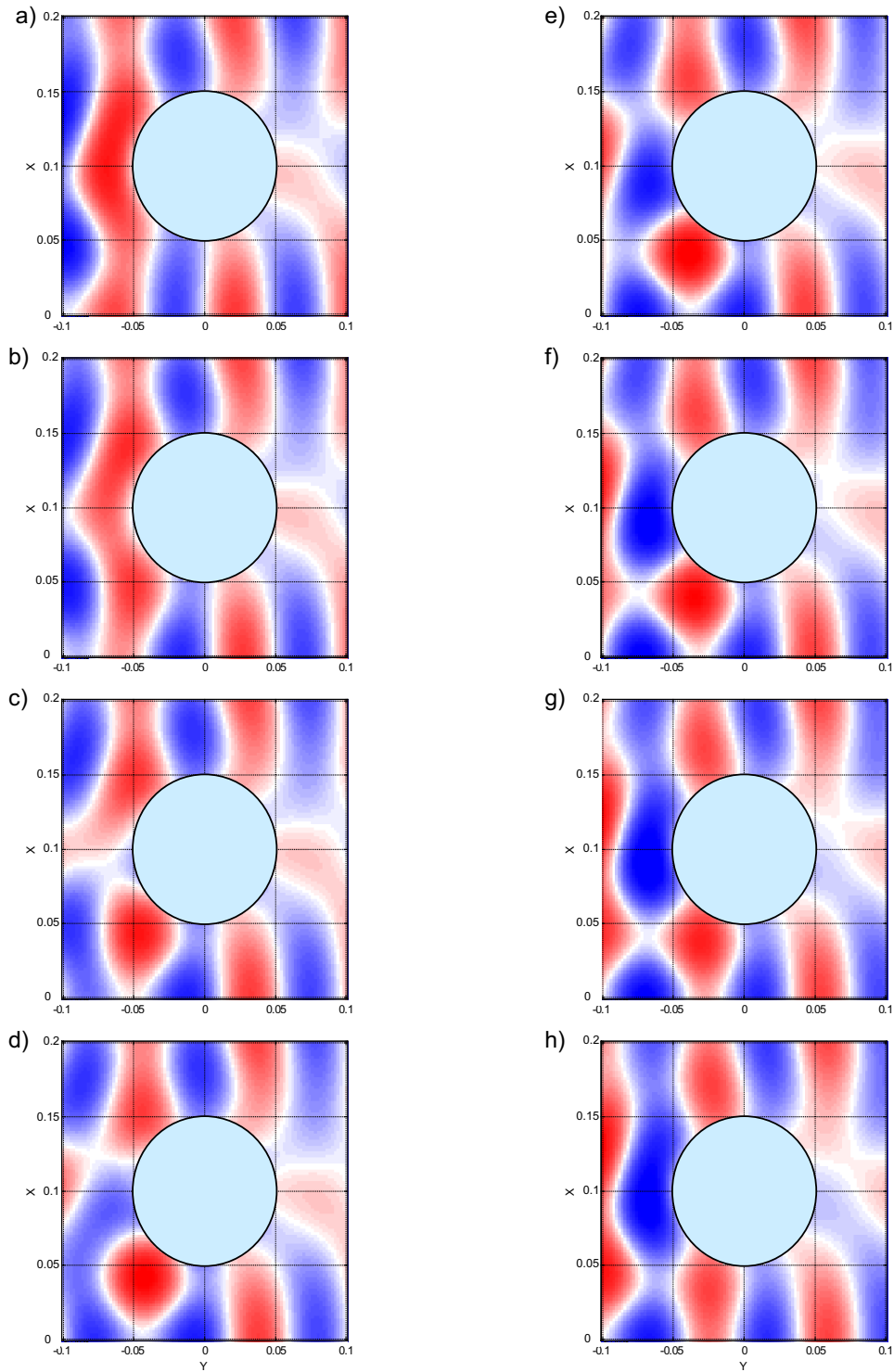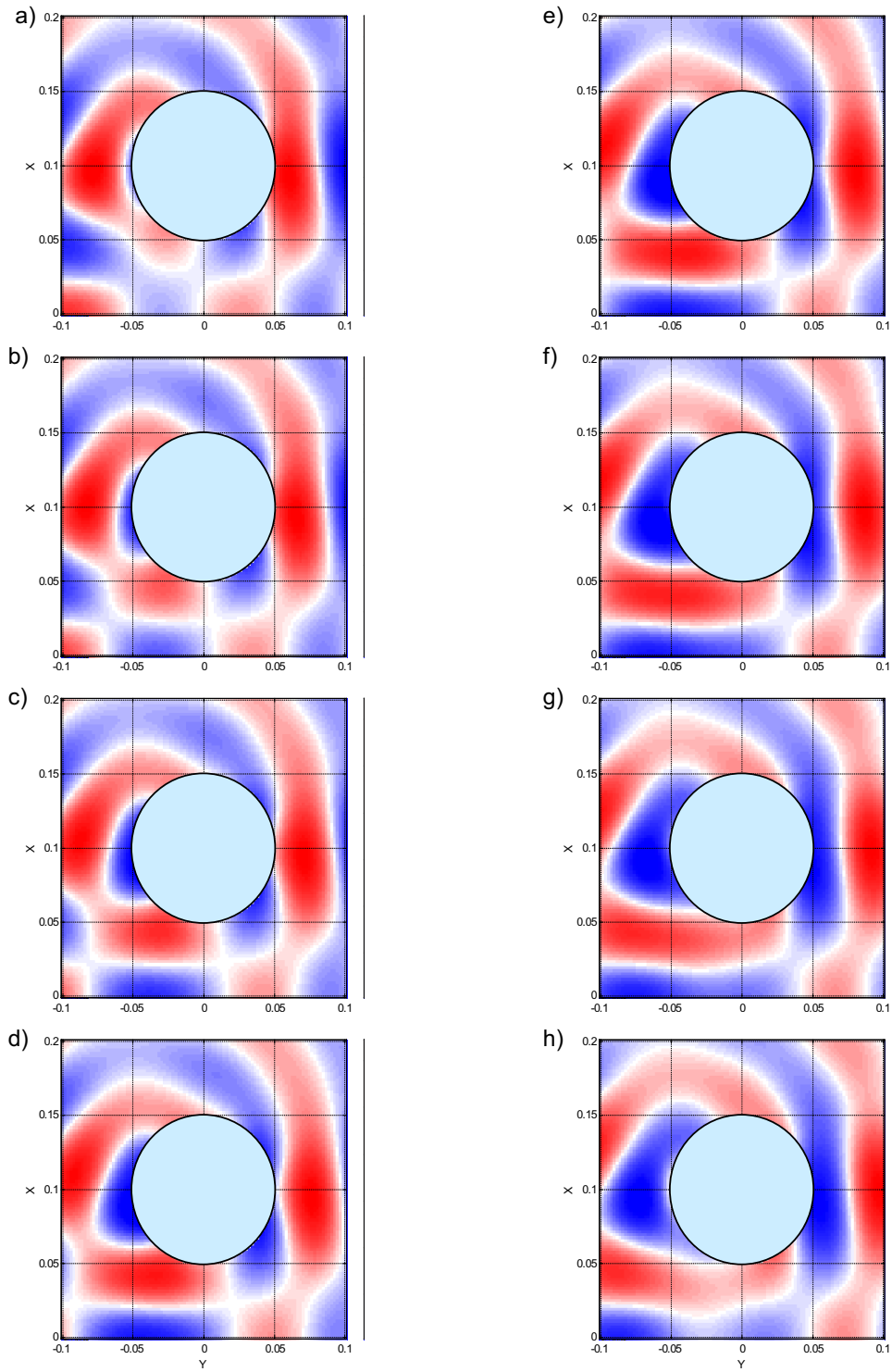
Figure 43. Scattered acoustic field in the near field zone. The shell is located near the bottom of the waveguide. The shell thickness d = 0.05 * R₁, wavenumber k = 25.201.

12.4   Conclusion.

Time evolutions of the total and the scattered pressure fields are presented and analysed in this chapter. The calculations are carried out for several values of the shell thickness, several locations of the shell in the waveguide, and in several frequency ranges.

At the frequency just above the critical frequency of the lowest waveguide mode, the scattered field has a strong vertically directed dipole component, which is caused by vertical movement of fluid particles in the incident field. For the shell with zero wall thickness, a monopole component also exists. Interference between the two components leads to propagation of waves of acoustic pressure along the shell boundary from the top to the lower part of the shell.

At higher frequencies near the lowest order monopole resonance of a thin shell, a strong monopole component of the scattered field is detected. Yet, the surface waves also exist, but propagate from the front to the rear part of the shell, rather than from the top to the bottom, which is explained by the direction of the wave vector of the incident wave.

At resonance, the incident field leads the scattered field by a quarter of a cycle. At a frequency well above the resonance, this lead approaches half a cycle. These results correspond to previously obtained results (Donskoi *et al. 1990*) for oscillations of an air-filled cavity near a piston.

In the middle frequency range, the waves of acoustic pressure along the shell boundary also exist. Due to the existence of these waves, wavefronts of the scattered wave have a circular shape near the shell. These circles are destroyed in the far field zone by interference of waves travelling by different acoustic paths. An area of indistinct shadow is revealed behind the shell. It is shown that near the top boundary the phase speed can be directed oppositely to the incident wave, which can lead to the appearance of energy vortices.

At a resonance frequency of the internal oscillations of the shell, the waves of pressure propagating along the shell boundaries increase in amplitude as they propagate. This peculiar feature of resonance scattering is explained by the energy exchange between the surface waves, which occurs through the resonance oscillations of gas inside the shell. The waves in the total field structure, opposite to the non-resonance case, are standing, rather than propagating.

If the shell is located near a waveguide boundary, the acoustic wave experiences multiple reflections between the shell and the boundary. This leads to a maximum in the frequency dependence of the reflection coefficient. In addition, this phenomenon shows the important role of the higher-order waveguide modes in the interaction between the shell and the waveguide boundaries.

13 Target Strength and Its Application to Waveguide Systems.

One of the parameters that is most often used in measuring efficiency of reflection of a plane acoustic wave by elastic objects in the ocean is the target strength TS, that may be defined as

$$TS = 10 \log \frac{I_r}{I_i} \tag{84}$$

where I_r is the intensity of the reflected wave referenced to one metre distance from the acoustic centre of the target, and I_i is the incident wave intensity (Urick, 1983).

However, as the above analysis shows, the use of *TS* is not appropriate for a shallow ocean when the acoustic field is clearly dependent upon the modal structure. First, the reflection depends not only on the geometrical shape of the object, but also on the location of the object in the waveguide and the resonance properties of the object. Second, the rate of amplitude decrease with increasing distance from the target differs for different waveguide modes. Third, in the immediate proximity of the object the higher exponentially damping waveguide modes with imaginary g_n give significant contributions to the total acoustic field. Fourth, the reflection will depend on the location of the source, because the modal composition of the incident wave described by the Green's function depends on the source coordinates.

For all these reasons, the target strength does not characterise fully the reflective properties of the object inside the waveguide. In this case, the object can be described by the scattering matrix, containing coefficients of transformation of the modes in the incident wave to the modes in the reflected wave. The reflection coefficient similar to the one calculated above can also be used to describe overall reflection in the waveguide.

14 Accuracy of the Multi-Modal Integral Method.

14.1 Introduction.

The accuracy of the calculations is an important issue in dealing with numerical modelling. As it is stated above, the Multi-Modal Integral (MMI) Method, developed and used in this work, provides the exact solution to the scattering problem. The boundary value problem has been solved analytically and any direct solution of differential equations by means of numerical algorithms is not required. However, the exact solution is achievable as a limit of quickly converging series and the accuracy of this solution must be evaluated. In addition, some numerical calculations are needed in the MMI method to perform two tasks, namely: a) calculation of the coefficients of the system of linear equations, and b) solution of the system.

This chapter discusses the accuracy of the solution provided by the MMI method and means of accuracy control. Two main techniques used in accuracy control are the correct truncation of the system matrix and the correct total power balance of the incident and the scattered waves.

14.2 Matrix of the System of Linear Equations (the Scattering Matrix).

As was shown above in Section (8.3.4), the boundary value problem, formulated in this work, was reduced to a system of linear equations. The system can be written as:

$$\left\|\mathbf{\hat{M}}\right\|\vec{\mathbf{b}} = \vec{\mathbf{a}} , \tag{85}$$

where the vector $\vec{\mathbf{a}}$ describes the modal composition of the incident field, the vector $\vec{\mathbf{b}}$ components are the Fourier coefficients of the distribution of acoustic sources on the surface of the scattering cylinder, and $\left\|\mathbf{\hat{M}}\right\|$ is the scattering matrix. Eq. (85) is another form of Eq. (61), where the matrix $\left\|\mathbf{\hat{M}}\right\|$ is determined as the sum of the matrix $\left\|\mathbf{M}\right\|$, defined by Eq. (63), and the unity matrix $\left\|\mathbf{E}\right\|$:

$$\left\|\mathbf{\hat{M}}\right\| = \left\|\mathbf{M}\right\| + \left\|\mathbf{E}\right\| . \tag{86}$$

The system of equations (85) is infinite in number of equations and unknown variables. Therefore, the implementation of the method requires truncation of the matrix at some index $m_{\max}$. The indices in the matrix $\left\|\mathbf{\hat{M}}\right\|$ range from $-\infty$ to $+\infty$, so that the number of equations of the truncated system is equal to $2m_{\max} + 1$.

14.2.1 Truncation of the Scattering Matrix and the Green's function.

One of the main advantages of the Multi-Modal Integral Method in comparison with existing methods is the fact that the matrix $\left\|\hat{\mathbf{M}}\right\|$ can be truncated easily without losing information about the scattering process. This feature is due to the modification of the waveguide's Green's function, as carried out in Section (8.3.3). The new form of the Green's function takes into account all the waveguide modes up to infinite order by separating asymptotic terms and summing them in a convenient analytic form. Due to this fact, the scattering matrix $\left\|\hat{\mathbf{M}}\right\|$ contains all the information about the scattering process in its central part, where the absolute value of the matrix indices, $|m|, |p| < m_{max}$. The exact value of m_{max} depends upon the frequency and the configuration of the waveguide.

14.2.2 Determining of the Matrix Dimension in Numerical Experiments.

The values of m_{max} in the numerical experiments were determined in the following way. For every configuration of the waveguide in every frequency range, the problem was solved sequentially for different values of the matrix dimension until the results stopped changing significantly when m_{max} was increased further. Subsequent calculations in that frequency range were carried out using this value of m_{max}.

The efficiency of the Multi-Modal Integral Method is confirmed by small values of m_{max} needed to obtain results in the situations considered in this work. All calculations for the case of the scattering by homogeneous cylinders considered in Chapters 9 and 10 required only $m_{max} = 4$. The calculations for the case of a gas-filled shell in the Chapter 11 required two values of m_{max}. At low frequencies, where non-dimensional wavenumber k is less than 10, m_{max} is equal to 9. At higher frequencies, where $10 \lesssim k \lesssim 32$, the value of m_{max}, used in the calculations, was 13. Such small size matrices allow the solution of scattering problems on computers with relatively small resources.

14.2.3 Examples of the Scattering Matrix.

Figures 44 – 52 show scattering matrices for the cases of homogeneous cylinders and an elastic shell as scattering objects, which were discussed in Chapters 9, 10, and 11. The horizontal and vertical coordinates are the matrix indices. The colour bar in each picture represents the colour scale of the picture. The numbers near the colour bar show the logarithm to the base 10 of the absolute value of a matrix element corresponding to each colour.

14.2.3.1 Scattering Matrices for Homogeneous Cylinders.

Figures 44 - 49 show the matrices for the case of one and two homogeneous cylinders as scattering objects. The parameters of the system used in the calculations are shown in Section 9.2.

14.2.3.1.1 Matrices for Scattering by One Cylinder.

Figure 44 shows matrices for one cylinder located in the middle of the waveguide at frequencies outside the frequency range of the resonances of the waveguide and of the scattering object. It is seen clearly that all elements different from zero are located in the central region of the matrix and on its main diagonal. It is seen also that the required size of the matrix increases with frequency, but in the considered frequency range all non-zero matrix elements are located within the square $-4 \le m, p \le 4$.

Elements on the main diagonal behave differently when the matrix indices increase: they tend to unity, rather than to zero. This represents the fundamental fact that all higher cylindrical modes of the incident field are scattered independently of each other. This observation shows that it is possible to truncate the matrix. Unity on the main diagonal provides a value, which is much larger than the values of other non-diagonal elements in every row, so that these elements may be neglected.

Figure 45 shows matrices for frequencies near the critical frequencies of the waveguide modes $k = n + 0.5$. The common characteristic for these matrices is their larger size when compared with the non-resonant matrices in Fig. 44. This can be explained by more efficient interaction between cylindrical modes of the acoustic field. At a critical frequency of a waveguide mode, acoustic energy in this mode propagates in the vertical direction, which facilitates multiple reflections from the waveguide walls.

The matrices for the resonance frequencies of the scattering object are shown in Fig. 46. Every matrix, shown in Fig. 46, corresponds to a resonance in the acoustic source distribution on the surface of the cylinder in Fig. 9a.

The size of these matrices is approximately the same as the size of the non-resonant matrices in Fig. 44. However, these matrices have another interesting feature: two of the diagonal elements with the opposite values of the matrix indices are very small compared to unity. In Figs. 46a,b,c these elements correspond to indices $m, p = \pm2, m, p = \pm3, m, p = \pm4$ respectively. In physical terms, this means that the corresponding modes in the scattered field have high amplitudes. Observe that every row in the matrix represents a linear equation, where the right-hand part is the non-zero amplitude of a component of the incident field. The left-hand part of the equation is a product of the mode amplitude and a small value of the matrix element. (Other terms in the equation may be neglected.) The solution of such an equation is the mode amplitude, which is much

bigger than the solutions of the other equations, where diagonal elements are close to unity or even larger.

Fig. 9a confirms that the second, the third, and the fourth modes of the cylinder have resonances at these frequencies. This fact provides a way for finding resonance frequencies of a scattering object. These frequencies can be identified as frequencies where diagonal elements of the scattering matrix are small.

14.2.3.1.2 *Matrices for Scattering by Two Cylinders.*

Figures 47 - 49 show scattering matrices for the case of two cylinders located in the middle of a waveguide one behind the other. It is clearly seen that the size of these matrices is twice as big as the size of the previously considered matrices for one cylinder. Matrices in Figs. 47 - 49 consist of four quadrants in which the elements are different from zero. Matrix elements in quadrants 2 and 4 (along the main diagonal of the matrix) mathematically describe the interaction of the two cylinders with themselves. The matrix elements in quadrants 1 and 3 describe the interaction between cylinders. For example, quadrant 1 describes the contribution of the incident acoustic field, scattered by the *first* (left) cylinder, to the pressure disturbances on the surface of the *second* (right) cylinder.

The matrices for two cylinders also possess most features of the matrices for one cylinder:

- All non-diagonal matrix elements tend to zero apart from restricted areas in the centre of each quadrant.

- The diagonal elements tend to unity.

- The size of the matrix where its elements are not zeroes grows with frequency.

- The size of the matrix is bigger at critical frequencies of the waveguide modes.

- At resonance frequencies of the scattering cylinder, one of the diagonal elements is small compared to unity.

The pictures of matrices in the case of scattering by two cylinders reveal an important characteristic of the Multi-Modal Integral Method. Namely, the convergence of the matrix elements remains intact after a cylinder is added near the first cylinder. The solution, which is obtained, is fully self-consistent and properly describes the acoustic interaction between the cylinders. This fact provides an opportunity to use the Multi-Modal Integral Method for modelling complex structures. For example, ten scatterers can be combined in the same manner like has been shown here for two scatterers.
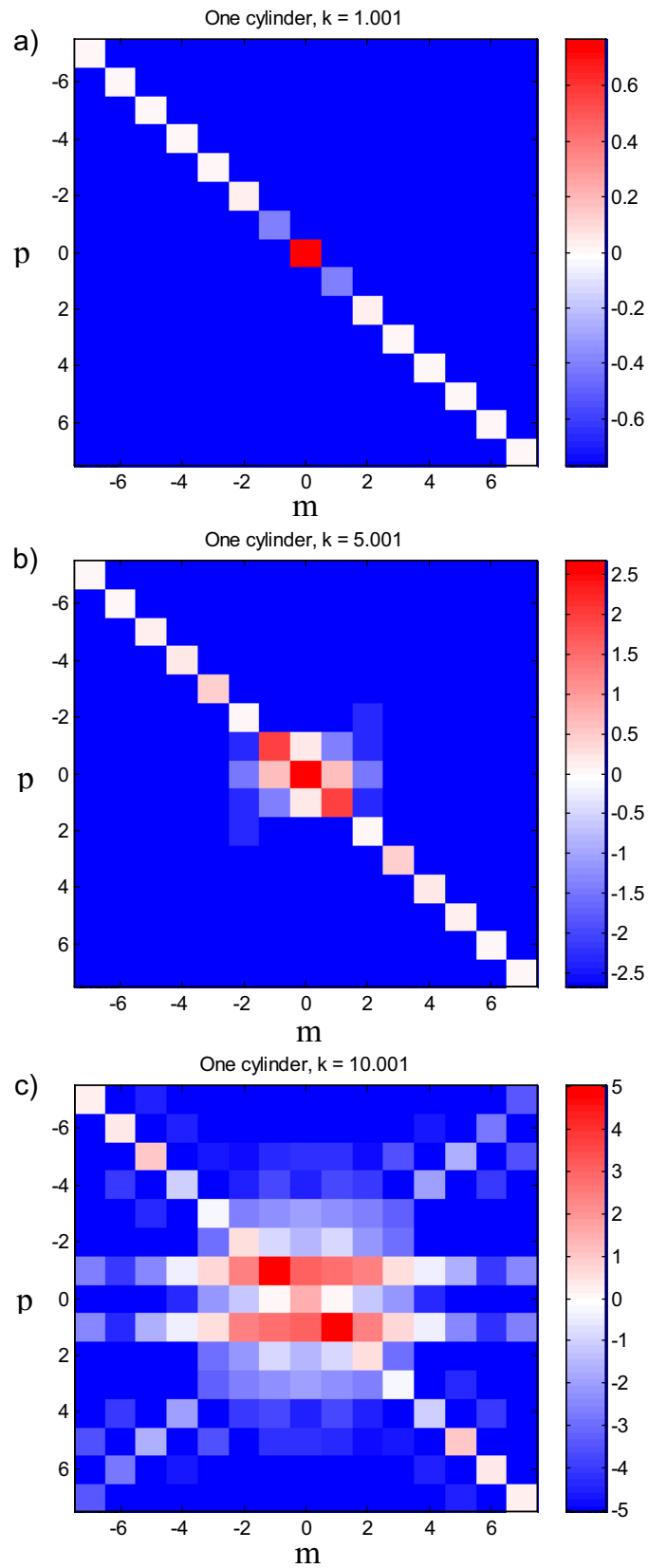
Figure 44. Scattering matrices for one homogeneous cylinder in the middle of the waveguide.

Figure 45. Scattering matrices for one homogeneous cylinder in the middle of the waveguide. Frequencies coincide with critical frequencies of the waveguide.

a)

One cylinder, k = 5.301

b)

One cylinder, k = 8.101

c)

One cylinder, k = 10.201

Figure 46. Scattering matrices for one homogeneous cylinder in the middle of the waveguide. Frequencies coincide with resonance frequencies.

Figure 47. Scattering matrices for two homogeneous cylinders in the middle of the waveguide.

a)

b)

c)

Figure 48. Scattering matrices for two homogeneous cylinders in the middle of the waveguide. Frequencies coincide with critical frequencies of the waveguide.

a)

Two cylinders, k = 4.001

b)

Two cylinders, k = 8.101

c)

Two cylinders, k = 10.201

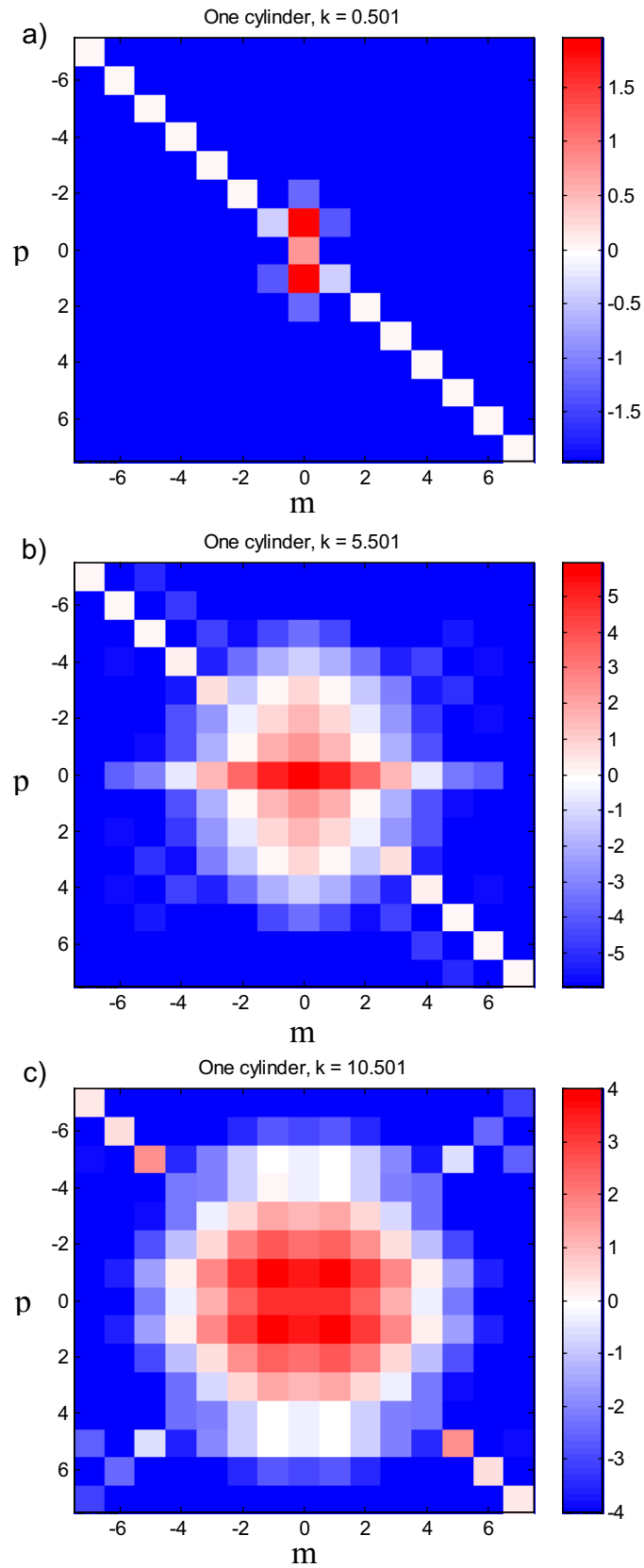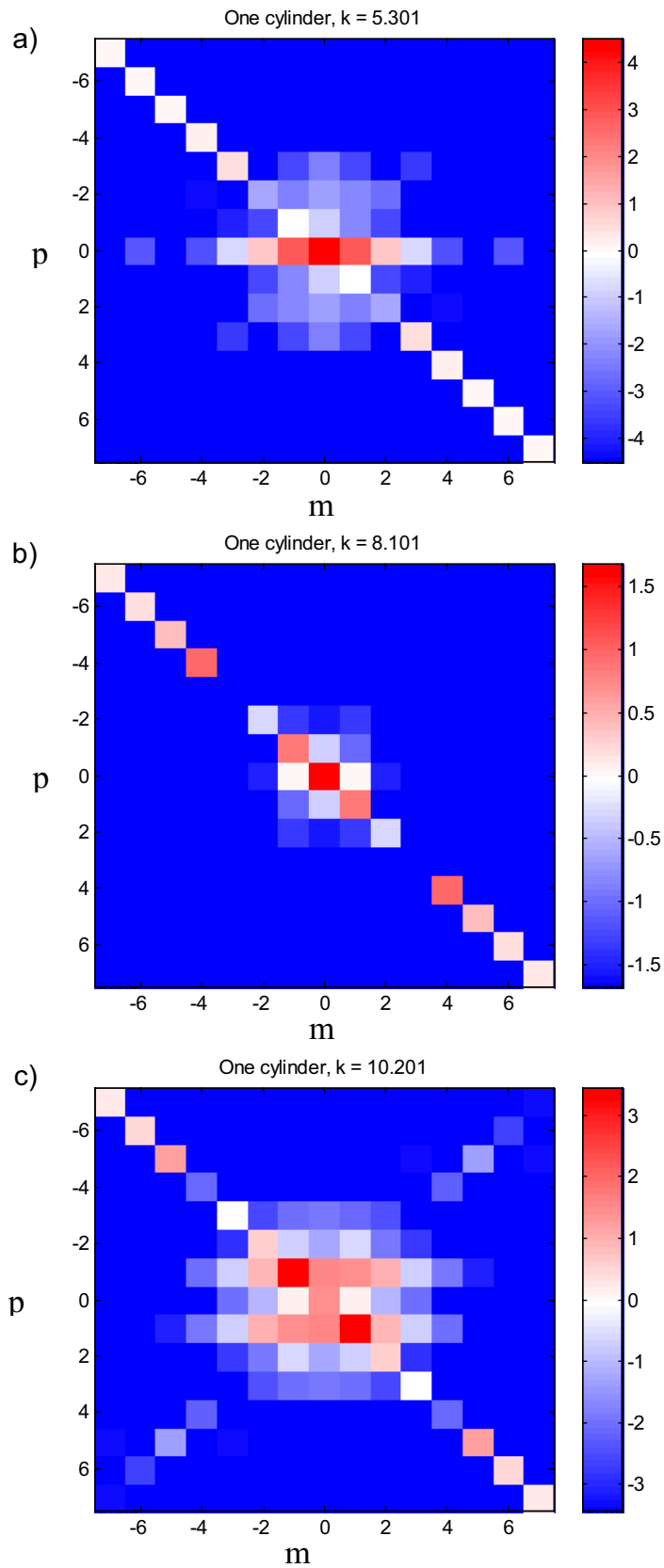*Figure 49. Scattering matrices for two homogeneous cylinders in the middle of the waveguide. Frequencies coincide with resonance frequencies.*
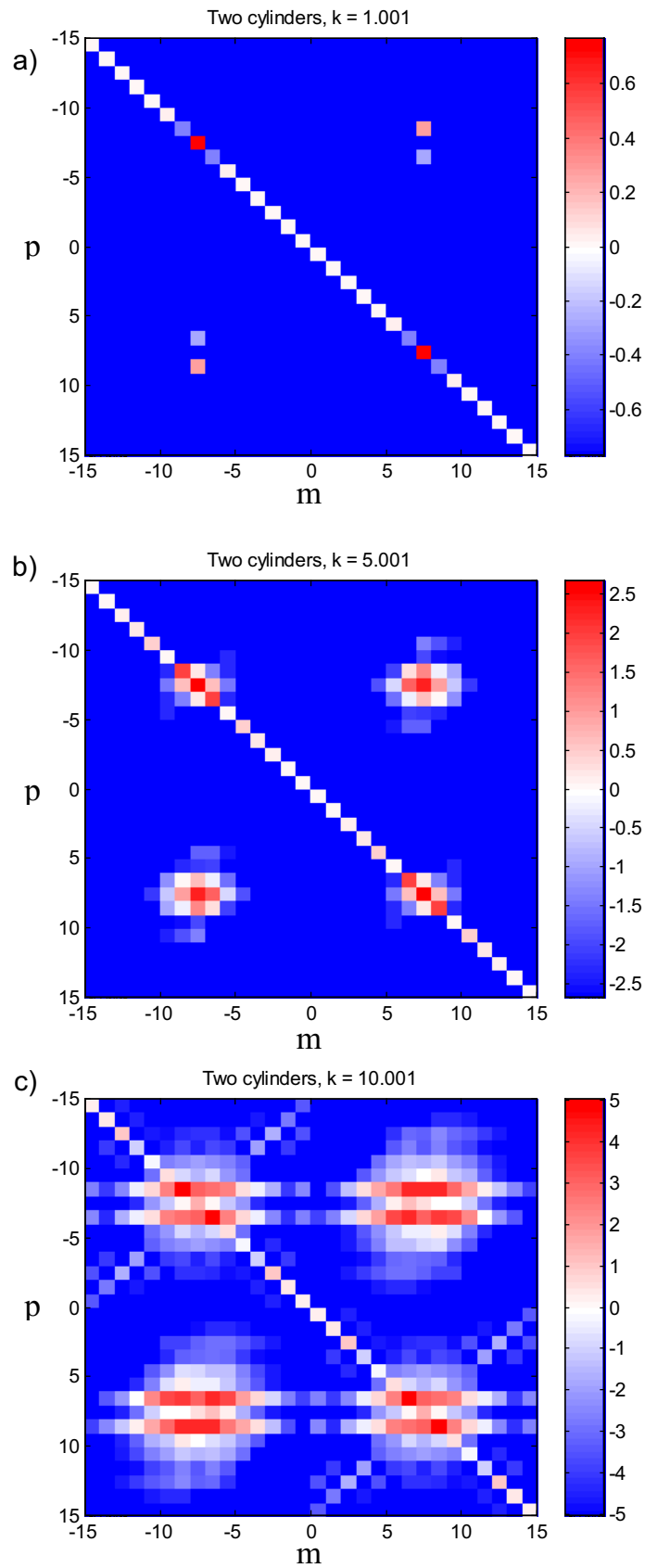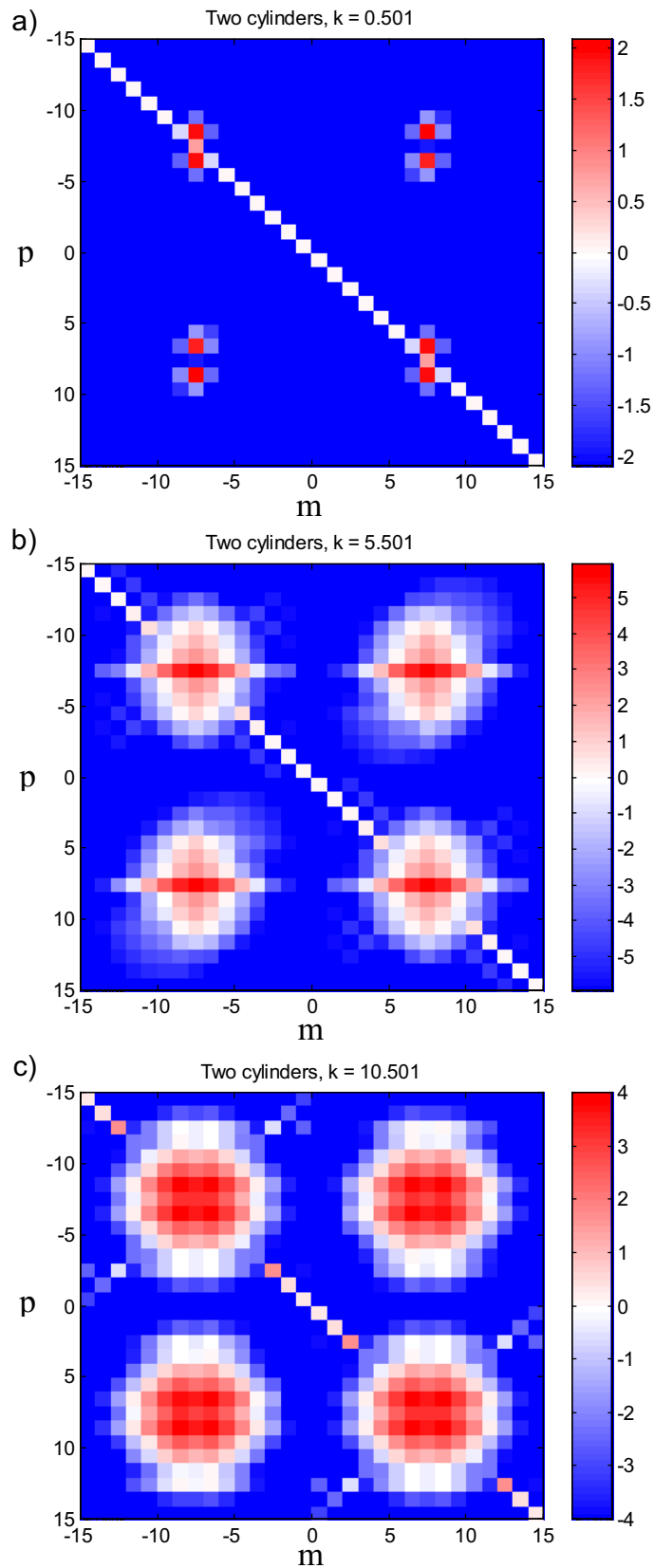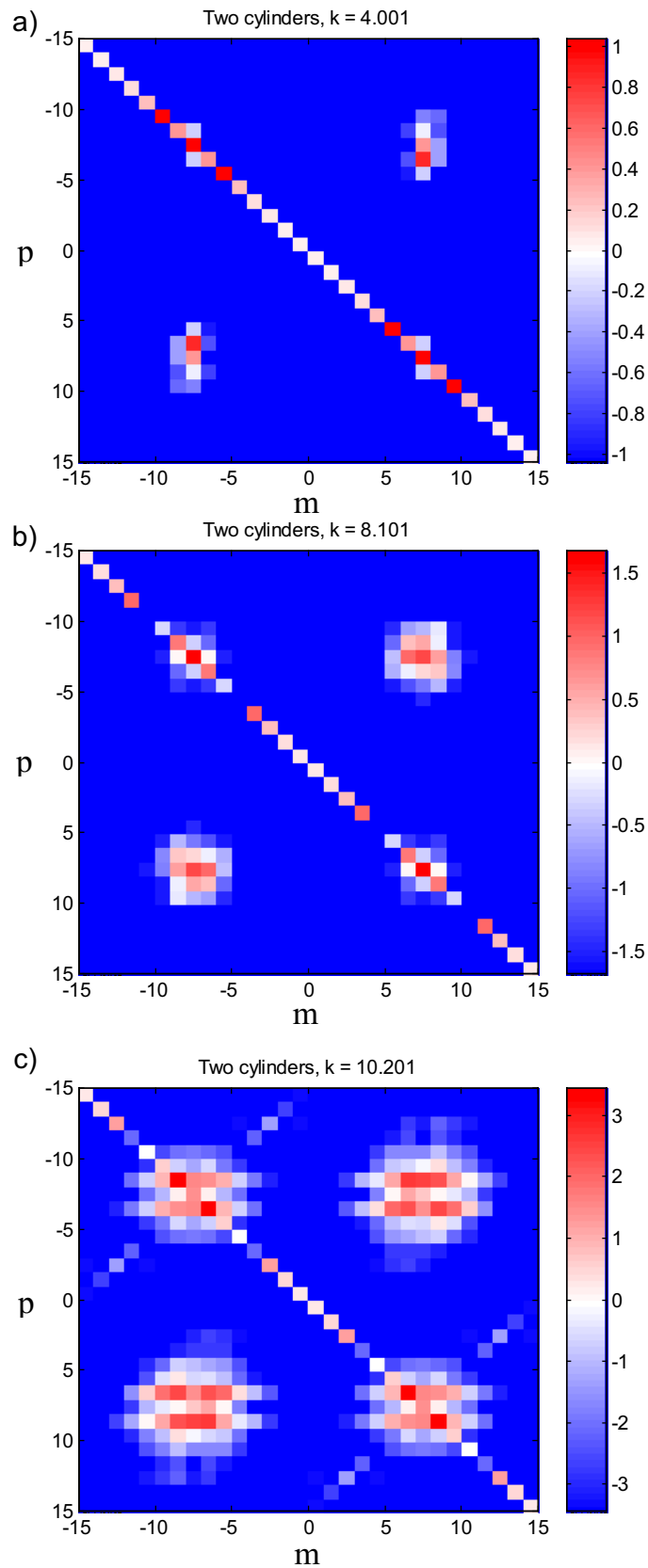
14.2.3.2 Scattering Matrices for an Air-Filled Elastic Shell.

Figures 50 - 52 show matrices for the case of an elastic shell as the scattering object for three values of the shell thickness considered in this work. Every figure contains three matrices for different values of the non-dimensional wavenumber (frequency) k. All the parameters used in the calculations are shown in Section 11.3.

14.2.3.2.1.Matrices for a Shell with Zero Thickness.

Pictures in Fig. 50 show matrices for the case of the zero thickness shell. The pictures show that the matrices for the shell also possess the two main features, which make them suitable for solving the scattering problem. Namely, their non-diagonal elements tend to zero, and the diagonal elements tend to unity apart from the restricted area, located in the centre of the matrix. This fact cosnfirms again the efficiency of the Multi-Modal Integral Method, which can be used with different types of scattering objects.

However, the matrices in Fig. 50 significantly differ from the matrices for homogeneous cylinders in two aspects. First, the size of the central area, where elements differ from zero, is larger. For example, the absolute value of the highest element m_{max} for the matrix in Fig. 50a is nine. In the case of homogeneous cylinders at the same frequency m_{max} is only four. Second, the maximum absolute value of the matrix elements for the shell is within the interval 10^{10} to 10^{15} at different frequencies, while for homogeneous cylinders the maximum of this value is 10^{5}.

Physically these features mean that the interaction, which occurs between different modes in the incident and scattered fields, is more intense in the case of a zero thickness shell. Indeed, the shell is filled with air, where the sound speed is much smaller than in the surrounding fluid. Consequently, many more internal modes exist at the same frequency within an air-filled shell, than within a homogeneous metal cylinder.

Figs. 50b,c show matrices for frequencies $k = 15.801$ and $k = 25.201$. As shown in Section 11.4, these frequencies correspond to the resonances of the shell. As Fig. 12a shows, these resonances correspond to the monopole and the dipole distributions of the velocity amplitude on the shell surface respectively. At these frequencies, the shell is more transparent for the incoming sound wave: the reflection coefficient has sharp minima (see Fig. 12b).

Analysis of the matrices, shown in Figs. 50b,c, reveals a major difference between these matrices and the resonance matrices for homogeneous cylinders (Figs. 46, 49). The matrices in Figs. 50b,c do not have a diagonal element with a very low absolute value. This fact means that no single cylindrical mode is dominant in the scattered field, and the resonances are complex motions of the shell consisting of many modes excited within the shell.

Thus, the matrices for the shell with zero thickness are of larger size and have elements of larger value than in the case of homogeneous cylinders. However, this fact does not affect significantly the efficiency of the Multi-Modal Integral Method.

14.2.3.2.2 *Matrices for a Shell with Non-Zero Thickness.*

Figs. 51, 52 show scattering matrices for shells with non-zero thickness $d = 0.05R_1$, where R_1 is the external radius of the shell. Fig. 51 corresponds to the shell located in the middle of the waveguide, while Fig. 52 corresponds to the shell located near the rigid waveguide bottom.

These matrices have the size and the value of elements similar to the size and the value of elements observed for homogeneous cylinders. This is expected when the influence of the shell wall is taken into account. Indeed, the shell wall shields the interior of the shell from the incident acoustic wave, and the excitation of the multimode oscillations within the shell is no longer efficient.

The influence of the shell wall explains also another feature of the matrices in Figs. 51, 52. It is seen in these pictures, that every matrix contains a row of elements, which are significantly different from zero. (These elements still tend to zero when the absolute value of their index increases, so this does not affect the convergence of the solution.) This fact may be explained in the following way. The wall of the shell is a thin elastic plate, where Lamb waves can propagate, as discussed in the literature review. At every frequency one of the Lamb modes is close to its resonance, and, consequently, has bigger amplitude than the other modes. Thus, the shell wall becomes more transparent for this particular component of the incident field, which leads to multimodal oscillations in the air-filled shell interior. The oscillations within the shell interior reveal themselves as a row of matrix elements significantly different from zero.

Generally, Figs. 51, 52 show, that the Multi-Modal Integral Method in the case of a non-zero thickness shell is as efficient as it is in the case of the homogeneous cylinders.

*Figure 50. Scattering matrices for an air-filled shell. Shell thickness d = 0, height of the shell above the bottom H =0.5*D.*

Figure 51. Scattering matrices for an air-filled shell. Shell thickness d = 0.05 * R_1, height of the shell above the bottom H =0.5*D.

a)

Shell, d = 0.05*R, H = 0.1*D, k = 5.001

b)

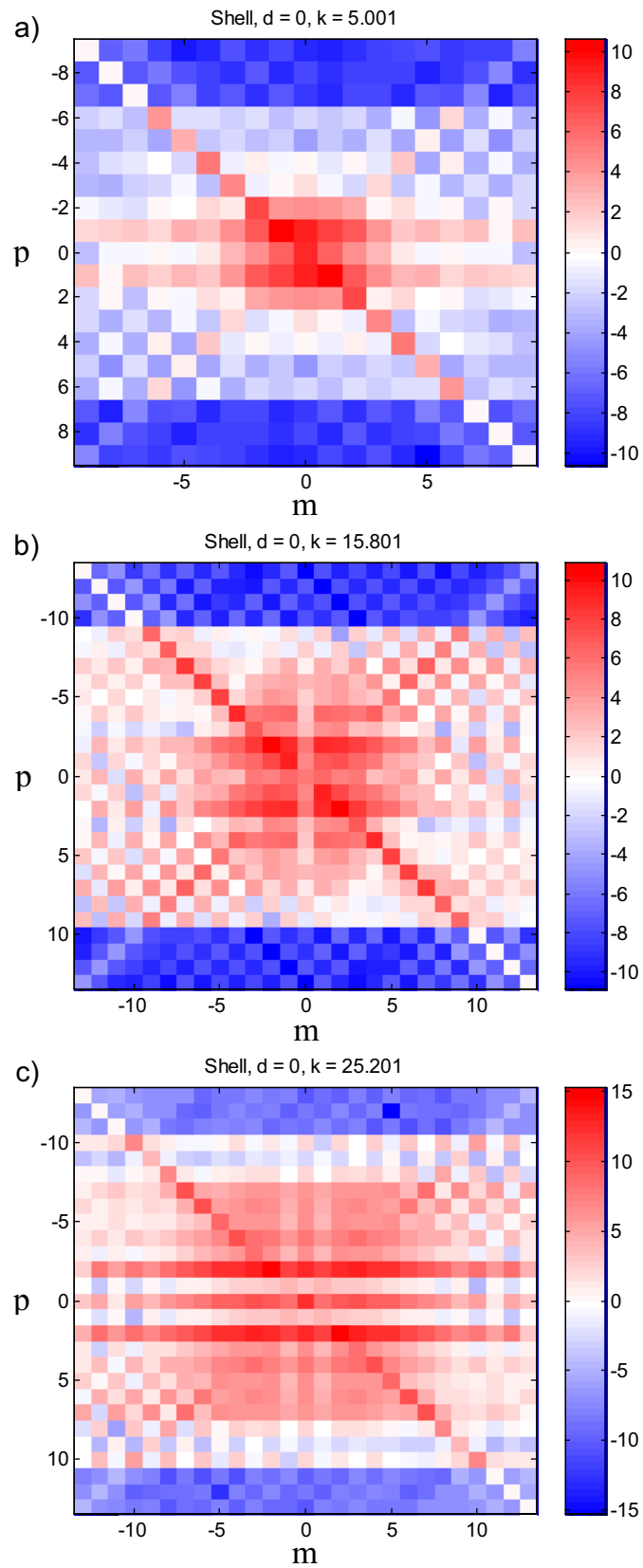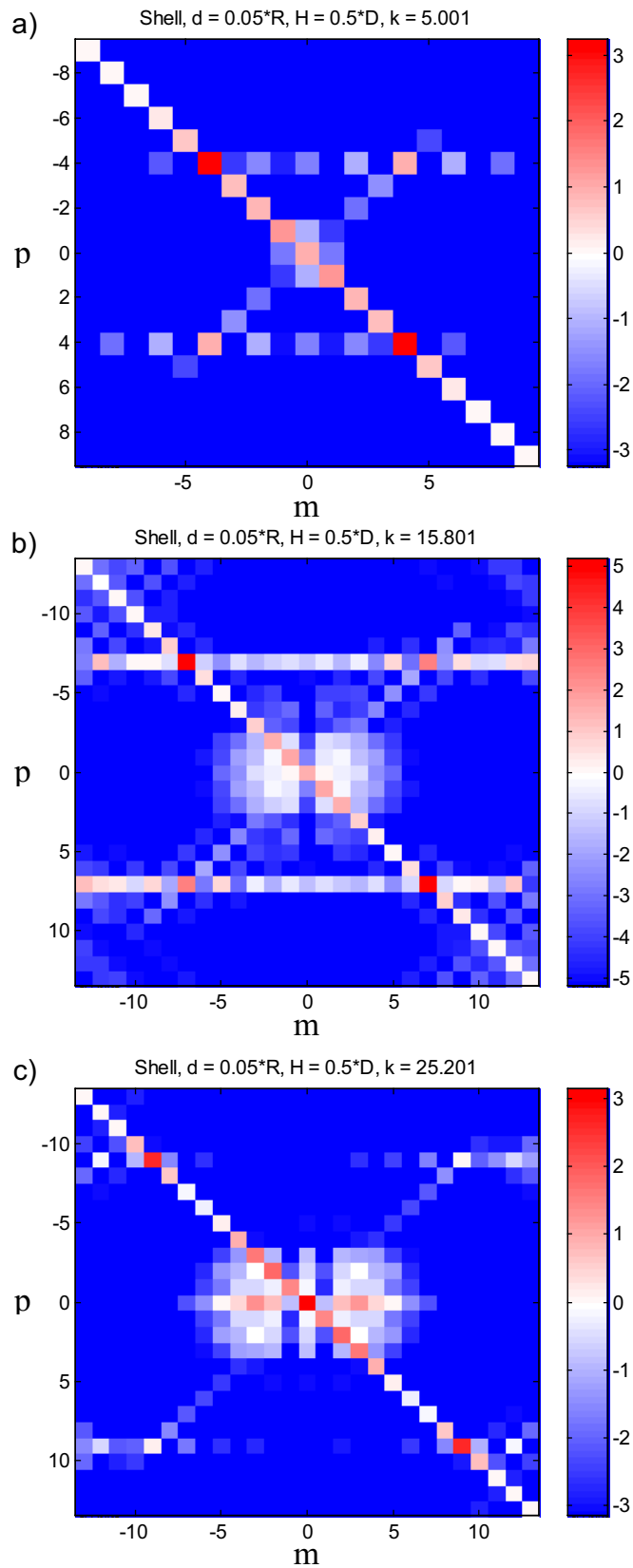Shell, d = 0.05*R, H = 0.1*D, k = 15.801
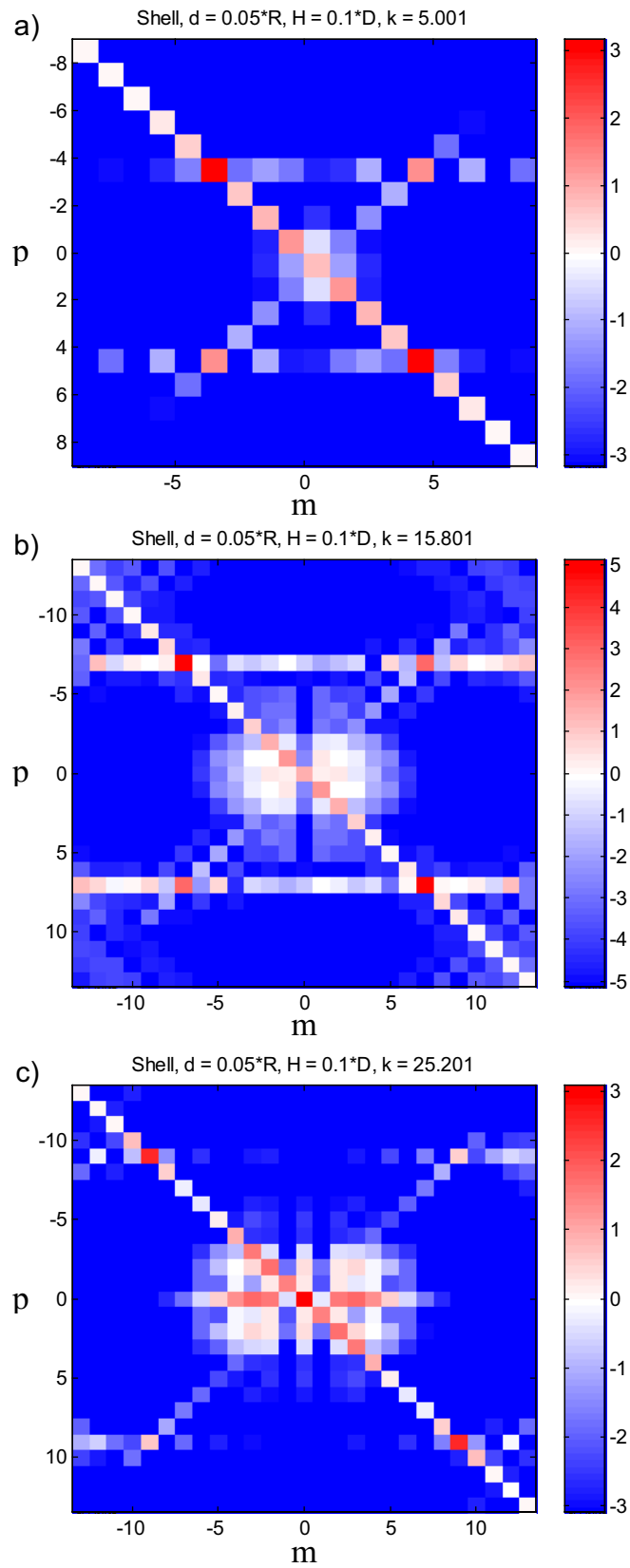
c)

Shell, d = 0.05*R, H = 0.1*D, k = 25.201

*Figure 52. Scattering matrices for an air-filled shell. Shell thickness d = 0.05 * R_1, height of the shell above the bottom H =0.1*D.*

14.2.4 Balance of Power Flows in the Waveguide.

The appearance of the scattering matrix shows clearly the efficiency of the Multi-Modal Integral Method in general. However, the size of the matrices can not be used as an indicator of a correct solution at every frequency. Calculation of discrepancy of power flows is used to control the accuracy of the solution.

14.2.4.1 Definition of Power Flow Discrepancy.

The waveguide, considered in this work, does not contain any acoustic sources near scattering objects. Consequently, power flows through the cross-sections on both sides of the scattering objects must be equal. In other words, the following condition must be satisfied:

$$\Delta I = \frac{S_e - S^-}{S^+} = 1 \,, \tag{87}$$

where S_e, S^-, and S^+ are the power flows in the incident, reflected and transmitted waves respectively. These values can be expressed through the modal coefficients of the incident and scattered acoustic waves. The corresponding expressions are shown in Appendix C.

Satisfaction of Eq. 87 can not guarantee the correctness and the accuracy of the solution. However, a difference ΔI from unity undoubtedly would be a proof that the obtained solution is incorrect. For this reason, the value of ΔI was monitored carefully for every set of waveguide parameters at every frequency point.

14.2.4.2 Power Flow Discrepancy for Homogeneous Cylinders.

Fig. 53 shows the frequency dependence of the power flow discrepancy for the case of a) one and b) two homogeneous cylinders in the middle of the waveguide. Blue and red lines correspond to different numbers of integration points taken into account in the calculation of the matrix elements (see the figure caption).

As shown above, the elements of the scattering matrix are determined by the double integral on the interval $[0, \pi]$ (see Eq. (63)). The calculations for homogeneous cylinders were carried out with only 10 integration points on the interval $[0, \pi]$. The integral was evaluated by means of a 10-point Gauss quadrature formula. The formula integrates polynomials up to degree 19 exactly, and it shows much better accuracy in comparison with other algorithms of numerical integration. The corresponding power flow discrepancy is shown in Fig. 53 by the blue lines.

As seen from the figure, the power flow discrepancy ΔI remains small at all frequencies. This fact again confirms the accuracy of the solution obtained with the use of the Multi-Modal Integral Method. However, at several frequencies ΔI experiences sharp jumps. These

jumps do not destroy the validity of the solution at these frequencies, but their explanation is required.

The reason for the jumps in the power flow discrepancy at some frequencies can be understood from the fact, that these frequencies are in fact the resonance frequencies, identified in Section 9.6. As was shown in Section 14.2.3.1, at these frequencies the value of one of the diagonal matrix elements is small, and better accuracy of numerical integration is needed to calculate the matrix elements.

Red lines in Fig. 53 show ΔI for the calculations, performed with 20 integration points on the interval $[0, \pi]$. It is seen from the figure, that the accuracy of calculations in this case is better at most frequencies. Moreover, the largest improvement is achieved at the resonance frequencies, where one of the diagonal elements has a small value. This fact shows that, if further improvement of the accuracy is needed, it can be achieved by increasing the number of integration points.

It can be concluded from Fig. 53, that the Multi-Modal Integral Method provides satisfactory accuracy even with a small number of integration points. If necessary, the accuracy may easily be improved by performing the numerical integration with a larger number of integration points. It can be seen also that the accuracy of the Multi-Modal Integral Method is the same for one and two cylinders.
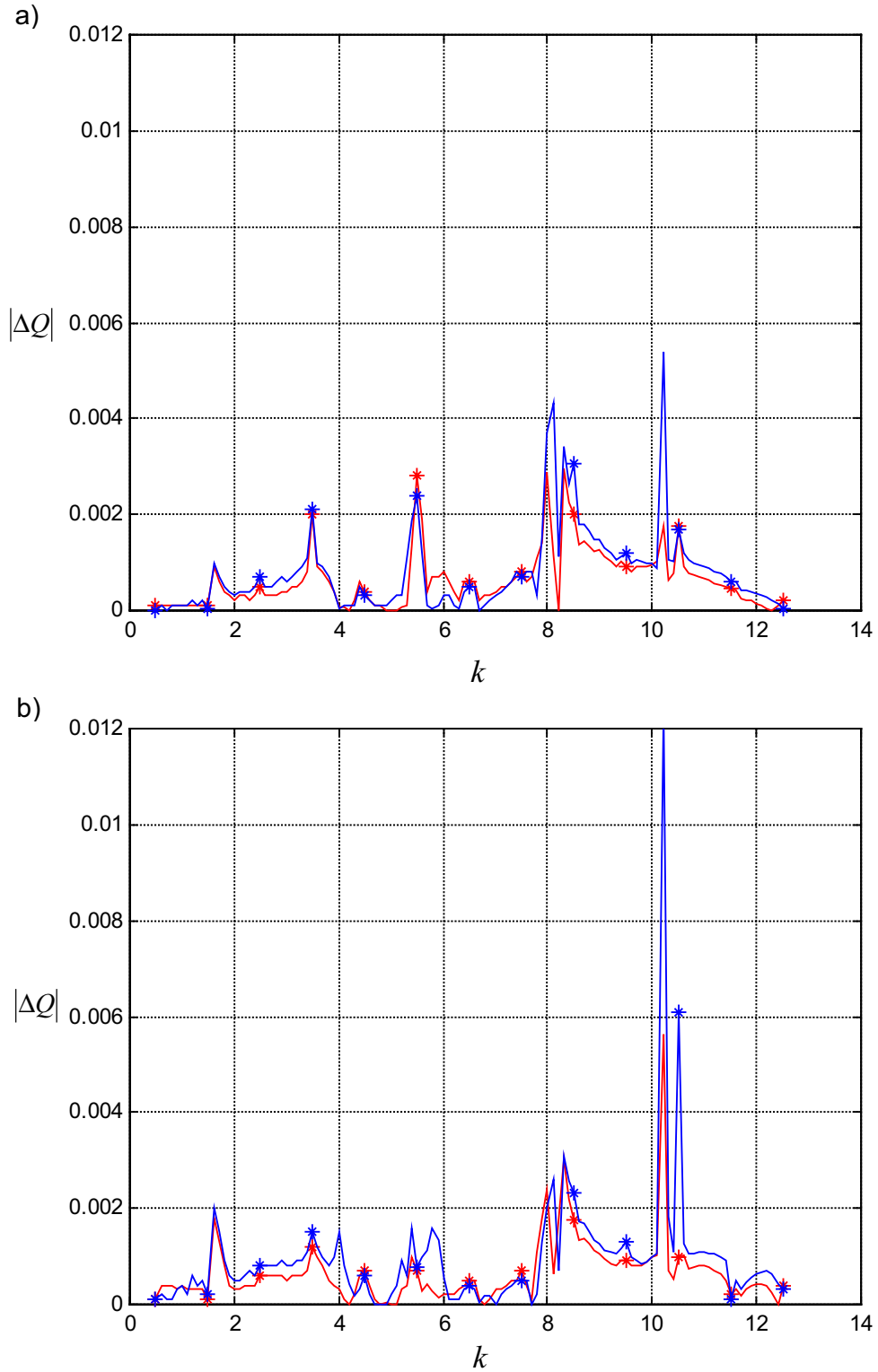
Figure 53. Power flow discrepancy vs non-dimensional frequency for a) one and b) two cylinders. Blue line:10 points on the interval of integration. Red line: 20 points on the interval of integration. Asterisks reveal critical frequencies of the waveguide.

14.2.4.3 Power Flow Discrepancy for an Air-Filled Shell.

The calculations for an air-filled shell were carried out using the following values of the maximum index of matrix elements m_{max} and the number of integration points N_{int}:

$$m_{max} = \begin{cases} 9, & k < 10 \\ 13, & k > 10 \end{cases}, \tag{88}$$

$$N_{int} = \begin{cases} 20, & k < 10 \\ 30, & k > 10 \end{cases}. \tag{89}$$

Fig. 54 shows the power flow discrepancy for three configurations of the waveguide with an air-filled shell as a scattering object. The figure reveals the following features.

First, the value of the discrepancy is well below 0.01 within the whole frequency range considered. This confirms the validity of the Multi-Modal Integral Method in the case of the shell as a scattering object.

Second, the discrepancy increases with frequency. As shown above, the size of the scattering matrix is larger at higher frequencies. Consequently, for accuracy to be maintained, the size of the matrix used in the calculations must also grow with frequency.

Third, the discrepancy curve experiences jumps (up or down) at the critical frequencies of the waveguide modes. This also is due to the larger size of the matrix at such frequencies, as was shown in Section 14.2.3.

In general, the power flow discrepancy for an air-filled shell remains satisfactory within the whole frequency range for the different waveguide configurations. The more complex structure of the shell in comparison with homogeneous cylinders requires a matrix of larger size and more integration points. However, these parameters remain small and may be easily increased if improvement of accuracy is required.

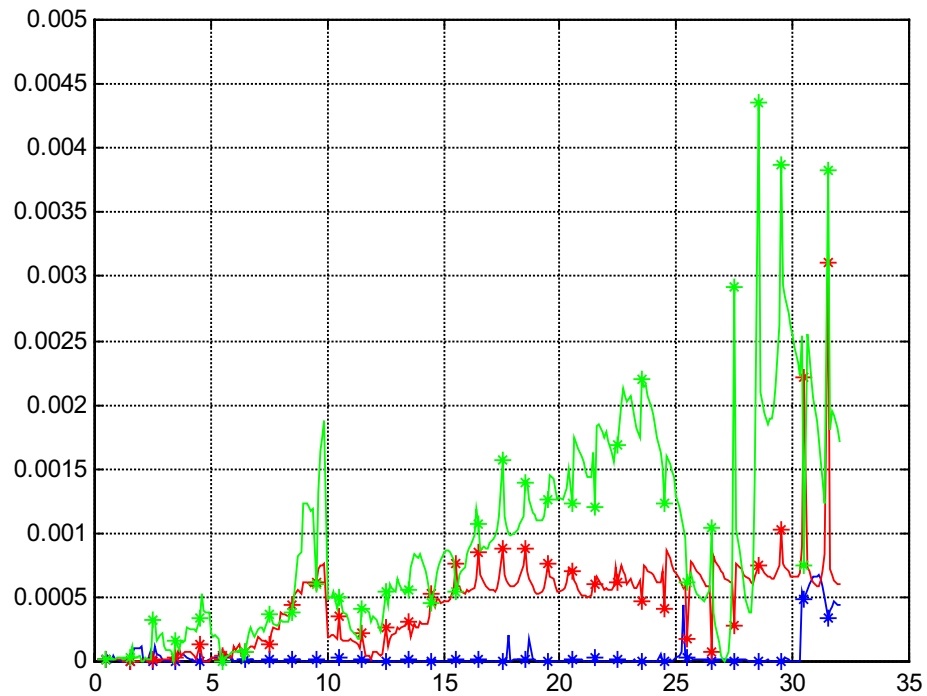*Figure 54. Power flow discrepancy vs non-dimensional frequency for an air-filled shell of external radius $R_1 = 0.05 * D$, where D is the waveguide depth. Blue line: shell thickness d = 0, the distance between the shell centre and the bottom H = 0.5 * D. Red line: d = 0.05 * R_1, H = 0.5 * D. Green line: d = 0.05 * R_1 , H = 0.1 * D. Asterisks reveal critical frequencies of the waveguide.*

14.3   Conclusions.

The accuracy of the solution in the current work is controlled by two methods. The first method is the proper truncation of the scattering matrix, and the second method is monitoring the discrepancy of power flows in the incident and scattered waves.

The Multi-Modal Integral Method, developed in this work, uses a modified form of the Green's function of the waveguide. The scattering matrices, calculated with the use of the modified Green's function, can easily be truncated without losing information about the system. All non-diagonal elements of the matrices tend to zero apart from a restricted area in the central part of the matrices. The diagonal elements in the matrices tend to unity, which prevents the linear equations from being singular.

The examples of scattering matrices for different waveguide configurations show, that the convenient appearance of the matrices remains in the cases of one cylinder, two cylinders, and an air-filled elastic shell. The maximum index of the matrix elements in the numerical experiments varied from 4 to 13, which demonstrates the effectiveness of the Multi-Modal Integral Method for different configurations.

Investigation of the scattering matrices provides a technique for finding resonance frequencies of a scattering object. At such frequencies, a diagonal element related to the resonant mode is small compared to unity.

To control the accuracy of the solution, the power flow balance in the scattered and incident waves is used. In all the configurations and the frequency ranges, considered in this work, the discrepancy in the power flow remains below 0.01. If improvement in accuracy is needed, it can easily be achieved by increasing the size of the scattering matrix or by increasing the number of integration points.

Generally, the convenient appearance of the scattering matrix is a major advantage of the Multi-Modal Integral Method. Control of the power flow imbalance proves that an accurate solution of the scattering problem can be obtained with the use of only a small number of rows and columns in the scattering matrix.

15 Summary.

From the papers, which have been reviewed, it is clear that much research has been done in the area of sound scattering by elastic objects. However, there is a lack of results for scattering in shallow waveguides, which is due to the mathematical complexity of the problem where the influence of the waveguide walls must be taken into account.

In this paper, a method has been presented for solving wave diffraction problems by employing a system of N space-localised inhomogeneities in a longitudinally homogeneous waveguide. The waveguide boundaries may be of arbitrary reactive impedance. The method combines integral equations and eigenfunction methods to reduce the problem to a system of $2N$ integral-functional equations relative to the fields excited in elastic bodies and sources of scattered waves on the surface of cylinders. The method also employs a Green's function of the waveguide in a non-standard form so that it is a quickly converging series allowing taking into consideration all waveguide modes up to the infinite order.

The method was applied to scattering by a set of homogeneous cylinders. Amplitude-frequency and phase-frequency characteristics are obtained for the absolute values of mode components of the scattered field. Results show that the modal coefficients experience abrupt changes near resonance frequencies of the cylinder and the waveguide. It was also shown that the coefficients of evanescent modes are not even approximately zero, which demonstrates the important part they play in the scattering process. It was shown that the resonances of the waveguide and the scattering object are determined by the maxima and minima in the amplitude-frequency characteristics of the modal amplitudes.

The spatial distribution of the pressure amplitude is obtained in the waveguide near the scattering cylinders for two versions of the system: a) one cylinder in the middle of the waveguide, and b) two cylinders in the middle of the waveguide, one of which is located behind the other. The results show high-amplitude oscillations in the near vicinity of the cylinders in the case of resonance frequency excitation, while the far field structure is changed significantly at resonance. This again demonstrates the important role of non-propagating evanescent modes. The mechanism responsible for the scattering by two cylinders at resonance has also been described.

Frequency and angular dependencies of the acoustic source density distribution on the cylinder surface are obtained for both versions a) and b) of the system. A series of resonances with different spatial structures have been identified within the considered frequency range. It is shown that the resonances are associated with structural resonances of the shell as well as with surface elastic waves near the cylinder boundary. It is also demonstrated that the resonances correspond to maxima and minima in the amplitude-frequency

characteristics. A resonance split is revealed for one and two cylinders.

Energy streamlines are calculated for one cylinder in a waveguide with both boundaries as pressure release surfaces. Calculations are carried out for two sets of elastic parameters of the cylinder, corresponding to "soft" and "rigid" objects. It is shown that at low frequencies the energy streamlines are significantly distorted near the cylinder in both cases, which corresponds to motion of the object back and forth in the acoustic field. Closed energy streamlines, the energy vortices, are identified both in the near and far field zones. It was shown, that in the case of the "soft" cylinder, at the frequency near one of its internal resonances, the near field energy vortices go through the interior of the cylinder. This fact is explained by high-amplitude internal oscillations of the cylinder, which cause the excitation of higher-order waveguide modes. These modes interfere with each other causing the appearance of the near field energy vortices. It was shown that the near field energy vortices form a single scattering object with the cylinder itself resulting in a much bigger scattering cross-section. It was also suggested that reradiation of the acoustic energy stored in the vortices may contribute to the echo phenomenon.

The method also was applied to scattering by an air-filled elastic cylindrical shell. The frequency dependencies of the reflection coefficient were compared with the distribution of the velocity amplitude on the surface of a shell. The analysis showed that resonances in the shell oscillations strongly affect the amount of energy reflected from the shell. Different kinds of resonances were revealed for different values of the frequency, the shell thickness, and the distance between the shell and the bottom.

The sharp decrease of the reflected signal, found at some frequencies, suggests, that the reflection from an elastic object can be suppressed in two possible ways. The first way is to select the corresponding internal structure of the object, and the second way is to actively excite oscillations, which may increase sound transmission through the object, thus decreasing the reflection. It was also shown that the conventional definition of target strength is inappropriate in a shallow waveguide.

Two techniques were used to control the accuracy of the solution. The first was the correct truncation of the scattering matrix, and the second was the monitoring of the power flow balance in the incident and the scattered waves. The scattering matrices, calculated using the modified Green's function, have a convenient form, which can be easily truncated. In all situations considered the correctness of the truncation was verified by an acceptable power flow discrepancy.

In conclusion, the Multi-Modal Integral Method, suggested and used in this work, is an efficient and powerful tool for solving scattering problems in waveguides. The method differs from other available methods by providing mathematically exact solutions. The numerical

implementation of the method requires few computer resources for good accuracy of the solution. The current work also suggests that similar techniques may be applied to other real-life scattering problems.

16 Appendix A. Derivation of the Modified Green's Function.

16.1 Common Form of Green's Function

The Green's function $G(x,y;x_0,y_0)$ of a medium is the field of a singular source located at the point (x_0, y_0) with the observation point at (x, y). The Green's function satisfies the non-uniform Helmholtz equation:

$$(\Delta + k^2)G(x,y;x_0,y_0) = \delta(x\text{-}x_0)\delta(y\text{-}y_0), \tag{A1}$$

where the delta-function, $\delta(x) = \begin{cases} \infty, x = 0 \\ 0, x \neq 0 \end{cases}, \quad \int_{-\infty}^{\infty} \delta(\xi)d\xi = 1$.

In the case of the waveguide with both boundaries pressure release, the Green's function satisfies the following boundary conditions on the waveguide walls:

$$G(x,0;x_0,y_0) = 0, \quad G(x,\pi;x_0,y_0) = 0. \tag{A2}$$

Remember that the normalisation used in this work assumes that all variables and parameters, that have the dimension of length, are normalised by D/π.

The solution of the boundary problem (A1) and (A2), can be obtained by standard methods. It takes the following form:

$$G(x, y; x_0, y_0) = \sum_{n=1}^{\infty} K_n(x, y; x_0, y_0), \tag{A3a}$$

$$K_n = \frac{i}{\pi g_n} \sin nx_0 \sin nx \exp(ig_n|y - y_0|), \tag{A3b}$$

$$g_n = \sqrt{k^2 - n^2}. \tag{A4}$$

Differentiation of the Green's function (A3a) over the direction $\vec{r}$, determined by the angle φ between $\vec{r}$ and the horizontal axis, gives the following expression for the derivative of the Green's function:

$$\frac{\partial G(x, y; x_0, y_0)}{\partial r} = \sum_{n=1}^{\infty} L_n(x, y; x_0, y_0), \tag{A5a}$$

$$L_n = \frac{1}{\pi} \sin nx_0 \left[\frac{in}{g_n} \sin \varphi \cos nx \mp \cos \varphi \sin nx \right] \exp(ig_n|y - y_0|). \tag{A5b}$$

The Green's function (A3) and its derivative (A5) converge very slowly, so it is necessary to improve their convergence by separating the asymptotic term.

16.2 Improving Convergence of the Green's Function

Observe that any function may be added and subtracted from the Green's function:

$$G = \sum_{n=1}^{\infty} K_n - \overline{K} + \overline{K} . \tag{A6}$$

A convenient function to add and subtract is defined by the following expressions:

$$\overline{K} = \sum_{n=1}^{\infty} \overline{K}_n , \quad \overline{K}_n = \lim_{n/k \to \infty} K_n . \tag{A7}$$

Taking into account, that at $n/k \to \infty$ $\dfrac{i}{g_n} \cong \dfrac{1}{n}$, and $ig_n \cong -n$, it is possible to obtain the expression for $\overline{K}_n$:

$$\overline{K}_n = \lim_{n/k \to \infty} K_n = \lim_{n/k \to \infty} \left(\frac{i}{\pi g_n} \sin nx_0 \sin nx \exp(ig_n |y - y_0|) \right), \tag{A8a}$$

$$\overline{K}_n = \frac{1}{\pi n} \sin nx \sin nx_0 \exp[-n|y - y_0|]. \tag{A8b}$$

Using the well-known trigonometric formula:

$$\sin \alpha \sin \beta = \tfrac{1}{2}[\cos(\alpha - \beta) - \cos(\alpha + \beta)], \tag{A9}$$

the function $\overline{K}_n$ can be represented in the following form:

$$\overline{K}_n = \frac{1}{2\pi n} [\cos n(x - x_0) - \cos n(x + x_0)] \exp[-n|y - y_0|]. \tag{A10}$$

The sum of the series (A7) can be calculated by means of the formula(Prudnikov, 1986):

$$\sum_{n=1}^{\infty} \frac{r^n}{n} \cos nx = -\tfrac{1}{2} \ln(1 - 2r \cos x + r^2). \tag{A11}$$

It may be observed that the formula (A11) takes the form of (A10), when the following substitutions are made:

$$r = \exp(-|y - y_0|), \quad x = x \pm x_0 . \tag{A12}$$

Now, an expression for $\overline{K}$ may be found:

$$\begin{aligned}
\overline{K} &= \sum_{n=1}^{\infty} \frac{1}{2\pi n} [\cos n(x - x_0) - \cos n(x + x_0)] \exp[-n|y - y_0|] \\
&= \sum_{n=1}^{\infty} \frac{1}{2\pi n} \cos n(x - x_0) e^{-n|y - y_0|} - \sum_{n=1}^{\infty} \frac{1}{2\pi n} \cos n(x + x_0) e^{-n|y - y_0|} \\
&= -\frac{1}{4\pi} \ln\left[1 - 2e^{-|y - y_0|} \cos(x - x_0) + e^{-2|y - y_0|}\right] \\
&\quad + \frac{1}{4\pi} \ln\left[1 - 2e^{-|y - y_0|} \cos(x + x_0) + e^{-2|y - y_0|}\right] \\
&= \frac{1}{4\pi} \ln \frac{1 - 2e^{-|y - y_0|} \cos(x + x_0) + e^{-2|y - y_0|}}{1 - 2e^{-|y - y_0|} \cos(x - x_0) + e^{-2|y - y_0|}}
\end{aligned} \tag{A13}$$

By dividing both the numerator and the denominator by $2\exp(-|y-y_0|)$, it is possible to obtain the final expression for $\overline{K}$:

$$\overline{K} = \frac{1}{4\pi}\ln\left[\frac{\cosh|y-y_0| - \cos(x+x_0)}{\cosh|y-y_0| - \cos(x-x_0)}\right]. \tag{A14}$$

Now, the waveguide Green's function $G(x,y;x_0,y_0)$ can be represented as

$$G(x,y;x_0,y_0) = \overline{K}(x,y;x_0,y_0) + \sum_{n=1}^{\infty}\left(K_n(x,y;x_0,y_0) - \overline{K}_n(x,y;x_0,y_0)\right), \tag{A15}$$

where the functions $\overline{K}$, K_n, and $\overline{K}_n$ are determined by (A14), (A3b), and (A8b).

It should be noted that the function $\overline{K}$ describes the influence of all evanescent waveguide modes up to infinite order, while the series describes the influence of the lower-order modes. Due to the correlations (A7), the series converges very quickly as soon as the mode order n becomes greater than the non-dimensional wavenumber k.

16.3   *Improving Convergence of the Green's Function Derivative.*

The techniques used for improving the convergence of the Green's function derivative are analogous to the techniques used above for improving the convergence of the Green's function in section 16.2. However, opposed to section 16.2, not one, but two asymptotic terms over the parameter k/n are taken into account.

Observe that any function may be added and subtracted from the Green's function derivative over the direction $\vec{r}$:

$$\frac{\partial G}{\partial r} = \sum_{n=1}^{\infty}L_n - \overline{L} + \overline{L} . \tag{A16}$$

In this case, a convenient function to add and subtract is defined by the following expressions:

$$\overline{L} = \sum_{n=1}^{\infty}\overline{L}_n, \quad \overline{L}_n = \lim_{n/k\to\infty}L_n . \tag{A17}$$

Taking into consideration, that at $n/k\to\infty$ $\dfrac{i}{g_n}\cong\dfrac{1}{n}$, and $ig_n\cong-n\left(1-\dfrac{1}{2}\left(\dfrac{k}{n}\right)^2\right)$,

an expression for $\overline{L}_n$ is obtained as follows:

$$\overline{L}_n = \lim_{n/k\to\infty}L_n$$
$$= \lim_{n/k\to\infty}\left[\frac{1}{\pi}\sin nx_0\left(\frac{in}{g_n}\sin\varphi\cos nx \mp \cos\varphi\sin nx\right)\exp\left(ig_n|y-y_0|\right)\right], \tag{A18a}$$

$$\overline{L}_n = \frac{1}{\pi}\sin nx_0\left(\cos nx\sin\varphi \mp \sin nx\cos\varphi\right)\left(1+\frac{k^2}{2n}|y-y_0|\right)e^{-n|y-y_0|}. \tag{A18b}$$

In contrast to the expression (A8b), the expression (A18b) takes into account the two first terms in the Tailor series of the exponent $\exp(ig_n|y - y_0|)$ over the parameter k/n. The additional term further improves the convergence of the series, which is important for the correct calculation of the Green's function derivative.

With the use of the following trigonometrical formulas:

$$\sin\alpha\sin\beta = \tfrac{1}{2}[\cos(\alpha - \beta) - \cos(\alpha + \beta)],\qquad\text{(A19a)}$$

$$\sin\alpha\cos\beta = \tfrac{1}{2}[\sin(\alpha - \beta) + \sin(\alpha + \beta)],\qquad\text{(A19b)}$$

the expression (A18b) can be written as:

$$\overline{L}_n = \frac{1}{2\pi}\{\sin\varphi[\sin n(x_0 - x) + \sin n(x_0 + x)]$$
$$\mp\cos\varphi[\cos n(x_0 - x) - \cos n(x_0 + x)]\}\times\left(1 + \frac{k^2}{2n}|y - y_0|\right)e^{-n|y-y_0|}.\qquad\text{(A20)}$$

Now the series (A17) for $\overline{L}$ may be written as a sum of several series, each of which will be calculated separately:

$$\overline{L} = \frac{1}{2\pi}(S_1 + S_2 \mp S_3 \pm S_4 + S_5 + S_6 \mp S_7 \pm S_8),\qquad\text{(A21)}$$

$$S_1 = \sin\varphi\sum_{n=1}^{\infty}\sin n(x_0 - x)e^{-n|y-y_0|},\qquad\text{(A22)}$$

$$S_2 = \sin\varphi\sum_{n=1}^{\infty}\sin n(x_0 + x)e^{-n|y-y_0|},\qquad\text{(A23)}$$

$$S_3 = \cos\varphi\sum_{n=1}^{\infty}\cos n(x_0 - x)e^{-n|y-y_0|},\qquad\text{(A24)}$$

$$S_4 = \cos\varphi\sum_{n=1}^{\infty}\cos n(x_0 + x)e^{-n|y-y_0|},\qquad\text{(A25)}$$

$$S_5 = \frac{k^2\sin\varphi}{2}|y - y_0|\sum_{n=1}^{\infty}\frac{1}{n}\sin n(x_0 - x)e^{-n|y-y_0|},\qquad\text{(A26)}$$

$$S_6 = \frac{k^2\sin\varphi}{2}|y - y_0|\sum_{n=1}^{\infty}\frac{1}{n}\sin n(x_0 + x)e^{-n|y-y_0|},\qquad\text{(A27)}$$

$$S_7 = \frac{k^2\cos\varphi}{2}|y - y_0|\sum_{n=1}^{\infty}\frac{1}{n}\cos n(x_0 - x)e^{-n|y-y_0|},\qquad\text{(A28)}$$

$$S_8 = \frac{k^2\cos\varphi}{2}|y - y_0|\sum_{n=1}^{\infty}\frac{1}{n}\cos n(x_0 + x)e^{-n|y-y_0|}.\qquad\text{(A29)}$$

The series S_1 and S_2 are calculated using the following formula (Prudnikov, 1986):

$$\sum_{n=1}^{\infty} (\pm 1)^n e^{-na} \sin nx = -\frac{1}{2} \frac{\sin x}{\cos x \mp \cosh a} \; .$$
(A30)

Taking into account that $|y - y_0|$ corresponds to a in (A30), one can conclude that

$$S_1 = \sin \varphi \sum_{n=1}^{\infty} \sin n(x_0 - x) e^{-n|y-y_0|} = -\frac{1}{2} \frac{\sin \varphi \sin(x_0 - x)}{\cos(x_0 - x) - \cosh|y - y_0|},$$
(A31)

$$S_1 = \sin \varphi \sum_{n=1}^{\infty} \sin n(x_0 + x) e^{-n|y-y_0|} = -\frac{1}{2} \frac{\sin \varphi \sin(x_0 + x)}{\cos(x_0 + x) - \cosh|y - y_0|}.$$
(A32)

To find the sum of the series S_3 and S_4, the following formula is used (Prudnikov, 1986):

$$\sum_{n=1}^{\infty} (\pm 1)^n e^{-na} \cos nx = \frac{1}{2} \frac{\sinh a}{\cosh a \mp \cos x} - \frac{1}{2}.$$
(A33)

The series S_3 and S_4 can be represented as:

$$S_3 = \cos \varphi \sum_{n=1}^{\infty} \cos n(x_0 - x) e^{-n|y-y_0|} = \frac{\cos \varphi}{2} \left[\frac{\sinh|y - y_0|}{\cosh|y - y_0| - \cos(x_0 - x)} - 1 \right]$$
$$= \frac{\cos \varphi}{2} \left[\frac{-e^{-|y-y_0|} + \cos(x_0 - x)}{\cosh|y - y_0| - \cos(x_0 - x)} \right],$$
(A34)

$$S_4 = \cos \varphi \sum_{n=1}^{\infty} \cos n(x_0 + x) e^{-n|y-y_0|} = \frac{\cos \varphi}{2} \left[\frac{\sinh|y - y_0|}{\cosh|y - y_0| - \cos(x_0 + x)} - 1 \right]$$
$$= \frac{\cos \varphi}{2} \left[\frac{-e^{-|y-y_0|} + \cos(x_0 + x)}{\cosh|y - y_0| - \cos(x_0 + x)} \right].$$
(A35)

To find S_5 and S_6, the following formula is needed (Prudnikov, 1986):

$$\sum_{n=1}^{\infty} \frac{r^n}{n} \sin nx = \arctan \frac{r \sin x}{1 - r \cos x} \; .$$
(A36)

Taking into account that $e^{-|y-y_0|}$ corresponds to r in (A36), the series S_5 and S_6 can be found as:

$$S_5 = \frac{k^2 \sin \varphi}{2} |y - y_0| \sum_{n=1}^{\infty} \frac{1}{n} \sin n(x_0 - x) e^{-n|y-y_0|}$$
$$= \frac{k^2 \sin \varphi}{2} |y - y_0| \arctan \frac{e^{-|y-y_0|} \sin(x_0 - x)}{1 - e^{-|y-y_0|} \cos(x_0 - x)},$$
(A37)

$$S_6 = \frac{k^2 \sin \varphi}{2} |y - y_0| \sum_{n=1}^{\infty} \frac{1}{n} \sin n(x_0 + x) e^{-n|y-y_0|}$$
$$= \frac{k^2 \sin \varphi}{2} |y - y_0| \arctan \frac{e^{-|y-y_0|} \sin(x_0 + x)}{1 - e^{-|y-y_0|} \cos(x_0 + x)}.$$
(A38)

With the use of the formula (A11), the series S_7 and S_8 can be written in the following form:

$$
\begin{aligned}
S_7 &= \frac{k^2 \cos\varphi}{2}|y-y_0|\sum_{n=1}^{\infty}\frac{1}{n}\cos n(x_0-x)e^{-n|y-y_0|} \\
&= \frac{k^2 \cos\varphi}{2}|y-y_0|\left(-\frac{1}{2}\right)\ln\left[1-2e^{-|y-y_0|}\cos(x_0-x)+e^{-2|y-y_0|}\right],
\end{aligned}
\tag{A39}
$$

$$
\begin{aligned}
S_8 &= \frac{k^2 \cos\varphi}{2}|y-y_0|\sum_{n=1}^{\infty}\frac{1}{n}\cos n(x_0+x)e^{-n|y-y_0|} \\
&= \frac{k^2 \cos\varphi}{2}|y-y_0|\left(-\frac{1}{2}\right)\ln\left[1-2e^{-|y-y_0|}\cos(x_0+x)+e^{-2|y-y_0|}\right].
\end{aligned}
\tag{A40}
$$

The difference $S_7 - S_8$ can be further simplified:

$$
\begin{aligned}
S_7 - S_8 &= \frac{k^2 \cos\varphi}{4}|y-y_0|\ln\frac{1-2e^{-|y-y_0|}\cos(x_0+x)+e^{-2|y-y_0|}}{1-2e^{-|y-y_0|}\cos(x_0-x)+e^{-2|y-y_0|}} \\
&= \frac{k^2 \cos\varphi}{4}|y-y_0|\ln\frac{\cosh|y-y_0|-\cos(x_0+x)}{\cosh|y-y_0|-\cos(x_0-x)}.
\end{aligned}
\tag{A41}
$$

Now, after all the series have been calculated, substitution of the corresponding formulas in the formula (A21) gives the final expression for the function $\bar{L}$:

$$
\begin{aligned}
\bar{L} = \frac{1}{4\pi}&\left\{\sin\varphi\left[\frac{\sin(x_0-x)}{\cosh|y-y_0|-\cos(x_0-x)}+\frac{\sin(x+x_0)}{\cosh|y-y_0|-\cos(x+x_0)}\right]\right. \\
&\mp\cos\varphi\left[\frac{\cos(x_0-x)-e^{-|y-y_0|}}{\cosh|y-y_0|-\cos(x_0-x)}-\frac{\cos(x+x_0)-e^{-|y-y_0|}}{\cosh|y-y_0|-\cos(x+x_0)}\right] \\
&+k^2|y-y_0|\left[\sin\varphi\left(\arctan\frac{\sin(x_0-x)e^{-|y-y_0|}}{1-e^{-|y-y_0|}\cos(x_0-x)}\right.\right. \\
&\left.\left.\left.+\arctan\frac{\sin(x_0+x)e^{-|y-y_0|}}{1-e^{-|y-y_0|}\cos(x_0+x)}\right)\mp\frac{\cos\varphi}{2}\ln\left(\frac{\cosh|y-y_0|-\cos(x+x_0)}{\cosh|y-y_0|-\cos(x-x_0)}\right)\right]\right\}.
\end{aligned}
\tag{A42}
$$

The new quickly converging representation of the waveguide Green's function derivative $\partial G(x,y;x_0,y_0)/\partial r$ can be represented as follows:

$$
\begin{aligned}
&\frac{\partial G(x,y;x_0,y_0,\varphi)}{\partial r} = \\
&\bar{L}(x,y;x_0,y_0,\varphi)+\sum_{n=1}^{\infty}\left(L_n(x,y;x_0,y_0,\varphi)-\bar{L}_n(x,y;x_0,y_0,\varphi)\right).
\end{aligned}
\tag{A43}
$$

where the functions $\bar{L}, L_n$, and $\bar{L}_n$ are determined by (A42), (A5b), and (A20).

17 Appendix B. Calculation of the Singular Integral.

The elements of the matrix of the system of linear equations (61) are defined by the double integral in the form of Eq. (63). However, the functions $\overline{K}(\varphi_v, \varphi_{l0})$ and $\overline{L}(\varphi_v, \varphi_{l0})$ have singularities when the source and the observation points coincide, e.i. when $v = l$ and $\varphi_v = \varphi_{l0}$. In the current work, this integral is taken by separating a small ε-vicinity of the singularity. Below are the corresponding calculations for the case of the symmetric waveguide with both pressure release boundaries. Symbols l and v are omitted, because the singularity exists only when the source and the observation points are on the surface of the same object.

17.1 Singularity in the Green's Function.

The function $\overline{K}(x, y; x_0, y_0)$, which is the asymptotic part of the Green's function, takes the following form in the case of the symmetric waveguide (54a):

$$\overline{K}(x, y; x_0, y_0) = \frac{1}{4\pi} \ln\left[\frac{\cosh|y - y_0| - \cos(x + x_0)}{\cosh|y - y_0| - \cos(x - x_0)}\right]. \tag{B1}$$

When the source and the observation points are on the surface of the scattering object, the Eq. (B1) can be rewritten as:

$$\overline{K}(\varphi, \varphi_0) = \frac{1}{4\pi} \ln\left[\frac{\cosh|R_0(\cos\varphi - \cos\varphi_0)| - \cos(R_0(\sin\varphi + \sin\varphi_0))}{\cosh|R_0(\cos\varphi - \cos\varphi_0)| - \cos(R_0(\sin\varphi - \sin\varphi_0))}\right]. \tag{B2}$$

The integral to be calculated:

$$I_{pm} = \int_0^{2\pi} \left\{ \int_0^{2\pi} \overline{K}(\varphi, \varphi_0) \exp(i(p\varphi_0 - m\varphi)) d\varphi_0 \right\} d\varphi, \tag{B3}$$

can be represented as:

$$I_{pm} = I_{pm}^{(1)} - I_{pm}^{(2)}, \tag{B4}$$

where

$$I_{pm}^{(1)} = \frac{1}{4\pi} \int_0^{2\pi} \left\{ \int_0^{2\pi} \ln[\cosh|R_0(\cos\varphi - \cos\varphi_0)| - \cos(R_0(\sin\varphi + \sin\varphi_0))] \right.$$
$$\left. \times \exp(i(p\varphi_0 - m\varphi)) d\varphi_0 \right\} d\varphi, \tag{B5}$$

$$I_{pm}^{(2)} = \frac{1}{4\pi} \int_0^{2\pi} \left\{ \int_0^{2\pi} \ln[\cosh|R_0(\cos\varphi - \cos\varphi_0)| - \cos(R_0(\sin\varphi - \sin\varphi_0))] \right.$$
$$\left. \times \exp(i(p\varphi_0 - m\varphi)) d\varphi_0 \right\} d\varphi. \tag{B6}$$

It may be noted that the singularity is contained only in the integral I_2.

Let the expression under the integral be denoted as:

$$f(\varphi, \varphi_0) = \ln[\cosh|R_0(\cos\varphi - \cos\varphi_0)| - \cos(R_0(\sin\varphi - \sin\varphi_0))]$$
$$\times \exp(i(p\varphi_0 - m\varphi)). \tag{B7}$$

The integral $I_{pm}^{(2)}$ over the square $0 \leq \varphi \leq \pi$, $0 \leq \varphi_0 \leq \pi$ on the plane (φ, φ_0) can be represented as a sum of integrals over the triangle $0 \leq \varphi \leq \pi$, $0 \leq \varphi_0 \leq \varphi$:

$$I_{pm}^{(2)} = \frac{1}{4\pi}\left(J_1 + J_2 + J_3 + J_4 + J_5 + J_6 + J_7 + J_8\right),$$
(B8)

$$J_1 = \int_0^\pi d\varphi \int_0^\varphi f(\varphi, \varphi_0) d\varphi_0 = \int_0^\pi d\varphi \int_0^\varphi f_1(\varphi, \varphi_0) d\varphi_0,$$
(B9)

$$J_2 = \int_0^\pi d\varphi \int_0^\varphi f(\varphi_0, \varphi) d\varphi_0 = \int_0^\pi d\varphi \int_0^\varphi f_2(\varphi, \varphi_0) d\varphi_0,$$
(B10)

$$J_3 = \int_0^\pi d\varphi \int_0^\varphi f(2\pi - \varphi, \varphi_0) d\varphi_0 = \int_0^\pi d\varphi \int_0^\varphi f_3(\varphi, \varphi_0) d\varphi_0,$$
(B11)

$$J_4 = \int_0^\pi d\varphi \int_0^\varphi f(2\pi - \varphi_0, \varphi) d\varphi_0 = \int_0^\pi d\varphi \int_0^\varphi f_4(\varphi, \varphi_0) d\varphi_0,$$
(B12)

$$J_5 = \int_0^\pi d\varphi \int_0^\varphi f(\varphi, 2\pi - \varphi_0) d\varphi_0 = \int_0^\pi d\varphi \int_0^\varphi f_5(\varphi, \varphi_0) d\varphi_0,$$
(B13)

$$J_6 = \int_0^\pi d\varphi \int_0^\varphi f(\varphi_0, 2\pi - \varphi) d\varphi_0 = \int_0^\pi d\varphi \int_0^\varphi f_6(\varphi, \varphi_0) d\varphi_0,$$
(B14)

$$J_7 = \int_0^\pi d\varphi \int_0^\varphi f(2\pi - \varphi, 2\pi - \varphi_0) d\varphi_0 = \int_0^\pi d\varphi \int_0^\varphi f_7(\varphi, \varphi_0) d\varphi_0,$$
(B15)

$$J_8 = \int_0^\pi d\varphi \int_0^\varphi f(2\pi - \varphi_0, 2\pi - \varphi) d\varphi_0 = \int_0^\pi d\varphi \int_0^\varphi f_8(\varphi, \varphi_0) d\varphi_0.$$
(B16)

Let a small ε-strip near the line $\varphi_0 = \varphi$ be separated from the integration triangle. After the substitution, $\varphi_0 = \varphi - \varepsilon$, $\varepsilon \ll 1$, the expression under the integral takes the form:

$$f_1^\varepsilon(\varphi, \varepsilon) = \ln\left[\cosh\left|R_0\left(\cos\varphi - \cos(\varphi - \varepsilon)\right)\right| - \cos\left(R_0\left(\sin\varphi - \sin(\varphi - \varepsilon)\right)\right)\right]$$
$$\times \exp\left[i(p - m)\varphi - p\varepsilon\right].$$
(B17)

All the integrals J, determined by Eqs. (B9) – (B16), can now be represented as a sum of two integrals, where the first integral does not have singularities, while the second integral is determined in the limit of small ε. The integrals J_n, $n = 1, 2, ..., 8$ take the following form:

$$J_n = J_n^0 + J_n^\varepsilon,$$
(B18)

$$J_n^0 = \int_0^\pi d\varphi \int_0^{\varphi - \varepsilon_0} f_n(\varphi, \varphi_0) d\varphi_0,$$
(B19)

$$J_n^\varepsilon = \lim_{\varepsilon_1 \to 0} \int_0^\pi d\varphi \int_{\varphi - \varepsilon_0}^{\varphi - \varepsilon_1} f_n(\varphi, \varphi_0) d\varphi_0 = \lim_{\varepsilon_1 \to 0} \int_0^\pi d\varphi \int_{\varepsilon_1}^{\varepsilon_0} f_n(\varphi, \varphi - \varepsilon) d\varepsilon.$$
(B20)

Here, ε_0 takes small, but finite, values.

Let the expression under the integral be represented as

$$f_1(\varphi, \varphi_0) = F_1(\varphi, \varphi_0)\exp\left[i(p\varphi_0 - m\varphi)\right],$$
(B21)

or, after the substitution $\varphi_0 = \varphi - \varepsilon$,

$$f_1^\varepsilon(\varphi,\varepsilon) = F_1^\varepsilon(\varphi,\varepsilon)\exp[i((p-m)\varphi - p\varepsilon)]. \tag{B22}$$

Here, $F_1^\varepsilon(\varphi,\varepsilon)$, is given by Eq. (B17) without the exponent:

$$F_1^\varepsilon(\varphi,\varepsilon) = \ln[\cosh|R_0(\cos\varphi - \cos(\varphi - \varepsilon))| - \cos(R_0(\sin\varphi - \sin(\varphi - \varepsilon)))]. \tag{B23}$$

The other functions $F_n^\varepsilon(\varphi,\varepsilon)$, $n = 2,3,...,8$, can be defined analogously.

By expanding $F_n^\varepsilon(\varphi,\varepsilon)$ into Taylor series with respect to ε, it may be shown that

$$F_1^\varepsilon(\varphi,\varepsilon) = F_2^\varepsilon(\varphi,\varepsilon) = F_7^\varepsilon(\varphi,\varepsilon) = F_8^\varepsilon(\varphi,\varepsilon) = \ln\left(\tfrac{1}{2}\varepsilon^2 R_0^2 + O(\varepsilon^4)\right). \tag{B24}$$

The other four functions $F_n^\varepsilon(\varphi,\varepsilon)$, $n = 3,4,5,6$, do not have singularities when ε tends to zero, which means that they do not contribute to the singular integral.

Now the singular integral J_1^ε can be found as:

$$J_1^\varepsilon = \lim_{\varepsilon_1 \to 0} \int_0^\pi d\varphi \int_{\varepsilon_1}^{\varepsilon_0} f(\varphi,\varphi - \varepsilon)d\varepsilon \cong$$

$$\int_0^\pi e^{i(p-m)\varphi} d\varphi \lim_{\varepsilon_1 \to 0} \int_{\varepsilon_1}^{\varepsilon_0} e^{-ip\varepsilon}\left(2\ln\varepsilon + \ln\frac{R_0^2}{2}\right)d\varepsilon. \tag{B25}$$

The integral over φ is determined easily:

$$\int_0^\pi e^{i(p-m)\varphi} d\varphi = \begin{cases} \dfrac{(-1)^{p-m}-1}{i(p-m)}, & p \neq m \\ \pi, & p = m \end{cases} \tag{B26}$$

The first term in the integral over ε has no singularities:

$$\ln\frac{R_0^2}{2}\lim_{\varepsilon_1 \to 0}\int_{\varepsilon_1}^{\varepsilon_0} e^{-ip\varepsilon} d\varepsilon = \ln\frac{R_0^2}{2}\begin{cases} \lim_{\varepsilon_1 \to 0}(\varepsilon_0 - \varepsilon_1), & p = 0 \\ \dfrac{-1}{ip}\lim_{\varepsilon_1 \to 0}\left(e^{-ip\varepsilon_0} - e^{-ip\varepsilon_1}\right), & p \neq 0 \end{cases}$$

$$= \varepsilon_0 \ln\frac{R_0^2}{2} + O(\varepsilon_0^2). \tag{B27}$$

The logarithmic term in Eq. (B25) has two different values depending on the value of p:

$$\lim_{\varepsilon_1 \to 0}\int_{\varepsilon_1}^{\varepsilon_0} e^{-ip\varepsilon}\ln\varepsilon\, d\varepsilon = \begin{cases} \lim_{\varepsilon_1 \to 0}\int_{\varepsilon_1}^{\varepsilon_0} \ln\varepsilon\, d\varepsilon, & p = 0 \\ \lim_{\varepsilon_1 \to 0}\int_{\varepsilon_1}^{\varepsilon_0} e^{-ip\varepsilon}\ln\varepsilon\, d\varepsilon, & p \neq 0 \end{cases} \tag{B28}$$

Using the well-known formula:

$$\int \ln x\, dx = x\ln x - x, \tag{B29}$$

the value of the integral at $p = 0$ is found:

$$\lim_{\varepsilon_1 \to 0} \int_{\varepsilon_1}^{\varepsilon_0} \ln \varepsilon \, d\varepsilon = \lim_{\varepsilon_1 \to 0} \left[\varepsilon \ln \varepsilon - \varepsilon \right]_{\varepsilon_1}^{\varepsilon_0} = \varepsilon_0 \ln \varepsilon_0 - \varepsilon_0 . \tag{B30}$$

Using the following formula (Dwight, 1961),

$$\int \frac{e^{ax} dx}{x} = \ln|x| + \sum_{n=1}^{\infty} \frac{a^n x^n}{nn!} \tag{B31}$$

the value of the integral (B28) at $p \neq 0$ may be expressed as:

$$\lim_{\varepsilon_1 \to 0} \int_{\varepsilon_1}^{\varepsilon_0} e^{-ip\varepsilon} \ln \varepsilon \, d\varepsilon = \lim_{\varepsilon_1 \to 0} \left[\ln|\varepsilon| + \sum_{n=1}^{\infty} \frac{(-ip)^n \varepsilon^n}{nn!} \right]_{\varepsilon_1}^{\varepsilon_0} = \varepsilon_0 \ln \varepsilon_0 - \varepsilon_0 - ip\varepsilon_0 + O(\varepsilon_0^2). \tag{B32}$$

Now the integral (B28) can be rewritten as:

$$\lim_{\varepsilon_1 \to 0} \int_{\varepsilon_1}^{\varepsilon_0} e^{-ip\varepsilon} \ln \varepsilon \, d\varepsilon = \varepsilon_0 \ln \varepsilon_0 - \varepsilon_0 - ip\varepsilon_0 + O(\varepsilon_0^2), \tag{B33}$$

and the integral J_1^{ε} equals

$$J_1^{\varepsilon} = \left[2(\varepsilon_0 \ln \varepsilon_0 - \varepsilon_0(1+ip)) + \varepsilon_0 \ln \frac{R_0^2}{2} \right] \times \begin{cases} i \dfrac{(-1)^{p-m} - 1}{(m-p)}, & p \neq m \\ \pi, & p = m \end{cases} . \tag{B34}$$

Let only the most significant term $O(\varepsilon_0 \ln \varepsilon_0)$ be left in Eq. (B34):

$$J_1^{\varepsilon} = \left[2\varepsilon_0 \ln \varepsilon_0 + O(\varepsilon_0) \right] \times \begin{cases} i \dfrac{(-1)^{p-m} - 1}{(m-p)}, & p \neq m \\ \pi, & p = m \end{cases} . \tag{B35}$$

It is clear from Eq. (B7), that $f(2\pi - \varphi, 2\pi - \varphi_0)$ is the complex conjugate of $f(\varphi, \varphi_0)$:

$$f(2\pi - \varphi, 2\pi - \varphi_0) = f^*(\varphi, \varphi_0). \tag{B36}$$

Consequently, the sum $J_1 + J_7$, including only terms of order $\varepsilon_0 \ln \varepsilon_0$, can be written as:

$$J_1^{\varepsilon} + J_7^{\varepsilon} = 2 \operatorname{Re} J_1^{\varepsilon} = \begin{cases} 4\pi\varepsilon_0 \ln \varepsilon_0, & p = m \\ 0 & p \neq m \end{cases} . \tag{B37}$$

The integrals J_2^{ε} and J_8^{ε} differ from J_1^{ε} and J_7^{ε} only by terms of order ε_0, and the sum of the four integrals can be determined by:

$$J_1^{\varepsilon} + J_2^{\varepsilon} + J_7^{\varepsilon} + J_8^{\varepsilon} = 4 \operatorname{Re} J_1^{\varepsilon} = \begin{cases} 8\pi\varepsilon_0 \ln \varepsilon_0, & p = m \\ 0 & p \neq m \end{cases} . \tag{B38}$$

Denoting $K(\varphi, \varphi_0) = \overline{K}(\varphi, \varphi_0) e^{i(p\varphi_0 - m\varphi)}$, it is possible to calculate the singular integral I_{pm} (Eq. (B3)), using the following formula:

$$I_{pm} = \int_0^{2\pi}\left\{\int_0^{2\pi} K(\varphi,\varphi_0)d\varphi_0\right\}d\varphi = \int_0^{2\pi}\left\{\int_0^{\varphi-\varepsilon_0}\left[K(\varphi,\varphi_0)+K(\varphi_0,\varphi)+\right.\right.$$

$$K(2\pi-\varphi,\varphi_0)+K(\varphi_0,2\pi-\varphi)+K(2\pi-\varphi_0,\varphi)+K(\varphi,2\pi-\varphi_0) \tag{B39}$$

$$+K(2\pi-\varphi,2\pi-\varphi_0)+K(2\pi-\varphi_0,2\pi-\varphi)\left]d\varphi_0\right\}d\varphi + 2\varepsilon_0\ln\varepsilon_0\delta_{pm} + O(\varepsilon_0),$$

where Kronecker's symbol $\delta_{pm} = \begin{cases} 1, & p=m \\ 0, & p\neq m \end{cases}$.

The first term in (B39), containing the sum of eight functions, does not have any singularities and can be evaluated numerically. The term $2\varepsilon_0\ln\varepsilon_0$ must be added to the diagonal matrix elements.

17.2   Singularity in the Derivative of the Green's Function.

The singularity in the asymptotic part of the derivative of the Green's function $\overline{L}(x,y;x_0,y_0)$ is resolved by means of techniques similar to those described in the previous section. The function $\overline{L}$ can be written as a sum of a non-singular, $\overline{L}_0$, and a singular, $\overline{L}_1$, term:

$$\overline{L} = \overline{L}_0 + \overline{L}_1, \tag{B40}$$

where the non-singular part is determined by

$$\overline{L}_0 = \frac{1}{4\pi}\left\{\frac{\cos[\varphi\pm(x_0+x)]-\cos\varphi\, e^{-|y-y_0|}}{\cosh|y-y_0|-\cos(x_0+x)}\right\}+$$

$$k^2|y-y_0|\left[\sin\varphi\left(\arctan\frac{\sin(x_0-x)e^{-|y-y_0|}}{1-e^{-|y-y_0|}\cos(x_0-x)}+\right.\right. \tag{B41}$$

$$\left.\arctan\frac{\sin(x_0+x)e^{-|y-y_0|}}{1-e^{-|y-y_0|}\cos(x_0+x)}\right)\mp\frac{\cos\varphi}{2}\ln\left(\frac{\cosh|y-y_0|-\cos(x+x_0)}{\cosh|y-y_0|-\cos(x-x_0)}\right)\left]\right\},$$

and the singular part in a simplified form is determined by:

$$\overline{L}_1 = \frac{1}{4\pi}\left\{\frac{\cos[\varphi\pm(x_0-x)]-\cos\varphi\, e^{-|y-y_0|}}{\cosh|y-y_0|-\cos(x_0-x)}\right\}. \tag{B42}$$

The top sign corresponds to $y>y_0$, while the bottom sign corresponds to $y<y_0$.

The function $\overline{L}_1$ has a singularity only when the source and the observation points are located on the surface of the same scattering object. In this case, the function describes the radial derivative of the Green's function and can be written as:

$$\overline{L}_1 = \frac{1}{4\pi}\left\{\frac{\cos[\varphi\pm R_0(\sin\varphi_0-\sin\varphi)]-\cos\varphi\, e^{-R_0|\cos\varphi-\cos\varphi_0|}}{\cosh[R_0|\cos\varphi-\cos\varphi_0|]-\cos[R_0(\sin\varphi_0-\sin\varphi)]}\right\}. \tag{B43}$$

The singular integral to be calculated now takes the following form:

$$I_{pm} = \int_0^{2\pi} \left\{ \int_0^{2\pi} \overline{L}_1(\varphi, \varphi_0) \exp(i(p\varphi_0 - m\varphi)) d\varphi_0 \right\} d\varphi \,. \tag{B44}$$

Denoting

$$f(\varphi, \varphi_0) = \frac{\cos[\varphi \pm R_0(\sin\varphi_0 - \sin\varphi)] - \cos\varphi \, e^{-R_0|\cos\varphi - \cos\varphi_0|}}{\cosh[R_0|\cos\varphi - \cos\varphi_0|] - \cos[R_0(\sin\varphi_0 - \sin\varphi)]} e^{i(p\varphi_0 - m\varphi)} \,, \tag{B45}$$

it is possible to represent the integral (B44) as a sum of eight integrals over the triangle $0 \leq \varphi \leq \pi, \quad 0 \leq \varphi_0 \leq \varphi$:

$$I_{pm} = \frac{1}{4\pi}(J_1 + J_2 + J_3 + J_4 + J_5 + J_6 + J_7 + J_8), \tag{B46}$$

$$J_1 = \int_0^\pi d\varphi \int_0^\varphi f(\varphi, \varphi_0) d\varphi_0 = \int_0^\pi d\varphi \int_0^\varphi f_1(\varphi, \varphi_0) d\varphi_0 \,, \tag{B47}$$

$$J_2 = \int_0^\pi d\varphi \int_0^\varphi f(\varphi_0, \varphi) d\varphi_0 = \int_0^\pi d\varphi \int_0^\varphi f_2(\varphi, \varphi_0) d\varphi_0 \,, \tag{B48}$$

$$J_3 = \int_0^\pi d\varphi \int_0^\varphi f(2\pi - \varphi, \varphi_0) d\varphi_0 = \int_0^\pi d\varphi \int_0^\varphi f_3(\varphi, \varphi_0) d\varphi_0 \,, \tag{B49}$$

$$J_4 = \int_0^\pi d\varphi \int_0^\varphi f(2\pi - \varphi_0, \varphi) d\varphi_0 = \int_0^\pi d\varphi \int_0^\varphi f_4(\varphi, \varphi_0) d\varphi_0 \,, \tag{B50}$$

$$J_5 = \int_0^\pi d\varphi \int_0^\varphi f(\varphi, 2\pi - \varphi_0) d\varphi_0 = \int_0^\pi d\varphi \int_0^\varphi f_5(\varphi, \varphi_0) d\varphi_0 \,, \tag{B51}$$

$$J_6 = \int_0^\pi d\varphi \int_0^\varphi f(\varphi_0, 2\pi - \varphi) d\varphi_0 = \int_0^\pi d\varphi \int_0^\varphi f_6(\varphi, \varphi_0) d\varphi_0 \,, \tag{B52}$$

$$J_7 = \int_0^\pi d\varphi \int_0^\varphi f(2\pi - \varphi, 2\pi - \varphi_0) d\varphi_0 = \int_0^\pi d\varphi \int_0^\varphi f_7(\varphi, \varphi_0) d\varphi_0 \,, \tag{B53}$$

$$J_8 = \int_0^\pi d\varphi \int_0^\varphi f(2\pi - \varphi_0, 2\pi - \varphi) d\varphi_0 = \int_0^\pi d\varphi \int_0^\varphi f_8(\varphi, \varphi_0) d\varphi_0 \,. \tag{B54}$$

After the substitution $\varphi_0 = \varphi - \varepsilon$, the expression under the integral takes the form:

$$f(\varphi, \varphi - \varepsilon) = \frac{\left(\cos[\varphi \pm R_0(\sin(\varphi - \varepsilon) - \sin\varphi)] - \cos\varphi \, e^{-R_0|\cos\varphi - \cos(\varphi - \varepsilon)|}\right) e^{i[(p-m)\varphi - p\varepsilon]}}{\cosh[R_0|\cos\varphi - \cos(\varphi - \varepsilon)|] - \cos[R_0(\sin(\varphi - \varepsilon) - \sin\varphi)]} \tag{B55}$$

As was done in the previous section, the integrals J_n, $n = 1,2,...,8$ defined by the formulas (B47) - (B54), are represented as the sum of an integral over a narrow ε - strip and an integral over the rest of the triangle:

$$J_n = J_n^0 + J_n^\varepsilon \,, \tag{B56}$$

$$J_n^0 = \int_0^\pi d\varphi \int_0^{\varphi - \varepsilon_0} f_n(\varphi, \varphi_0) d\varphi_0 \,, \tag{B57}$$

$$J_n^\varepsilon = \lim_{\varepsilon_1 \to 0} \int_0^\pi d\varphi \int_{\varphi - \varepsilon_0}^{\varphi - \varepsilon_1} f_n(\varphi, \varphi_0) d\varphi_0 = \lim_{\varepsilon_1 \to 0} \int_0^\pi d\varphi \int_{\varepsilon_1}^{\varepsilon_0} f_n(\varphi, \varphi - \varepsilon) d\varepsilon \,. \tag{B58}$$

Here ε_0 is small, but finite.

It can be concluded from Eq. (B45), that the integrals J_3^ε, J_4^ε J_5^ε, and J_6^ε do not include the singularity, because the denominator in Eq. (B45) does not tend to zero when $\varphi - \varphi_0$ in these cases.

Let the exponent be separated from the expression under the integral:

$$f_1(\varphi,\varphi_0) = F_1(\varphi,\varphi_0)\exp[i(p\varphi_0 - m\varphi)], \tag{B59}$$

or, after the substitution $\varphi_0 = \varphi - \varepsilon$:

$$f_1^\varepsilon(\varphi,\varepsilon) = F_1^\varepsilon(\varphi,\varepsilon)\exp[i((p-m)\varphi - p\varepsilon)]. \tag{B60}$$

Here $F_1^\varepsilon(\varphi,\varepsilon)$ is determined by:

$$F_1^\varepsilon(\varphi,\varepsilon) = \frac{\cos[\varphi \pm R_0(\sin(\varphi-\varepsilon)-\sin\varphi)] - \cos\varphi\, e^{-R_0|\cos\varphi-\cos(\varphi-\varepsilon)|}}{\cosh[R_0|\cos\varphi-\cos(\varphi-\varepsilon)|] - \cos[R_0(\sin(\varphi-\varepsilon)-\sin\varphi)]}. \tag{B61}$$

The other seven functions $F_n^\varepsilon(\varphi,\varepsilon)$ can be defined analogously.

As shown in the previous section, the denominator in the expression (B61) for small ε can be approximated as:

$$\cosh[R_0|\cos\varphi-\cos(\varphi-\varepsilon)|] - \cos[R_0(\sin(\varphi-\varepsilon)-\sin\varphi)] = \tfrac{1}{2}R_0^2\varepsilon^2 + O(\varepsilon^4). \tag{B62}$$

Consequently, in the numerator of Eq. (B61) only terms up to order ε must be considered, because higher order terms do not have the singularity when divided by the term of order ε^2.

The numerator can be approximated for small ε as follows:

$$\begin{aligned}
&\cos[\varphi + R_0(\sin(\varphi-\varepsilon)-\sin\varphi)] - \cos\varphi\, e^{-R_0|\cos\varphi-\cos(\varphi-\varepsilon)|} = \\
&\cos[\varphi - R_0\varepsilon\cos\varphi] - \cos\varphi(1 - R_0\varepsilon\sin\varphi) + O(\varepsilon^2) = \\
&\cos\varphi + R_0\varepsilon\cos\varphi\sin\varphi - \cos\varphi + R_0\varepsilon\cos\varphi\sin\varphi + O(\varepsilon^2) = R_0\varepsilon\sin 2\varphi + O(\varepsilon^2).
\end{aligned} \tag{B63}$$

Thus, $F_1^\varepsilon(\varphi,\varepsilon)$ can be written in the following form:

$$F_1^\varepsilon(\varphi,\varepsilon) = \frac{2\sin 2\varphi}{R_0\varepsilon} + O(\varepsilon^0). \tag{B64}$$

The singular integral J_1^ε now can be split into the product of two independent integrals over ε and φ.

$$J_1^\varepsilon = \frac{2}{R_0}\int_0^\pi e^{i(p-m)\varphi}\sin 2\varphi\, d\varphi \lim_{\varepsilon_1\to 0}\left[\int_{\varepsilon_1}^{\varepsilon_0}\frac{e^{-ip\varepsilon}}{\varepsilon}d\varepsilon\right]. \tag{B65}$$

With the use of the formula:

$$\int\frac{e^{ax}dx}{x} = \ln|x| + \sum_{n=1}^\infty \frac{a^n x^n}{nn!}, \tag{B66}$$

the integral over ε is found as follows:

$$\lim_{\varepsilon_1 \to 0}\left[\int_{\varepsilon_1}^{\varepsilon_0} \frac{e^{-ip\varepsilon}}{\varepsilon}d\varepsilon\right] = \lim_{\varepsilon_1 \to 0}\left|\frac{\varepsilon_0}{\varepsilon_1}\right| + O(\varepsilon_0).$$

(B67)

The calculation of the integral over φ requires the use of the formula (Dwight, 1961):

$$\int e^{ax}\sin(bx)dx = \frac{e^{ax}}{a^2 + b^2}[a\sin(bx) - b\cos(bx)].$$

(B68)

Now, taking into account that $a = i(p - m), b = 2$, the integral over φ can be found as follows:

$$\int_0^\pi e^{i(p-m)\varphi}\sin 2\varphi\, d\varphi = \frac{e^{i(p-m)\varphi}}{4-(p-m)^2}\left[i(p-m)\sin 2\varphi - 2\cos 2\varphi\right]\Bigg|_0^\pi = 0.$$

(B69)

The formula (B69) is correct if $|p - m| \neq 2$. In the case when $p - m = \pm 2$, the integral can be determined as:

$$\int_0^\pi e^{i(p-m)\varphi}\sin 2\varphi\, d\varphi = \int_0^\pi e^{\pm 2i\varphi}\sin 2\varphi\, d\varphi = \int_0^\pi \left(\cos 2\varphi \sin 2\varphi \pm i\sin^2 2\varphi\right)d\varphi =$$

$$\int_0^\pi \tfrac{1}{2}\sin 4\varphi\, d\varphi \pm \int_0^\pi i\sin^2 2\varphi\, d\varphi = -\tfrac{1}{8}\cos 4\varphi\Big|_0^\pi \pm i\left[\frac{1}{2} - \frac{\sin 4\varphi}{8}\right]\Bigg|_0^\pi = 0.$$

(B70)

Thus, the integral J_1^ε is equal to zero. It may be proved analogously, that the other three integrals containing singularities, J_2^ε, J_7^ε, and J_8^ε, also are zero. So, the singularities in the Green's function derivative may be ignored when calculating numerically the matrix elements (63). The line $\varphi = \varphi_0$, however, must be excluded from the area over which the integration is carried out in order to avoid a run-time computer error.

18 Appendix C. Modelling of Scattering by a Gas-Filled Shell.

This Appendix contains three derivations. The first derivation is that of the impedances for modes of the elastic shell. The second derivation is the expression for the integral reflection coefficient in terms of the modal coefficients, and the third derivation is that of the formula for the velocity distribution on the shell boundary.

18.1 The Impedances of an Elastic Gas-Filled Shell.

The theoretical description of the problem of scattering by homogeneous cylinders, provided in Section 8, can be extended to include scattering by an elastic gas-filled shell. The difference between the two cases is only in the expressions for the impedances of the scattering object, $z_m, -\infty < m < \infty$, which can be defined as:

$$z_m = -\left[\frac{\left(\partial P/\partial r\right)_m}{P_m}\right]_{r=R_1}.$$
(C1)

Here R_1 is the outer radius of the scattering object, and P_m is the m-th cylindrical component of the acoustic pressure. In the case of solid cylinders the z_m are described by Eqs. (32)-(36) and (64).

The waveguide configuration to be considered is shown in Fig. 11. As shown in the figure, a plane two-dimensional waveguide is filled with a homogeneous fluid. An elastic cylindrical shell of external radius R_1 and internal radius R_2 is immersed in the waveguide. The fluid is described by the sound speed, c, and the density, ρ. The shell is described by the Lame coefficients, λ, μ, and the density ρ_s. The gas in the interior of the shell is characterised by the sound speed, c_g, and the density, ρ_g.

The displacement vector $\vec{r}$ in the shell wall is, as previously described (see Eq. (2)), the sum of longitudinal and transversal waves:

$$\Delta \vec{r}(r, \varphi) = \nabla \Phi(r, \varphi) + \nabla \times F(r, \varphi),$$
(C2)

where $\Phi(r, \varphi)$ and $F(r, \varphi)$ are the corresponding potentials. However, the expressions for the potentials in the case of the shell include the Bessel's functions of the second kind, $Y_m(r, \varphi)$:

$$F(r, \varphi) = \sum_{m=-\infty}^{\infty}\left[A_m^J J_m(k_t r) + A_m^Y Y_m(k_t r)\right]e^{im\varphi},$$
(C3)

$$\Phi(r, \varphi) = \sum_{m=-\infty}^{\infty}\left[B_m^J J_m(k_l r) + B_m^Y Y_m(k_l r)\right]e^{im\varphi}.$$
(C4)

The pressure field on the external shell boundary may be expressed as a Fourier series:

$$P(R_1, \varphi) = \sum_{m=-\infty}^{\infty}P_m e^{im\varphi}.$$
(C5)

The pressure field in the gas-filled interior, $P_g(r, \varphi)$, is described by a series of cylindrical functions of the first kind:

$$P_g(r, \varphi) = \sum_{m=-\infty}^{\infty} P_m^g J_m(k_g r) e^{im\varphi} \, . \tag{C6}$$

Conditions on the external shell boundary are similar to the conditions (9) - (11):

$$\left[2\frac{\partial}{\partial r}\left(\frac{1}{r}\frac{\partial \Phi}{\partial \varphi}\right) - k_t^2 F - 2\frac{\partial^2 F}{\partial r^2} \right]_{r=R_1} = 0 \, , \tag{C7}$$

$$2\mu\left[\frac{\pi}{D}\right]^2 \left[\frac{\partial}{\partial r}\left(\frac{1}{r}\frac{\partial F}{\partial \varphi}\right) - \frac{\lambda}{2\mu}k_l^2\Phi + \frac{\partial^2 \Phi}{\partial r^2} \right]_{r=R_1} = -P|_{r=R_1} \, , \tag{C8}$$

$$\left[\frac{\pi}{D}\right]^2 \left[\frac{\partial \Phi}{\partial r} + \frac{1}{r}\frac{\partial F}{\partial \varphi} \right]_{r=R_1} = \left[\frac{1}{\rho(kc)^2}\frac{\partial P}{\partial r} \right]_{r=R_1} \, . \tag{C9}$$

Conditions on the internal shell boundary are analogous to the conditions (C7) - (C9) with the replacement of the pressure in the fluid P with the pressure in the gas P_g, and the external radius R_1 with the internal radius R_2:

$$\left[2\frac{\partial}{\partial r}\left(\frac{1}{r}\frac{\partial \Phi}{\partial \varphi}\right) - k_t^2 F - 2\frac{\partial^2 F}{\partial r^2} \right]_{r=R_2} = 0 \, , \tag{C10}$$

$$2\mu\left[\frac{\pi}{D}\right]^2 \left[\frac{\partial}{\partial r}\left(\frac{1}{r}\frac{\partial F}{\partial \varphi}\right) - \frac{\lambda}{2\mu}k_l^2\Phi + \frac{\partial^2 \Phi}{\partial r^2} \right]_{r=R_2} = -P_g|_{r=R_2} \, , \tag{C11}$$

$$\left[\frac{\pi}{D}\right]^2 \left[\frac{\partial \Phi}{\partial r} + \frac{1}{r}\frac{\partial F}{\partial \varphi} \right]_{r=R_2} = \left[\frac{1}{\rho(k_g c_g)^2}\frac{\partial P_g}{\partial r} \right]_{r=R_2} \, . \tag{C12}$$

To obtain expressions for the impedances, the solutions in the form of Eqs. (C3) - (C5) must be substituted into the boundary conditions (C7) - (C12).

After substitution of the solutions (C3) - (C5), the condition (C8) will take the following form:

$$2\mu\left[\frac{\pi}{D}\right]^2 \sum_{m=-\infty}^{\infty} \left\{ \left[B_m^J k_l^2\left(J_m''(k_l R_1) - \frac{\lambda}{2\mu}J_m(k_l R_1) \right) \right. \right.$$
$$+ B_m^Y k_l^2\left(Y_m''(k_l R_1) - \frac{\lambda}{2\mu}Y_m(k_l R_1) \right) + A_m^J im\left(\frac{k_t}{R_1}J_m'(k_t R_1) - \frac{1}{R_1^2}J_m(k_t R_1) \right) \tag{C13}$$
$$\left. \left. + A_m^Y im\left(\frac{k_t}{R_1}Y_m'(k_t R_1) - \frac{1}{R_1^2}Y_m(k_t R_1) \right) \right] e^{im\varphi} \right\} = -P_m e^{im\varphi} \, .$$

Let the above expression be multiplied by $\frac{1}{2\pi}e^{-ip\varphi}, -\infty < p < \infty$ and integrated over φ from 0 to 2π. Due to the orthogonality of the functions $e^{im\varphi}$:

$$\int_0^{2\pi} e^{im\varphi}e^{-ip\varphi}d\varphi = \begin{cases} 2\pi, & p=m \\ 0, & p \neq m \end{cases},$$ (C14)

the term $e^{im\varphi}$ may be dropped and the Eq. (C13) may be written for every m-th term separately:

$$2\mu\left[\frac{\pi}{D}\right]^2\left[B_m^J k_l^2\left(J_m''(k_l R_1) - \frac{\lambda}{2\mu}J_m(k_l R_1)\right) + B_m^Y k_l^2\left(Y_m''(k_l R_1) - \frac{\lambda}{2\mu}Y_m(k_l R_1)\right)\right.$$
$$\left.+ A_m^J im\left(\frac{k_t}{R_1}J_m'(k_t R_1) - \frac{1}{R_1^2}J_m(k_t R_1)\right) + A_m^Y im\left(\frac{k_t}{R_1}Y_m'(k_t R_1) - \frac{1}{R_1^2}Y_m(k_t R_1)\right)\right]$$ (C15)
$$= -P_m, \quad -\infty < m < \infty.$$

Denoting

$$\Phi_{1m}^J(x) = 2m[xJ_m'(x) - J_m(x)],$$ (C16)

$$\Phi_{1m}^Y(x) = 2m[xY_m'(x) - Y_m(x)],$$ (C17)

$$\Phi_{3m}^J(x) = 2x^2\left[J_m''(x) - \frac{\lambda}{2\mu}J_m(x)\right],$$ (C18)

$$\Phi_{3m}^Y(x) = 2x^2\left[Y_m''(x) - \frac{\lambda}{2\mu}Y_m(x)\right],$$ (C19)

it is possible to rewrite Eq. (C13) as:

$$\frac{\mu}{R_1^2}\left[\frac{\pi}{D}\right]^2\left[B_m^J\Phi_{3m}^J(k_l R_1) + B_m^Y\Phi_{3m}^Y(k_l R_1) + A_m^J i\Phi_{1m}^J(k_t R_1) + A_m^Y i\Phi_{1m}^Y(k_t R_1)\right]$$
$$= -P_m.$$ (C20)

The next step is to find the derivative of the pressure on the external boundary. After substitution of the solutions, the condition (C9), takes the following form:

$$\frac{\rho(kc)^2}{R_1}\left[\frac{\pi}{D}\right]^2$$
$$\times\left[k_l R_1 B_m^J J_m'(k_l R_1) + k_l R_1 B_m^Y Y_m'(k_l R_1) + im A_m^J J_m(k_t R_1) + im A_m^Y Y_m(k_t R_1)\right]$$ (C21)
$$= \left(\frac{\partial P}{\partial r}\right)_m\bigg|_{r=R_1}$$

An expression for z_m is obtained by dividing Eq. (C21) by Eq. (C20):

$$z_m = \frac{\rho R_1 (kc)^2}{\mu}$$

$$\times \left[\frac{k_l R_1 \left(B_m^J J_m'(k_l R_1) + B_m^Y Y_m'(k_l R_1) \right) + im \left(A_m^J J_m(k_t R_1) + A_m^Y Y_m(k_t R_1) \right)}{B_m^J \Phi_{3m}^J(k_l R_1) + B_m^Y \Phi_{3m}^Y(k_l R_1) + A_m^J i \Phi_{1m}^J(k_t R_1) + A_m^Y i \Phi_{1m}^Y(k_t R_1)} \right]. \tag{C22}$$

The coefficients $A_m^J, A_m^Y, B_m^J, B_m^Y$ will be determined from the boundary conditions (C7) and (C10) – (C12).

Substitution of the solutions (C3) - (C5) into the condition (C7), gives the following equation:

$$2imB_m^J \left[k_l R_1 J_m'(k_l R_1) - J_m(k_l R_1) \right] + 2imB_m^Y \left[k_l R_1 Y_m'(k_l R_1) - Y_m(k_l R_1) \right]$$
$$- k_t^2 R_1^2 A_m^J \left[J_m(k_t R_1) + 2J_m''(k_t R_1) \right] - k_t^2 R_1^2 A_m^Y \left[Y_m(k_t R_1) + 2Y_m''(k_t R_1) \right] = 0. \tag{C23}$$

Introducing auxiliary functions:

$$\Phi_{2m}^J(x) = x^2 \left[2J_m''(x) + J_m(x) \right], \tag{C24}$$

$$\Phi_{2m}^Y(x) = x^2 \left[2Y_m''(x) + Y_m(x) \right], \tag{C25}$$

Eq. (C23) takes the following form:

$$iB_m^J \Phi_{1m}^J(k_l R_1) + iB_m^Y \Phi_{1m}^Y(k_l R_1) - A_m^J \Phi_{2m}^J(k_t R_1) - A_m^Y \Phi_{2m}^Y(k_t R_1) = 0. \tag{C26}$$

The conditions on the internal boundary of the shell can be written analogously to the conditions on the external boundary. Replacing R_1 with R_2, P with P_g, and $(kc)^2$ with $(k_g c_g)^2$ in Eqs. (C20), (C21) and (C26) the following expression is obtained:

$$\frac{\mu}{R_2^2} \left[\frac{\pi}{D} \right]^2 \left[B_m^J \Phi_{3m}^J(k_l R_2) + B_m^Y \Phi_{3m}^Y(k_l R_2) + A_m^J i \Phi_{1m}^J(k_t R_2) + A_m^Y i \Phi_{1m}^Y(k_t R_2) \right]$$
$$= -P_m^g J_m(k_g R_2), \tag{C27}$$

$$\frac{\rho (k_g c_g)^2}{R_2} \left[\frac{\pi}{D} \right]^2$$
$$\times \left[k_l R_2 B_m^J J_m'(k_l R_2) + k_l R_2 B_m^Y Y_m'(k_l R_2) + im A_m^J J_m(k_t R_2) + im A_m^Y Y_m(k_t R_2) \right]$$
$$= P_m^g k_g J_m'(k_g R_2), \tag{C28}$$

$$iB_m^J \Phi_{1m}^J(k_l R_2) + iB_m^Y \Phi_{1m}^Y(k_l R_2) - A_m^J \Phi_{2m}^J(k_t R_2) - A_m^Y \Phi_{2m}^Y(k_t R_2) = 0. \tag{C29}$$

Eqs. (C26) - (C29) comprise a system of linear equations for determining the coefficients $A_m^J, A_m^Y, B_m^J, B_m^Y$. In matrix form the system can be written as:

$$\begin{Vmatrix} \Phi_{2m}^{J}(k_t R_1) & \Phi_{2m}^{Y}(k_t R_1) & -i\Phi_{1m}^{J}(k_l R_1) & -i\Phi_{1m}^{Y}(k_l R_1) \\ \Phi_{2m}^{J}(k_t R_2) & \Phi_{2m}^{Y}(k_t R_2) & -i\Phi_{1m}^{J}(k_l R_2) & -i\Phi_{1m}^{Y}(k_l R_2) \\ imJ_m(k_t R_2) & imY_m(k_t R_2) & R_2 k_l J'_m(k_l R_2) & R_2 k_l Y'_m(k_l R_2) \\ i\Phi_{1m}^{J}(k_t R_2) & i\Phi_{1m}^{Y}(k_t R_2) & \Phi_{3m}^{J}(k_l R_2) & \Phi_{3m}^{Y}(k_l R_2) \end{Vmatrix} \begin{pmatrix} A_m^J \\ A_m^Y \\ B_m^J \\ B_m^Y \end{pmatrix}$$

$$= \begin{pmatrix} 0 \\ 0 \\ \dfrac{P_m^g k_g R_2 J'_m(k_g R_2)}{\rho_g (k_g c_g)^2}\left[\dfrac{D}{\pi}\right]^2 \\ -\dfrac{P_m^g}{\mu} R_2^2 J_m(k_g R_2)\left[\dfrac{D}{\pi}\right]^2 \end{pmatrix} \qquad (C30)$$

The system of equations (C30) allows determination of the coefficients $A_m^J, A_m^Y, B_m^J, B_m^Y$, which then can be used in Eq. (C22) for the calculation of the impedances z_m. The parameters P_m^g, which characterise the amplitudes of the acoustic pressure inside the shell, are still unknown. However, both numerator and denominator in Eq. (C22) linearly depend on the coefficients $A_m^J, A_m^Y, B_m^J, B_m^Y$, which are solutions of the system (C30). As a result, the z_m do not depend on the value of P_m^g, and any value different from zero can be used in Eq. (C30).

18.2   Definition of the Reflection Coefficient.

The reflection coefficient R_c can be defined as S^-/S_e, where S_e is the total amount of acoustic energy in the incident wave moving through a vertical cross-section of the waveguide in unit time, and S^- is the amount of energy reflected in the backward direction from the shell.

To obtain an expression for the reflection coefficient, the external pressure field in the waveguide is represented as a series of waveguide modes (see Eq. (17)):

$$P_e(x,y) = \sum_{n=1}^{\infty} \overline{A}_n e^{ig_n y} \sin(\eta_n x - \theta_n). \qquad (C31)$$

The reflected wave propagates in the opposite direction:

$$P^-(x,y) = \sum_{n=1}^{\infty} A_n^- e^{-ig_n y} \sin(\eta_n x - \theta_n). \qquad (C32)$$

The intensity vector $\vec{I}$ in an acoustic wave is determined by the formula (Landau, 1959):

$$I_y(x,y) = \frac{1}{2}\mathrm{Re}\left[P(x,y)V_y^*(x,y)\right]. \qquad (C33)$$

The horizontal component of the acoustic velocity vector, V_y, is related to the pressure field by the following expression:

$$V_y(x, y) = -\frac{i}{\rho\omega}\frac{\partial P(x, y)}{\partial y}.$$ (C34)

The total power flow through the vertical cross-section of the waveguide is determined by integrating the expression (C34) over the vertical coordinate:

$$S = \int_0^\pi I_y(x, y)dy.$$ (C35)

The substitution of Eqs. (C31) and (C32) into Eqs. (C33) - (C35) gives the following expressions for S^- and S_e:

$$S_e = \frac{\pi}{4\rho ck}\sum_{n=0}^{\infty}\left[\left|\overline{A}_n\right|^2 \operatorname{Re} g_n\right],$$ (C36)

$$S^- = \frac{\pi}{4\rho ck}\sum_{n=0}^{\infty}\left[\left|A_n^-\right|^2 \operatorname{Re} g_n\right].$$ (C37)

The longitudinal wavenumbers g_n are defined by the following expression (see text):

$$g_n = (k^2 - \eta_n^2)^{1/2}.$$ (C38)

It is clear from Eq. (C38), that the g_n are purely real if $\eta_n < k$, and purely imaginary if $\eta_n > k$, which means that the higher order modes do not transmit acoustic energy. Consequently, the above equations can be rewritten as:

$$S_e = \frac{\pi}{4\rho ck}\sum_{n=0}^{\eta_n}\left[\left|\overline{A}_n\right|^2 g_n\right],$$ (C39)

$$S^- = \frac{\pi}{4\rho ck}\sum_{n=0}^{\eta_n}\left[\left|A_n^-\right|^2 g_n\right].$$ (C40)

Then the reflection coefficient is defined by dividing (C40) by (C39):

$$R_c = \frac{S^-}{S_e} = \frac{\displaystyle\sum_{n=0}^{\eta_n}\left[\left|\overline{A}_n\right|^2 g_n\right]}{\displaystyle\sum_{n=0}^{\eta_n}\left[\left|A_n^-\right|^2 g_n\right]}.$$ (C41)

It is to be observed that only propagating lower order modes are taken into account in Eq. (C41).

18.3 *Velocity Amplitude on the Shell Boundary.*

This section contains the derivation of expressions linking the velocity amplitude on the surface of the shell with the coefficients b_m. These coefficients represent the solution of the system of linear equations, to which the original boundary value problem is reduced.

The radial derivative of the total acoustic field on the surface of the shell can be represented as a Fourier series in terms of basis functions $e^{im\varphi}, -\infty < m < \infty$:

$$\left[\frac{\partial P}{\partial r}\right]_{r=R_1} = \sum_{m=-\infty}^{\infty} \left[\left(\frac{\partial P}{\partial r}\right)_m\right]_{r=R_1} e^{im\varphi} \ . \tag{C42}$$

The total pressure field P in the fluid is the sum of the incident and the scattered field. It was shown in this work previously, that the incident field might be represented as a sum of cylindrical functions (see Eq. (18)):

$$P_e(x,y) = \sum_{m=-\infty}^{\infty} a_m J_m(kr) e^{im\varphi} \ . \tag{C43}$$

The components of the derivative of the scattered field may be expressed in terms of the coefficients b_m and the scattering matrix $\|\Lambda\|$ (see Eq. (60)):

$$\left[\left(\frac{\partial P_s}{\partial r}\right)_m\right]_{r=R_1} = b_m + \sum_{p=-\infty}^{\infty} b_p \Lambda_{pm} \ . \tag{C44}$$

Differentiating Eq. (C43) and adding Eqs. (C43) and (C44) together gives the following formula for the m-th component of the radial derivative of the total acoustic field on the surface of the shell:

$$\left[\left(\frac{\partial P}{\partial r}\right)_m\right]_{r=R_1} = kJ'_m(kR_1)a_m + b_m + \sum_{p=-\infty}^{\infty} b_p \Lambda_{pm} \ . \tag{C45}$$

The velocity amplitude V on the surface can be calculated easily from the radial pressure derivative using the following formula:

$$V\big|_{r=R_1} = \frac{D}{\pi\rho ck}\left[\frac{\partial P}{\partial r}\right]_{r=R_1}, \tag{C46}$$

where D is the waveguide depth, ρ is the fluid density, c is the sound speed in the fluid, and k is the non-dimensional wavenumber $k = 2D/\lambda$.

19 Bibliography.

Barnard, G.R. and McKinney, C.M. (1961), "Scattering of acoustic energy by solid and air-filled cylinders in water", J.Acoust.Soc.Am., **33**, 226-238.

Belov, V.E., Gorskii, S.M., Zinoviev, A.Y. and Khilko, A.I. (1994a), "Application of the method of integral equations to diffraction of acoustic waves at elastic bodies in a layer of liquid", Acoust. Phys., **40** (4), pp. 485-496.

Belov, V.E., Gorskii, S.M., Zinoviev, A.Y. and Khilko, A.I. (1994b), "Acoustic monitoring of plane-stratified media with elastic cylindrical inclusions", Acoust. Phys., **40**, p 298.

Belov, V.E., Gorskii, S.M., Zinoviev, A.Y. and Khil'ko, A.I. (1994c), "Application of the method of integral equations to diffraction of acoustic waves at elastic bodies in a layer of liquid", Radiotekhnika i Elektronika, **40** (4) 548-560, (in Russian)

Belov, V.E., Gorskii, S.M., Zinoviev, A.Y. and Khilko A.I. (1994d), "Diffraction of the acoustical fields by the elastic bodies in oceanic waveguides: solution by the combine integral method", Proceedings of the 2nd European conference on underwater acoustics, Copenhagen, Denmark. 4-8 July, 1994.

Belov, V.E., Gorskii, S.M., Zalezsky, A.A. and Zinoviev, A.Y. (1998), "Application of the integral equation method to acoustic wave diffraction from elastic bodies in a fluid layer", J. Acoust. Soc. Am. **103** (3), 1288-1295.

Breitenbach, Edward D., Überall, Herbert and Yoo, Kwang-Bock (1983), "Resonant Acoustic Scattering from Elastic Cylindrical Shells", J.Acoust.Soc.Am., **74**, 1267-1273.

Brekhovskikh, L.M. (1960), "Waves in Layered Media", Academic Press Inc., New York, p.41.

Brekhovskikh, L.M. (1967), "Surface Waves in a Solid", Sov. Phys. - Acoust., **12,** 320-325.

Brekhovskikh, L.M. (1968), "Surface Waves Confined to the Curvature of the Boundary in Solids", Sov. Phys. - Acoust., **13,** 462-472.

Brill, D., Überall, H. (1971), "Acoustic Waves Transmitted through Solid Elastic Cylinders", J.Acoust.Soc.Am., **50**, 921-939.

Dickey, J.W., Frisk, G.V. and Überall, H. (1976), "Whispering Gallery Modes on Elastic Cylinders", J.Acoust.Soc.Am., **59**, 1339-1346.

Dickey, J.W. and Überall, H. (1978), "Surface Wave Resonances in Sound Scattering from Elastic Cylinders", **63**, 319-320.

Dwight, H.B. (1961), "Tables of integrals and other mathematical data", The Macmillan Company, New York.

Donskoi, D.M., Zinoviev, A.Y., Chichagov, P.K. (1990), "Experimental study of the influence of gas cavity on the radiation of sound from a piston", Acoust. Phys., **36** (5), 480-481.

Doolittle, R.D., McNicholas, J.V. and Überall, H. (1967), "Circumferential Sound Pulses on Elastic Cylinders", J.Acoust.Soc.Am., **42**, 522-523.

Doolittle, R.D., Überall, H. and Ugincius, P. (1968), "Sound Scattering by Elastic Cylinders", J.Acoust.Soc.Am., **43**, 1-14.

Doolittle, R.D., Überall, H. (1966), "Sound Scattering by Elastic Cylindrical Shells", J.Acoust.Soc.Am., **39**, 272-275.

Flax, L., Dragonette, L.R. and H.Überall (1978), "Theory of Elastic Resonance Excitation by Sound Scattering", J.Acoust.Soc.Am., **63**, 723-731.

Franz, W. and Deppermann, K. (1952), Ann. Phys., **10**, 361-373.

Frisk, G.V., Dickey, J.W. and Überall, H. (1975), "Surface Wave Modes on Elastic Cylinders", J.Acoust.Soc.Am., **58**, 996-1008.

Frisk, G.V. and Überall, H. (1976), "Creeping Waves and Lateral Waves in Acoustic Scattering by Large Elastic Cylinders", J.Acoust.Soc.Am., **59**, 46-54.

Gaunaurd, Guillermo C. (1989), "Elastic and Acoustic Resonance Wave Scattering", Appl.Mech.Rev., **42**, 143-192.

Gaunaurd, G.C., Brill, D. (1984), "Acoustic Spectrogram and Complex-Frequency Poles of a Resonantly Excited Elastic Tube", J.Acoust.Soc.Am., **75**, 1681-1693.

Gaunaurd, G.C., Werby, M.F. (1991), "Similarities between Various Lamb Waves in Submerged Spherical Shells, and Rayleigh Waves in Elastic Spheres and Flat Half-Spaces", J.Acoust.Soc.Am., **89**, 2731-2739.

Glushkov, E., Glushkova, N. (1997), "Blocking property of energy vortices in elastic waveguides", J. Acoust. Soc. Am., **102**, 1356-1360.

Goodman, R.R., Bunney, R.E. and Marshall, S.W. (1967), "Observation of Circumferential Waves on Solid Aluminium Cylinders", J.Acoust.Soc.Am., **42**, 523-524.

Grace, O.D. and Goodman, R.R. (1966), "Circumferential waves on solid cylinders", J.Acoust.Soc.Am., **39**, 173-174.

Hickling, R. (1967), "Echoes from Spherical Shells in Air", J.Acoust.Soc.Am., **42**, 388-390.

Hickling, R., Burrows, R. K., Ball, J. F., Petrovic, M. (1991), "Power flow for sound incident on a solid aluminium sphere in water, J. Acoust. Soc. Am., **89**, 2509-2518.

Horton, C.W., King W.R. and Diercks, K.S.,(1962), "Theoretical analysis of the scattering of short acoustic pulses by a thin-walled metallic cylinder in water", J.Acoust.Soc.Am", **34**, 1929-1932.

Izbicki, J.L., Maze, G. and Ripoche, J. (1986), "Influence of the Free Modes of Vibration on the Acoustic Scattering of a Circular Cylindrical Shell", J.Acoust.Soc.Am., **80**, 1215-1219.

Landau, L.D and Lifshitz, E.M. (1959), "Fluid Mechanics", Pergamon Press, London.

Lapin, A.D. (1969), "Propagation of Surface Waves over Curved Surfaces", Sov.Phys.-Acoust., **15**, 201-204.

Lethullier, S., Pareige, P., Izbicki, J.L. and Conoir J.M. (1998), "Scattering by Two Adjacent Immersed Shells: Theory and Experiment", Proceedings of the 4th European Conference on Underwater Acoustics, Rome, Italy, Sep. 21 – 25 1998, **2**, 837-842.

McNicholas, J.V., Überall, H. and Choate, K. (1968), "Pulse Shapes of Creeping Waves around Soft Cylinders", J.Acoust.Soc.Am., **44**, 752-764.

Murphy, J. Diarmuid, Breitenbach, Edward D. and Überall, Herbert (1978), "Resonance Scattering of Acoustic Waves from Cylindrical Shells", J.Acoust.Soc.Am., **64**, 677-683.

Numrich, S.K., Howell, W.E., Subrahmanyam, J.V. and Überall, H. (1986), "Acoustic Ringing Response of the Individual Resonances of and Elastic Cylinder", J.Acoust.Soc.Am., **80**, 1161-1169.

Press, W.H, Flannery, B.P., Teukolsky, S.A. and Vetterling W.T. (1988), "Numerical recipes – the art of scientific programming", Cambridge University Press, Cambridge.

Prudnikov, A.P., Brychkov, Yu. A. and Marichev, O.I. (1986), Integrals and series. Elementary functions", Gordon and Breach Science Publishers, New York.

Rayleigh (1885), "On Waves Propagated Along the Plane Surface of an Elastic Solid", Proc. London Math. Soc **17**, 4-11.

Skelton, E. A., Waterhouse, R. V. (1986), "Energy streamlines for a spherical shell scattering plane waves", J. Acoust. Soc. Am., **80**, 1473-1478.

Stoneley, R. (1924), Proc. R. Soc. Lond. **A 106**, 416-428.

Talmant, M., Quentin, G., Rousselot, J.L., Subrahmanyam, J.V. and Überall, H. (1988), "Acoustic Resonances of Thin Cylindrical Shells and the Resonance Scattering Theory", J.Acoust.Soc.Am., **84**, 681-688.

Talmant, Maryline, Überall H., Miller, Russel D., Werby, Michael F. and Dickey, J. W. (1989), "Lamb Waves and Fluid-Borne Waves on Water-Loaded, Air-Filled Thin Cylindrical Shells", J.Acoust.Soc.Am., **86**, 278-289.

Überall, H., Doolittle, R.D. and McNicholas, J.V. (1966), "Use of Sound Pulses for a Study of Circumferential Waves", J.Acoust.Soc.Am., **39**, 564-578.

Überall, H., Dragonette, L.R. and Flax, L. (1977), "Relation Between Creeping Waves and Normal Modes of Vibration of a Curved Body", J.Acoust.Soc.Am., **61**, 711-715 (1977).

Ugincius, P. and Überall, H. (1968), "Creeping-Wave Analysis of Acoustic Scattering by Elastic Cylindrical Shells", J.Acoust.Soc.Am., **43**, 1025-1035.

Urick, R. J. (1983), "Principles of underwater sound", 3rd edition, McGraw-Hill.

Victorov, I.A. (1967), "Rayleigh and Lamb Waves: Physical Theory and Applications", Plenum Press, New York.

Wu, T.W. (1994), "On computational aspects of the boundary element method for acoustic radiation and scattering in a perfect waveguide", J.Acoust. Soc. Am., **96**, (6), 3733-3743.

Zinoviev. A. (1997), Sound Wave Scattering from an Air Filled Shell in a Layer of Liquid. Proceedings of the Fifth International Congress on Sound and Vibration, University of Adelaide, South Australia, Dec. 15 - 18, 1997, **4**, 1985-1993.

Zinoviev, A. (2000), An Investigation of Surface Waves on a Cylindrical Scattering Object in a Fluid Layer. Submitted for publication to the 5th European Conference on Undewater Acoustics, Lyon, France, 10 –13 July 2000.

Zinoviev, A., Belov, V. (1998), "Energy Flow of an Acoustic Wave Scattered by a Resonant Elastic Cylinder in a Layer of Liquid", Proceedings of the 23rd International Conference on Noise and Vibration Engineering (ISMA23), Leuven, Belgium, Sep. 16-18 1998, pp.685-690.

Zinoviev, A., and Bies, D.A. (1998), "Oscillations of a gas filled elastic shell in an acoustic wave in a layer of liquid", Proceedings of the 4th European Conference on Underwater Acoustics, Rome, Italy, Sep. 21 – 25 1998, **2**, 909-914.

20 Publications Originating from the Thesis.

20.1 Main Publications.

20.1.1 Refereed Journal Publication.

Belov, V.E., Gorskii, S.M., Zalezsky, A.A. and Zinoviev, A.Y. (1998) "Application of the integral equation method to acoustic wave diffraction from elastic bodies in a fluid layer", J. Acoust. Soc. Am. **103** (3), 1288-1295.

20.1.2 Conference Proceedings.

Zinoviev. A. (1997) Sound Wave Scattering from an Air Filled Shell in a Layer of Liquid. Proceedings of the Fifth International Congress on Sound and Vibration, University of Adelaide, South Australia, Dec. 15 - 18, 1997, **4**, 1985-1993.

Zinoviev, A. (2000), An Investigation of Surface Waves on a Cylindrical Scattering Object in a Fluid Layer. Submitted for publication to the 5th European Conference on Undewater Acoustics, Lyon, France, 10 –13 July 2000.

Zinoviev, A., Belov, V. (1998), "Energy Flow of an Acoustic Wave Scattered by a Resonant Elastic Cylinder in a Layer of Liquid", Proceedings of the 23rd International Conference on Noise and Vibration Engineering (ISMA23), Leuven, Belgium, Sep. 16-18 1998, pp.685-690.

Zinoviev, A., and Bies, D.A. (1998), "Oscillations of a gas filled elastic shell in an acoustic wave in a layer of liquid", Proceedings of the 4th European Conference on Underwater Acoustics, Rome, Italy, Sep. 21 – 25 1998, **2**, 909-914.

20.2 Other Publications.

20.2.1 Refereed Journal Publications.

Belov, V.E., Gorskii, S.M., Zinoviev, A.Y. and Khilko, A.I. (1994b) "Acoustic monitoring of plane-stratified media with elastic cylindrical inclusions", Acoust. Phys., **40**, p 298.

Belov, V.E., Gorskii, S.M., Zinoviev, A.Y. and Khil'ko, A.I. (1994c) "Application of the method of integral equations to diffraction of acoustic waves at elastic bodies in a layer of liquid", Radiotekhnika i Elektronika, **40** (4) 548-560, (in Russian).

Donskoi, D.M., Zinoviev, A.Y., Chichagov, P.K. (1990), "Experimental study of the influence of gas cavity on the radiation of sound from a piston", Acoust. Phys., **36** (5), 480-481.

20.2.2 Conference Proceedings.

Belov, V.E., Gorskii, S.M., Zinoviev, A.Y. and Khilko A.I. (1994d), "Diffraction of the acoustical fields by the elastic bodies in oceanic waveguides: solution by the combine integral method", Proceedings of the 2nd European conference on underwater acoustics, Copenhagen, Denmark. 4-8 July, 1994.